

THESIS

3

(1996)

MICHIGAN STATE UNIVERSITY LIBRARIES



3 1293 01402 7761

This is to certify that the

dissertation entitled

POST-DEPOSITIONAL PROCESSING OF DIAMOND FILM
USING ELECTRON CYCLOTRON RESONANCE PLASMAS

presented by

Rabindra Nath Chakraborty

has been accepted towards fulfillment
of the requirements for

Ph.D. degree in Electrical Engineering

D. K. Reinhard

Major professor

Date June 8, 1996

**LIBRARY
Michigan State
University**

**PLACE IN RETURN BOX to remove this checkout from your record.
TO AVOID FINES return on or before date due.**

DATE DUE	DATE DUE	DATE DUE
9 1 2004	_____	_____
1 2 2 2 0 0	_____	_____
NOV 15 2003 3 1 1 7 0 3	_____	_____
OCT 0 1 2004	_____	_____
JUL 2 5 2005 0 9 2 2 0 9	_____	_____
_____	_____	_____
_____	_____	_____

MSU is An Affirmative Action/Equal Opportunity Institution

c:\nlrc\datedue.pm3-p.1

POST-DEPOSITIONAL PROCESSING OF DIAMOND FILM USING
ELECTRON CYCLOTRON RESONANCE PLASMAS

By

Rabindra Nath Chakraborty

A DISSERTATION

Submitted to
Michigan State University
in partial fulfillment of the requirements
for the degree of

DOCTOR OF PHILOSOPHY

Department of Electrical Engineering
1995

ABSTRACT

POST-DEPOSITIONAL ETCHING OF DIAMOND FILM USING ELECTRON CYCLOTRON RESONANCE PLASMAS

By

Rabindra Nath Chakraborty

Both dc arc jet and microwave CVD grown diamond samples were successfully etched using ECR plasmas generated from a microwave plasma disk reactor. The etch rate obtained from argon-oxygen-SF₆ ECR plasmas was an order of magnitude higher than the rate achieved from the conventional mechanical means. This research work is the first report on etching 100 mm diameter, 1.5 mm thick diamond disks. For uniform etching of 100 mm diameter diamond wafers, an etch rate above 8 μm/hr was achieved and up to 250 μm was removed from these wafers. Etch rate as high as 12 μm/hr were obtained on smaller samples. Response surface methodology was used to achieve this high diamond etch rate. Statistical analysis showed that oxygen and rf bias have the strongest positive influences on etch rate while SF₆ has a negative effect. Experiments also demonstrated that etching of diamond in an oxygen rich plasma environment is reactive ion assisted and an approximate theoretical calculation of the etch rate for reactive ion etching of diamond closely agreed with the experimentally obtained value. The etch rate was found to increase steadily with microwave input power and downstream distance. The variation of pressure

showed a maximum rate around 4 mtorr. Diamond etched in absence of SF₆ produced a black film on the etched surface which acted as a passivation layer. The etch rate was found to decrease as the black layer became denser. Hence etching of diamond at a steady high rate required the plasma to contain a minimum amount of SF₆.

100 mm diameter, ~1.5 mm thick, CVD grown polycrystalline diamond films were etched with as low as 5% non-uniformity over the surface. The non-uniformity of diamond etching was observed to decrease when etching was performed under different modal patterns. This observation was theoretically investigated to learn about the role of ambipolar diffusion in determining the spatial variation of etch rate for different resonant modes at downstream distance. The simulation results supported the hypothesis of mixing modes to obtain higher uniformity of etching.

A part of our research was aimed at planarizing rough diamond surfaces by first coating a sacrificial layer on diamond and then etching both diamond and the layer at the same rate. This method, referred to as the etch back method, was employed to planarize both dc arc-jet deposited and microwave CVD grown diamond samples. Different spin-on-sacrificial layers such as photoresist, titanium silicate emulsion in photoresist, and SOG were used for coating the rough diamond surfaces. Experiments conducted on fine grain, microwave grown diamond films with argon-oxygen-SF₆ plasmas and SOG sacrificial layers showed initial success of achieving planarization although the etch back technique did not succeed as well for coarse grain dc arc-jet deposited samples.

Patterning of the diamond film using SOG as the masking material was also briefly investigated on a diamond coated integrated circuit. An argon, oxygen, SF₆ plasma was successfully used to remove the diamond layer from the desired locations.

Copyright by
Rabindra Nath Chakraborty
1995

*However it is - good or bad,
It is for you, my Mom and Dad !*

Acknowledgments

First of all, I would like to thank my academic adviser, Professor D. K. Reinhard for his excellent research guidance, patient understanding of my academic needs and continuous support for over last three years. I have enjoyed every moment working with him and this experience will remain an asset for me all through my life. Besides academics, his goodness, dedication, honesty and equal respect for everyone have deeply moved me. I would like to thank Professor J. Asmussen and Dr. T. Grotjohn for their advises in my research. Also I was greatly benefited from their remarkable teaching of plasma related courses. I am thankful to Dr. M. Aslam and Professor B. Golding for their valuable comments on my research. Thanks are extended to Dr. P. Goldman, previously at Norton Diamond Film for his extensive co-operation in sending and documenting diamond samples. I am also thankful to Mr. B. Cline and Mr. K. Gray of Norton Diamond Film for supplying diamond samples and showing interests in transferring this diamond etching technology to industry as a supplement or replacement for the existing methods of diamond finishing. I sincerely acknowledge the help of my friends, Saeid Khatami for imaging SEMs, Brian Wright for repairing the plasma reactor, Nidhan Choudhuri for consulting statistics, and Anjan Ray for sharing his expertise in combustion. In addition, I want to thank Kuntal Thakurta, Krishnendu Majumdar, Goutam Das, G. Srikant and Murali Sreenivasan for

their silent wishes and precious friendship that gave me strength at the time of my distress. I want to express my gratitude to my father who sent me to America for studying. I want to share my satisfaction of completing this research with my brother Chiranjit Chakraborty, and my lovely little sister Kaberi Sen who always remained eager for this moment. Finally, I want to remember my first teacher, my mother who inspired me to join the doctoral program and encouraged me always to continue my journey to the pursuit of knowledge. To me, this success is her achievement.

Funding for this research was provided in part by State of Michigan Research Excellence fund and ARPA through Norton Diamond Film, a division of Saint Gobain/Norton Industrial Ceramics Corporation. The microwave plasma disk reactor used for this research is manufactured by Wavemat Inc. This reactor is integrated into a system manufactured by PlasmaQuest Inc.

Table of Contents

List of Tablesxi
List of Figures	xii
Chapter I. Introduction	1
1.1 Motivation of Etching Diamond with Plasmas	1
1.2 Research Objective	2
1.3 Outline of Dissertation	3
Chapter II. Background	4
2.1 Diamond	4
2.2 Different Methods for Diamond Finishing	8
2.2.1 Mechanical Abrasion	8
2.2.2 Laser Ablation	9
2.2.3 Etching via Chemical Reactions with Metals	10
2.2.4 Oxidation of Diamond in Molecular Oxygen	12
2.2.5 Etching with Ion Beams and Non ECR Plasmas	13
2.2.6 Etching of Diamond using ECR Plasmas	18
2.2 General Discussion of Microwave Electron Cyclotron Resonance Plasma	20
Chapter III. Introduction to Instruments & Experimental Set-up	28
3.1 Description of the Microwave ECR system	28
3.1.1 PlasmaQuest ECR Etching Machine	28
3.1.2 Operation of PlasmaQuest ECR Etching Machine	33
3.2 Description of Other Related Instruments	35

Chapter IV. Theory of Etch Processes	44
4.1 Different Types of Etching	45
4.1.1 Sputtering	45
4.1.2 Chemical Etching	46
4.1.3 Ion-assisted Etching	48
4.1.4 Ion-Enhanced Inhibitor Etching.	49
4.2 Plasma and Surface Interaction	50
4.2.1 Generation of Species	51
4.2.2 Diffusion of Species	53
4.2.3 Adsorption and Desorption.	56
4.3 Elementary Reaction Kinetics	59
4.4 Surface Kinetics of Ion-assisted Carbon Etching	62
Chapter V. Etching Experiments and Results	71
5.1. Variable Identification	71
5.2. General Discussion on Experimental Design	75
5.3 Process of Optimizing the Diamond Etch Rate	80
5.4 Effect of Variables on Etch Rate	93
5.4.1 Effect of RF Bias and RF Power on Etch Rate.	94
5.4.2 Effect of Microwave Power on Etch Rate.	104
5.4.3 Effect of Processing Pressure on Etch Rate	108
5.4.4. Effect of Oxygen, Sulfur Hexafluoride Ratio on Etch Rate	109
5.4.5 Effect of Argon, Oxygen Ratio on Etch Rate	115
5.4.6 Effect of Downstream Distance Etch Rate	120
5.4.7 Effect of Resonant Modes on Etch Rate	122
5.5 Black Film	123
5.6 Calculation of Approximate Diamond Etch Rate in Oxygen ECR Plasmas	131
Chapter VI. Uniformity of Etching and Control of Etch Profile.	135
6.1 Derivation of the Modal Patterns	136
6.2 Ambipolar Diffusion	145
6.3 Formulation of the Numerical Problem	149
6.4 Discussion of the Numerical Solution.	153

Chapter VII. Planarization and Masking of Diamond Films	158
7.1 Planarization	158
7.1.1 Planarization with Photoresist on Thick Film Samples	161
7.1.2 Planarization with Spin-On-Glass on Thick Film Samples	162
7.1.3 Planarization with Titanium-Silicate on Thick Film Samples	163
7.1.4 Planarization with SOG on Thin Film Diamonds	167
7.2 Masking	172
Chapter VIII. Summary and Future Research	175
8.1 Summary of Research	175
8.2 Future Work	177
8.3 Conclusions.	179
List of Appendices	181
Appedix A	181
Appedix B	183
Appedix C	184
List of References	191

List of Tables

Table 5.1 Ranges of the variables for the initial design	81
Table 5.2: The first design of experiments	82
Table 5.3: Effect of variables on etch rate	83
Table 5.4: The choice of gas flow rates	85
Table 5.5: Exploring the gas effects on the etch rate.	85
Table 5.6: Investigating the pressure effects	86
Table 5.7: Investigating the combined effect of power and argon	89
Table 5.8: Experimental design for understanding the effect of argon	89
Table 5.9: Variation of the operating mode and the power	91
Table 5.10: Uniformity analysis.	92
Table 5.11: Etch rate vs. rf bias: investigating the nature of dependence.	95
Table 5.12: The Effect of microwave power on etch rate	105
Table 5.13: Effect on SF ₆ to oxygen flow ratio on etch rate.	111
Table 5.14: Effect on argon to oxygen flow ratio on etch rate	116
Table 5.15: Effect of resonant mode on etch rate	123
Table 7.1: Dektak result of photoresist experiments	162
Table 7.2: Dektak result of SOG experiments	163
Table 7.3: Long range vs. short range dektak results	165
Table 7.4: Dektak result of titanium silicate experiments.	166

List of Figures

Figure 2.1: ECR effect	26
Figure 3.1: A 25 cm diameter ECR system - MPDR 325i	29
Figure 4.1: Sputtering	46
Figure 4.2: Pure chemical etching	47
Figure 4.3: Ion-assisted etching	48
Figure 4.4: Ion-enhanced inhibitor etching	49
Figure 4.5: Trench etching	50
Figure 4.6: Details of RIE processes	63
Figure 4.7: Reactive ion etching of diamond	65
Figure 4.8: Vertical and horizontal etching.	70
Figure 5.1: One at-a time experimental approach.	77
Figure 5.2: Results of regression analysis	84
Figure 5.3: The direction of steepest ascent.	87
Figure 5.4: Role of microwave power in rf induced dc bias	100
Figure 5.5: Etch rate vs. rf induced dc bias	101
Figure 5.6: Etch rate vs. rf power	102
Figure 5.7: Normalized etch rate vs. rf induced dc bias	103
Figure 5.8: Etch rate vs. microwave power at low power level	106
Figure 5.9: Etch rate vs. microwave power at high power level	107
Figure 5.10: Etch rate vs. process pressure	110
Figure 5.11: Etch rate vs. SF ₆ to oxygen flow rate ratio	112
Figure 5.12: Etch rate of diamond with and without black film	114
Figure 5.13: Etch rate vs. oxygen to argon ratio.	117
Figure 5.14: Sputter etch rate vs. rf power.	119
Figure 5.15: Subsequent etching of diamond in oxygen plasma	125
Figure 5.16: Etching of black film with Ar, O ₂ and SF ₆ plasma.	126
Figure 5.17: Raman spectrum	127
Figure 5.18: Globules on O ₂ etched sample.	128

Figure 5.19: Magnified structures of globules	129
Figure 5.20: Pre-etched sample surface	129
Figure 5.21: Conical structures on O ₂ etched sample.	130
Figure 6.1: Cylindrical cavity of length c and radius a	137
Figure 6.2: Figure 6.2: Modal patterns for TE and TM modes	146
Figure 6.3: The cross-section of plasma discharge.	150
Figure 6.4: The numerical grid	151
Figure 6.5: Region of solution and boundary conditions	152
Figure 6.6: Normalized downstream species density variation for mode 1	154
Figure 6.7: Normalized downstream species density variation for mode 2	155
Figure 6.8: Etching uniformity comparison for mode 1, mode 2 and mixed modes . . .	156
Figure 7.1: Method of polishing diamond	159
Figure 7.2: Short and long range surface fluctuations	166
Figure 7.3: Uncoated sample surface	169
Figure 7.4: Planarized surface after processing with low O ₂ containing plasmas. . . .	170
Figure 7.5: Planarized surface after processing with high O ₂ containing plasmas . . .	170
Figure 7.6: SOG coated diamond sample	171
Figure 7.7: Selectively etched diamond coated IC shows aluminum pad	174

Chapter I. Introduction

1.1 Motivation of Etching Diamond using Plasmas

With the advancement of chemical vapor deposition (CVD) methods, polycrystalline diamond can now be grown over relatively large substrate areas at a reasonably high rate[1.1]. But due to thickness and surface irregularities, as-grown diamond samples often need to be processed before they become useful for a given application. Etching diamond mechanically or chemically is a very difficult task since pure diamond is an extremely hard and inert material.

On a different context, recently developed low pressure, low temperature, plasma discharges, produced from electron cyclotron resonance (ECR) plasma reactors with microwave excitation, have demonstrated excellent promise in semiconductor processing [1.2]. For conventional semiconductor materials, these high density discharges are capable of achieving high etch rate uniformly over a large diameter substrate with negligible surface damage [1.3, 1.4]. Also high anisotropy and high etch selectivity are additional merits of these discharges. Because of the excellent performance exhibited by the ECR plasmas, our research was motivated to etch diamond with ECR plasmas and study its etch performances as the plasma characteristics are changed.

Most of our research was conducted as part of an intense research program called “Materials processing and manufacturing technologies for diamond substrate multi-chip modules and reactor selection and diamond MCM process development - phase I and II”, which was sponsored by the Advanced Research Project Agency (ARPA) and subcontracted to us by Norton Diamond Film. Some part of the research was also funded by Michigan Research Excellence Fund.

1.2. Research Objective

The focus of diamond etching research can be broadly divided into the following three areas:

- *Removal of Diamond and Thickness Reduction*

The first part of this research was concerned with the development of a precise and uniform plasma etching technique for 100 mm diameter diamond samples at an useful rate. To do so, it was essential to study the effect of various plasma parameters on etch rate. This was carried out by performing statistically designed experiments and the knowledge of these effects was then utilized to methodically optimize the etch rate with ECR plasmas.

- *Uniformity of Etching and its Analysis*

The second part of our research was intended to study the uniformity of etching 100 mm diameter polycrystalline diamond films with ECR plasmas. The goal was to study and find methods to control the etch profiles in order to obtain a desired final variation of wafer thickness.

- *Reduction of Surface Roughness & Masking of Diamond*

Surface roughness of as-deposited polycrystalline diamond films often poses problems for various applications, hence different methods are being employed to planarize the

rough surface. As a part of our research, ECR plasmas were investigated for reducing the surface roughness of the diamond films.

In addition, to utilize the high heat spreading capability of diamond, the possibility of applying ECR plasmas to selectively etch the diamond layer grown on an integrated circuit wafer was briefly studied in this research.

1.3 Outline of Dissertation

Following the brief introduction of the technology used for growing the samples we processed, various diamond etching methods as found in literature will be discussed in detail in chapter 2. At the end of this chapter, the principle of ECR plasma generation and its characteristics will be briefly reviewed. The description and operation of the specific ECR plasma reactor used in this research will be given in chapter 3. Various other instruments used for this research will also be introduced in this chapter.

Chapter 4 will discuss different plasma etching methods, surface reaction kinetics and the phenomenon of etching carbon surfaces in oxygen plasmas. In chapter 5, the statistical design of experiments and the optimization procedure of the diamond etch rate with ECR plasmas will be described in detail. The effect of the investigated parameters on etch rate and other important experimental observations will also be presented in this chapter with graphs and tables. In chapter 6, the technique for improvement of etching uniformity will be described along with the computer simulation results. Chapter 7 will discuss and document the research conducted on the planarization and masking of diamond. Finally chapter 8 will conclude this thesis with a discussion of the direction of future research.

Chapter II. Background

2.1 Diamond

Although artificial diamonds have to go a long way before they even begin to approach being economically viable as acceptable gem grade single crystal diamond, synthetic polycrystalline diamond is increasingly finding interest in industrial applications because of its attractive physical, chemical and optical properties. The extreme hardness of diamond and its chemical inertness in pure form, make it a useful material for coating mechanical tools that are exposed to abrasive and corrosive environments. Chemical vapor deposition (CVD) diamond coated products such as cutting tools, drills etc. are found to have much higher longevity than the uncoated ones. They also have a longer lifetime than tools coated with brazed or sintered diamond powder. Diamond is also being investigated for possible applications in electronic industries because of its interesting electrical properties. The large bandgap, low dielectric constant, and high hole and electron mobility at large electric fields are a few to name. Due to an incomparable heat dissipation capability at room temperature, diamond appears to have a promising market in making multi-chip modules for ICs with very high packaging density. Diamond also has some excellent optical properties including an absorption edge in the ultra-violet and a very high transparency over the entire visible and most of the infrared spectrum.

The combination of all these properties and the potential of diamond to be used in mechanical, optical and electronic industries are driving the fundamental research towards developing more inexpensive, fast, repetitive and convenient methods for growing and processing diamond.

Naturally occurring diamonds are believed to be the result of carbonaceous materials

having been subjected to tremendous pressure and heat deep within the earth. Synthetic, or man-made diamonds became possible in 1955 when laboratory equipment was used to subject graphite to great pressure and heat. The theoretical basis of the modern high pressure diamond synthesis rests on the calculations of the graphite-diamond equilibrium line in a pressure-temperature phase diagram and the first practical achievement of diamond formation was based on the pioneering work of P.W. Bridgman and the engineering teams in General Electric, ASEA and De Beers[2.1].

Today, diamonds are also grown under metastable conditions at low pressures using chemical vapor deposition (CVD). In most cases, CVD methods use a mixture of hydrogen and a gaseous carbon compound such as methane which is activated and contacted with the substrate to produce a diamond film on the substrate [2.2]. The hydrogen gas is dissociated into atomic hydrogen and then reacted with the carbon compound to form condensable carbon containing radicals such as CH_3 . The atomic hydrogen also reacts with surface-bonded hydrogen, abstracting it and creating active surface sites. The carbon containing radicals are then adsorbed onto these available surface sites. The carbon is subsequently incorporated into the diamond lattice, with abstraction of adsorbate hydrogen, again by atomic hydrogen. Although the exact chemistry for diamond formation in the metastable state is complicated and still under investigation, the dissociation of the hydrogen molecule to atomic hydrogen is generally the key step to initiate the diamond growth. Conceptually a principal function of a diamond growing reactor is to provide a means to dissociate the hydrogen molecules. Hence any reactor that is capable in putting in the necessary energy to produce enough atomic hydrogen should potentially be successful in growing diamond [2.3].

Hot filament reactors, acetylene flames, dc arc jets, dc plasma discharges, radio frequency (rf) discharges and microwave discharges are some of the frequently used diamond growing reactors. Out of these different techniques, the dc arc jet deposition method is further elaborated on here since most of the samples processed for our research are produced using this technique.

The deposition by conventional dc arc jet processes is usually confined to small areas and is difficult to control in terms of quality, thickness and reproducibility. An improved method of the dc arc jet, called magnetically mixed and spread arc (MMSARC) is in use for producing large area, thick diamond wafers at high growth rates [2.4, 2.5]. In 1991, Norton Diamond Film first reported production of disks up to 6 inches in diameter and 1 mm thickness [1.1] using this technique. The MMSARC deposition technique utilizes a controlled interaction of a solenoid magnetic field and the intense electrical discharge to alter the arc properties providing a means of controlling the electron and ion characteristics. As a result of the applied magnetic field, better mixing of the hot plasma with the cooler surrounding gas is achieved which in turn improves the homogeneity of the plasma jet and results in more uniform deposition of diamond on a large area.

However, no deposition process using any of the reactors mentioned before, can grow polycrystalline diamond to an exact thickness avoiding all undesired surface irregularities. Rather, as-deposited diamond samples contain a lot of unwanted features such as surface roughness, inappropriate thickness, pits, bowing etc. To correct these shortcomings of the deposited diamond, wafers are often grown to more than the required thickness to keep allowances for post-depositional processing work. Obtaining the right thickness and the desired surface specification from the as-grown wafer condition is not an easy task and is

often referred to as diamond finishing in this report.

Ever since the hardest material became a fascinating gem stone, the art and technology of cutting and polishing natural diamond has been evolving. Research on CVD polycrystalline diamond finishing is relatively new and was started a little over a decade ago.

With the advent of better diamond growth technology for depositing thick films, reduction of thickness of a given diamond wafer to a specified dimension at a faster rate with reasonable uniformity, has become a new requirement in diamond finishing work. Finding a fast, uniform, repetitive and easy-to-use etching method for diamond with large surface area is one of the important objectives of our research.

The large area diamond samples that we processed for this research work, are about 100 mm in diameter, 81 cm² in area, 1.4 mm in thickness and approximately 32 g in weight. Evidence of etching 100 mm diameter free-standing diamond disks prior to this work is not found in literature. This is likely due to the fact that only recently CVD diamond growth technology has progressed enough to deposit diamond on large area substrates at relatively high rate. Therefore the etching experiments have now become affordable. In addition to the 100 mm diameter free-standing diamond wafers, a few smaller diamond disks with 50 mm diameter and 17.8 mm diameter were also processed. Additional etching experiments were performed on some non-circular samples including square shaped samples of dimensions 10 mm X 10 mm and 20 mm X 20 mm. Most of these films are optically semi-transparent in nature and have a milky or blackish surface appearance depending upon the purity of the diamond. These samples were provided to us by the Norton Diamond Film.

2.2 Different Methods for Diamond Finishing

2.2.1 Mechanical Abrasion

The normal procedure in mechanical grinding is to use grit powder of a harder material than the workpiece but there is nothing harder than diamond so diamond is lapped with diamond. The traditional method of abrading diamond is by grinding on a flat wheel or scaife typically about 300 mm in diameter and made from cast-iron of carefully selected porosity. This scaife is charged with diamond powder ranging in sizes from less than 1 micrometer to about 40 micrometer, the larger sizes giving a faster removal rates but a rougher finish. Therefore it is common practice to begin polishing with coarse powder and finish off with say 0.1 micrometer powder to give a relatively smoother surface. The diamond powder is mixed with olive oil or some other base to form a slurry or suspension which is rubbed over the metal scaife and then left for some time for the suspension to be absorbed by the pores. The diamond to be polished is usually mounted in a metal holder known as a dop where it is held in place by two or more metal claws, or sometimes by a low melting point metal. The surface to be finished is placed against the scaife rotating at around 2500 rpm under a load of order 1 kg. The success in removal or polishing of diamond depends quite critically on several things, especially the orientation of the diamond, regular recharging of the diamond slurry, the vibration free running of the scaife, and rigid holding of the diamond piece [2.6, 2.7]. Diamond removal becomes very difficult if presented to the scaife in certain orientations, for example, abrasion of diamond along $\langle 100 \rangle$ is much easier than along $\langle 110 \rangle$. The removal rates along a hard direction depend more critically on the recharging of diamond paste.

Today the cast iron scaife is often replaced by a wheel of similar geometry in which

diamond powder is bonded in a metal alloy, or sometimes organic resin, on the surface of the wheel. A diamond bonded scaife costs much more than a cast iron scaife and it can be easily damaged but its use avoids the interruption and the labor involved in keeping the cast iron wheel fully charged with powder. It is necessary to avoid overheating the diamond piece by applying too much a load, as it is quite possible for a diamond to become red hot under poor conditions. In this case, an outer layer of the diamond will be burnt and damaged [2.8]. The chief draw-back of the mechanical etching methods is that they tend to be costly and time consuming, often entailing an ablating rate of about 0.1 micrometer/hr and requiring up to several weeks to finish a four inch diamond wafer. Obtaining a uniformity of etching over a large area is quite difficult and at times, prominent polish lines and sub-surface damages appear due to mechanical etching. Also an optical grade finishing of diamond surfaces virtually seems impossible to achieve through the mechanical polishing means. For all these combined reasons, alternatives to mechanical etching method are being investigated.

2.2.2 Laser Ablation

Lasers are normally used for drilling and cutting a wide variety of materials. A laser beam can concentrate a pulse of energy on a very small area on a specimen in a very short period of time [2.8]. Hence before the heat generated has the time to spread to the rest of the work-piece the material under the beam receives sufficient energy to vaporize. Lasers are commonly used to drill polycrystalline diamond because it can pierce diamond without causing much damage to the sample, but their ability to cause ablation and to convert diamond to graphite can be used to etch, polish and pattern diamond as well.

Since graphite is much easier to remove compared to diamond, laser assisted etching of diamond also finds application in micropatterning the nucleation sites and selective growth of diamond film [2.9, 2.10, 2.11]. Multi-pulse radiation from a laser, e.g, XeCl laser [2.12], has been used for roughness reduction of the as grown diamond surfaces. Usually the surface roughness is characterized in terms of R_a and its definition is given later in chapter 7. However, to improve the polishing efficiency for a very rough diamond film ($R_a = 250 \mu\text{m}$), a combined method of laser induced polishing and plasma etching was developed in which the largest defects are removed by irradiation with a powerful YAG laser [2.13].

Although lasers can be used for cutting, drilling, smoothing or even micro-patterning diamond as mentioned above, they would not appear very useful for bulk removal of material from a large area diamond sample. This is mainly because of the fact that the laser focuses on a very small area of the surface and ablates and graphitizes only that part of the specimen on which it is incident.

2.2.3 Etching via Chemical Reactions with Metals

Diamond is extremely inert chemically and not affected by acids except those which at high temperature act as oxidizers. However, there are some etching mechanisms. Diamond is reported to be etched by molten sodium nitrate at a temperature as low as 427°C [2.14]. It can also react with elemental metals which form carbides such as tungsten, tantalum, titanium and zirconium, and act as solvents for carbon. For example, it is well known that a diamond cutting tool suffers severe wear while cutting ferrous alloys which means that diamond can be etched using its solubility property in some molten metals, such as iron,

manganese, nickel, cobalt, chromium and platinum [2.15, 2.16] etc. In this case, the diffusion of carbon atoms into hot metals is the primary key for etching. The maximum stock removal of diamond on a 7 mm X 7 mm sample was found to be 7 micrometer / hr with an iron plate at 950 °C in vacuum [2.17]. About 55% of the area was reported to be polished in this method.

Both solid transition metals such as Fe, Mn and molten rare earth metals such as Ce are found to chemically etch diamond by means of carbon solubility and are used for thinning, polishing and patterning of diamond wafers. Free standing diamond films are sandwiched between two Mn or Fe sheets or powder aggregates and are heated in an inert atmosphere at about 900 °C. After the etching is complete, the wafer is cooled and the metallic material is removed [2.18, 2.19]. Etching of CVD diamond films by molten rare earth metals can be accomplished either by multiple layer stacking of rare earth metal sheets and diamond films and heating to above the melting of the metals or by dipping of the diamond films into a bath of molten rare earth metals [2.20, 2.21]. In May 1995, about 70 micrometers of diamond were reported to be etched with molten Ce at 920 °C in approximately 4 hours. However, the area of the sample and the uniformity of the etching were not mentioned. That report [2.22] also mentions a strong orientation dependent etching behavior of single crystal diamond. The etching rate dependence on crystal orientations with selenium at 920 °C is reported to be in the order (111) > (100) > (110) with a relative ratio of about 5:2:1. With molten rare earth metals, crystal grains are removed from both the growth and the nucleation side. This high difference in etch rate from one direction to the other can be used to advantage where the anisotropic etching is essential. However, for polycrystalline diamond films where grains may grow in all possible directions, this etching feature may

produce non-repetitive etch rate especially for different samples. The high sample to sample variation may pose difficulty in standardizing this processing technology.

2.2.4 Oxidation of Diamond in Molecular Oxygen

During heating, natural diamond is transformed into graphite at about 1800 °K in inert atmosphere or in vacuum. However, in the presence of oxygen, diamond starts to be oxidized at a temperature as low as 900 °K [2.23, 2.24]. From the fact that diamond loses weight in oxygen containing atmosphere at sufficiently high temperature, it is known that diamond can be removed by oxidation. Although the role of oxygen in etching diamond is not entirely understood, several attempts have been made to understand the oxidation behavior of polycrystalline diamond in molecular oxygen at elevated temperatures [2.25, 2.26]. A careful characterization of heating diamond at an elevated temperature reports [2.27] that compared to other forms of carbon, diamond exhibits a relatively oxidation resistant property. This results in a preferential removal of non-diamond content of the sample when heated. Hence it can be expected that the etching characteristics and finishing of diamond surface with oxygen will be dependent on the purity of the diamond sample. Another study [2.28] of polycrystalline diamond oxidation with air at 1073 K shows that the oxidation of synthetic diamond films started at lower temperature than that for natural diamond. The same study reports that the rates of oxidation of the polycrystalline diamond films synthesized by the hot filament and microwave plasma methods are found to be intermediate between the 111 and 100 planes of natural diamond crystal. The apparent activation energy for the oxidation of the synthetic diamond films are reported to agree with that for the oxidation of natural diamond at low oxygen pressure.

Further investigations [2.29] to understand the oxidation kinetics with the microwave plasma assisted diamond films, reveal that the oxidation rate of the microwave plasma deposited diamond films increase directly with sp^2 content of the film, meaning the graphite content of the film influence and help increase the etch rate of polycrystalline diamond. This observation certainly supports the oxidation resistant nature of pure diamond in contrast to other easy-to-oxidize forms of carbon, e.g, graphite.

Although diamond can be etched in molecular oxygen at high temperature, a more reactive oxidizing atmosphere is one with appreciable atomic oxygen. This is achieved in ion beams and plasma sources as described next.

2.2.5 Etching with Ion Beams and Non ECR Plasmas

Today chemically reactive plasma discharges are not only widely used for integrated circuit manufacturing but also provide a very vital technology for processing of materials in other industries as well. Plasmas, the collection of electrons, neutrals and ions in a quasi-neutral environment, are used for precise etching, patterning and other surface modifications. Plasmas can be generated in a laboratory in many different ways using different sources of input energy, e.g, dc, rf, microwave and laser, required to create the plasma species and maintain a steady state density of species by compensating the species lost in the process of bulk recombinations in the plasma, and the surface recombinations at the walls and on the work-piece. Such plasmas can contact a work-piece directly and be used as a source of ions in an ion source.

In most cases, it is found that reactive ions are primarily responsible for fast anisotropic etching, hence some sources are designed to extract ions from the bulk plasma using

high voltage grid which is then focused on a surface for processing. The Kaufman ion source is such an apparatus that produces a high energy ion beam and is widely used in surface treatment. An advantage of this low pressure, line of sight, beam technique is the flexibility of directional bombardment which is not available in other plasma processes.

Ion beam etching is normally classified in two categories. If the inert gas ion beam is used for an etching it is called ion milling. If the ion beam etching uses the ions of a gas that is chemically reactive with the work-piece, it is referred to as reactive ion beam etching (RIBE).

Reactive ion beam etching of diamond has been studied for more than a decade using ion extracting sources similar to the Kaufman ion source. Etching of diamond with oxygen ion beams was reported [2.30] in 1984. It was found that the sputter yield of oxygen ions varied with the incident angle of ions and increasing the energy of oxygen ions from 0.5 to 1.0 keV did not necessarily lead to an increase in sputter yield. Ion beam assisted etching of diamond using a 2KeV Xe^+ beam and a reactive gas of nitrogen dioxide in a Kaufman ion source has also been reported in the literature [2.31]. The etching rate was observed to vary from 3 micrometer/hr at 500 °K to 12 micrometer/hr at 0 °K. This inverse temperature dependence of etch rate is believed due to reduced adsorption of nitrogen dioxide on the diamond surface at higher temperature. It is also noted that in ion beam assisted etching, nitrogen dioxide is reported to produce an order of magnitude higher etch rate than oxygen. This is assumed to be due to the higher adsorption of nitrogen dioxide on the diamond surface compared to oxygen. However, usage of nitrogen dioxide poses an environmental hazard [2.32]. Hence the possibility of obtaining higher etch rate of diamond using gases that creates non-hazardous products continued.

The surface planarization work of CVD polycrystalline diamond with ion beam irradiation [2.33] shows that the etch rate and the reduction of surface roughness has a strong dependence on the angle of ion beam incidence. In the study by Hirata et. al., smooth surfaces of microwave plasma CVD diamond films were obtained when the incident angle was set up to 0° and 80° and the sample was heated to 400°C in an oxygen atmosphere. The surface roughness was reported to reduce from $3\ \mu\text{m } R_{\text{max}}$ to $0.5\ \mu\text{m } R_{\text{max}}$. Similar to R_a , R_{max} is a measure of surface roughness and will be described later in chapter 7.

A research group at the University of Arizona, Macleod et. al, reported their results on diamond planarization techniques using oxygen ion beams in a sequence of papers [2.32, 2.34, 2.35]. Their technique of using an overcoat on diamond surface and finding an appropriate condition of etch rate matching will be also discussed in detail in chapter 7.

Reactive ion etching (RIE), as opposed to RIBE, refers to plasma etching where reactive ions cross the plasma sheath and are incident on the substrate. RIE has also been applied to diamond etching. For example, a microwave but non Electron-Cyclotron-Resonance (ECR) plasma was successfully used to etch polycrystalline diamond film grown on silicon substrates [2.36]. Although that paper intended to study the nature of diamond film regrown on an etched diamond surface, an etch rate of 24 micrometer/hour was reported when the substrate is heated to 850°K by the input microwave power. Room air at an unknown flow rate was introduced for etching diamond at about 53 torr of processing pressure while about 650 watts of microwave power was put into the plasma reactor.

A study of RIE processing of diamond with oxygen and hydrogen was also carried out using a commercial RIE system [2.37]. Most of the etching in that report was performed with between 200-300 W rf power, a gas flow of 40-80 sccm, and a processing pressure of

65-80 mtorr. Polycrystalline diamond etched with 0.4 KeV oxygen ions at an oxygen flow of 80 sccm and at 65 mtorr processing pressure gave rise to an etch rate of 1.8 - 2.4 μ m/hr as opposed to 2.1 μ m/hr for natural II A type diamond. Use of hydrogen plasmas to etch diamond showed a relatively lower etch rate compared to oxygen discharges.

The same paper reports the use of oxygen and argon mixtures for RIE etching of polycrystalline diamond. It was found that adding a substantial amount of argon in the reaction chamber did not affect the etch rate. Also an increase of oxygen to argon ratio from 0 to 100% shows an initial increase in etch rate but a saturation behavior afterwards. This suggests that for a given process condition, the oxygen ions available at the surface of the substrate is not dependent on the number of oxygen atoms in a gas mixture as long as a minimum supply of the oxygen is maintained. Assuming the etch rate depends only on the number of oxygen ions, the paper explains that the number of reactive oxygen ions in dynamic equilibrium with the argon-oxygen mixture is presumably not a strong function of the partial pressure of oxygen in the gas mixture and this is the reason of the above observation.

Another experiment reported the use of an rf plasma to etch diamond, diamond-like-carbon and graphite simultaneously at about 50 mtorr, and about 100 °C. This paper suggests that the selectivity of oxidation between non-diamond and diamond forms of carbon is very high for oxygen plasmas, much higher than for molecular oxygen at a temperature greater than 600 °C. Also according to this report, plasma oxidation at low temperatures does not result in faceting of diamond, in contrast to high temperature oxidation in molecular oxygen or plasma oxidation at elevated temperature which resulted in faceting along (111) direction [2.38].

Subsequent study of RIE etching of diamond films with applied bias to the diamond substrate in an oxygen only plasma reported formation of columns on the diamond surface [2.39]. Change of rf bias to the substrate or the total processing pressure was found to have no influence on the formation of these columns. To understand the details of this phenomenon, etching experiments with oxygen only, oxygen - argon and oxygen - SF₆ plasmas were conducted in a parallel plate reactive ion etching plasma system. For all the experiments, 200 watts of rf power, 200 mtorr of oxygen pressure and a total of 40 sccm of gas flows were maintained. With oxygen-only plasma, small cones appeared after almost 1 hour of run which developed into columns after longer etching. Once the columns were formed, the area between the columns etched at a faster rate than the columns themselves. Therefore, the etch rate of the layer is determined by the etch rate of the columns. The orientation of the columns are found to have no connection with the growth direction of the film. With oxygen-argon plasma, the oxygen flow rate was fixed at 10 sccm and the argon flow rates were varied between 2.5 and 80 sccm keeping the rf power fixed at 200 watt and total pressure at 200 mtorr, but the columns appeared on etched surface in all cases.

However, the authors reported that diamond etched in pure SF₆ produced no columns and gave an etch rate of about 0.14 μ m/hr. Also, when SF₆ was added to oxygen with a minimum of about 1:3 ratio, the column formation was not observed. Under those conditions the etch rate was 0.94 μm/hr.

The composition of these columns formed after etching in oxygen only plasmas were investigated using X-ray photoelectron spectroscopy which determined that next to carbon and oxygen, aluminum and fluorine contributed in considerable amounts to the XPS signal. The aluminum on the sample surface is believed to originate from the aluminum

chamber. According to the paper, the shape of the C 1s peak suggests the existence of single carbon compound. Investigating the reason for column formation during RIE etching in an oxygen only or in oxygen - argon plasmas, the authors conclude that columns are formed due to an micro-masking effect caused by the deposition of hard-to-etch material from the chamber walls. They suggest that fluorine causes sufficient lateral etching to prevent cone formation.

2.2.6 Etching of Diamond using ECR Plasmas

Recently microwave plasma reactors are being widely used because of their electrodeless nature and their ability to create very high density excited and charged species over an attractive range of pressure variations. An important development in low pressure and low temperature microwave plasma processing is the electron cyclotron resonance discharge. The advantage of the ECR approach is that much lower ion energies can be used while retaining reasonable etch rate on any processing material. This way the processing damages are reduced significantly and the device performances are improved. Hence the ECR etching is finding increasing application in device fabrication [2.40].

The first paper on dry etching of diamond with ECR plasmas came from AT&T Bell labs [2.41] by Pearton et. al., in April 1992 and it reported the use of a Plasmatherm 720 ECR system which has an Asmussen-type multipolar resonant cavity (Wavemat MPDR 300) operating at 2.45 GHz. A systematic study of the dependence of etch rate on plasma parameters were performed. The variables, pressure, microwave power and dc bias were varied between the ranges of 1 and 30 mtorr, 200-700 watts, and -50 to -300 V respectively. The dc biases on the substrate are induced by the 13.56 MHz rf powering of the

cathode. Etching in oxygen-only plasma at 1 mtorr, with 400 watts of input microwave power showed a strong dependence of etch rate on rf bias. According to this paper, the etch rate rises rapidly for biases below about 100 V and shows a saturation behavior at higher bias region. This observed effect of improvement of etch rate with increase of bias in the low bias zone, is explained as the ion-enhanced desorption of the etch products which are expected to be CO and CO₂. At higher rf bias, with sufficient supply of energy at the surface, the removal of etch products no longer limits the mechanism, hence a saturation type behavior on etch is noticed. The rise of etch rate thereafter is because of the increase of direct physical sputtering of the diamond.

The variation of the etch rate with increasing power at a fixed bias of -80 V and a pressure of 1 mtorr, showed a continuous increase. This is the result of an increased density of oxygen ions incident on the sample surface.

The diamond etch rate variation with oxygen discharge pressure at a fixed bias of -80 V and microwave power of 400 watts was found to increase with increasing pressure. The increased supply of active oxygen species on the diamond surface at higher pressure is thought to be the reason for this. Also described in this paper is photolithographic patterning of the diamond film using both Hunt 5209E photoresist, and dc magnetron sputtered Ti-Pt-Au masks. The etching is reported to be highly anisotropic at 1 mtorr, -80V, and 400 watts of oxygen plasmas. Pearton et. al, reported an etch rate as high as 24 micrometer/hour. They also noted that an addition of SF₆ to the oxygen discharge increases the rate of diamond etching from what is obtained with oxygen only, however, no explanation for this observation is given in the paper.

Shortly after the above paper was published, another paper [2.42] in September 1992,

reported the dry etching of diamond using ECR plasmas for fabricating semiconductor devices on a plasma assisted CVD homoepitaxial diamond film. That paper described that since neither the thickness nor the doping concentration of that CVD films was ideally controlled, the adjustment of the active layer thickness was taken to be an alternative approach for fabricating recessed gate depletion MOSFETs. Because of the lesser probability of introducing surface damages, ECR plasmas were chosen for etching the active region of the field effect transistor with a recessed gate and also for creating the isolation zone. Creating the electrical isolation involved patterning a 0.1 micrometer thick sputter deposited silicon dioxide layer with photolithography to form an etch mask. The processing condition of 0.4 mtorr partial pressure of oxygen, 2.7 mtorr partial pressure of Argon, at a forward power of 1000 watts with no induced dc bias to the substrate yielded an etch rate of about 0.5 micrometer/hr.

Etching of CVD diamond grown on a Mo substrate in a dc discharge using 50% oxygen and 50% argon ECR plasma was reported from Russia [2.43]. According to the paper, the etching of diamond in pure oxygen plasmas makes it porous but the surface is somewhat polished in oxygen-argon plasmas. The average electron temperature and the ion energy distribution function of the plasmas were measured by a three-grid analyzer and a Langmuir probe respectively. It was believed that the energy distribution of the oxygen ions were influenced by the addition of argon into the plasma [2.44].

2.3 General Discussion of Microwave ECR Plasma

The technology for microwave generation of plasmas has been known since the invention of high power microwave sources during World War II, but it is more recent that these

sources have been repeatedly modified to improve material processing technology. Electron-cyclotron-resonance discharges are in most cases excited at a commercial microwave frequency of 2.45 GHz. These reactors differ from other microwave sources in their capability of coupling microwave power to the plasma at a very low pressure, usually in the neighborhood of 1 mtorr. ECR sources generate very dense but low ion energy plasma species which significantly reduce the possibility of introducing surface and sub-surface damages during processing. In addition to damage-free processing, ECR plasmas produce very high anisotropic etching at reasonably high rates and with an excellent uniformity. Because of the all these characteristics in combination, the ECR reactor is of interest today to meet the requirements of stricter processing standards, especially in IC fabrication technology. Also as noted earlier, ECR plasmas are of interest for diamond finishing.

Therefore, background information on the mechanism and basic principles for operation of ECR discharge is discussed here in the context of the particular ECR design used in this study, the multipolar plasma disk reactor (MPDR).

- *Functioning of an Electron-Cyclotron-Resonance Plasma Source*

Asmussen et.al., have described a multipolar ECR plasma source, also referred to as the microwave plasma disk reactor, which utilizes a tunable microwave cavity designed to create a cylindrical disk discharge that provides a large discharge cross sectional surface for plasma processing on a large diameter substrate [2.45]. A sliding short and the cylindrical cavity wall form the electromagnetic excitation zone within which the quartz discharge chamber confines the working gas to the discharge region. In electrodeless high-density low-energy plasma sources, the waves are generated near a plasma surface and

then propagate into the plasma where they are subsequently absorbed, leading to heating of plasma electrons and thereby exciting the discharge. For ECR discharges, the microwave energy is coupled to the natural frequency of the electron gas in the presence of a magnetic field where the natural resonance frequency of electrons is defined as:

$$\omega_{ce} = \frac{eB}{m_e} \quad (1)$$

In the above expression, e is the charge of the electron, B is the strength of the static magnetic field, and m_e is the mass of an individual electron. The resonance occurs when the electron cyclotron frequency equals to the excitation frequency ω . In an actual discharge this condition can be satisfied in a volume or surface within the discharge where the static magnetic field strength is appropriate for resonance, i.e. $\omega = \omega_{ce}$ and a component of electric field is perpendicular to the static magnetic field. This is called an ECR zone. The electrons are accelerated in this zone and in turn ionize and excite the neutral gas. The result is a plasma, the property of which can be varied with the discharge pressure, the gas inflow rate and the microwave input power [2.46].

The time and spatially varying microwave electric field which maintains the discharge can be mathematically expressed as $E(\vec{r})e^{j\omega t}$. This spatially varying electric field penetrates the discharge volume and influences the movement of the electron gas. An independent static but spatially varying magnetic field is also impressed on this discharge volume.

Under steady state conditions of the microwave discharge, the total electromagnetic power absorbed by the whole plasma volume P_a has to equal the total power lost by the plasma volume P_{loss} . The input power has a non-uniform distribution over the discharge

volume and thus the power absorbed by an arbitrary differential volume becomes a function of position. If the absorbed power density at position \vec{r} is expressed as $\langle P \rangle_{abs}(\vec{r})$, then it can be related to the discharge complex tensor conductivity $\sigma(\vec{r})$ and electric field $E(\vec{r})$ as:

$$\langle P \rangle_{abs}(\vec{r}) = \frac{1}{2} Re[E(\vec{r}) \bullet \sigma(\vec{r}) E(\vec{r})] \quad (2)$$

where both the complex plasma conductivity and the electric field are the functions of position in co-ordinate space.

For any differential plasma volume, this absorbed power $\langle P \rangle_{abs}(\vec{r})$ must be lost to maintain a steady state. Hence the power balance equation at any arbitrary position is written as:

$$\langle P \rangle_{abs}(\vec{r}) = \langle P \rangle_{loss}(\vec{r}) \quad (3)$$

where the power lost by the differential volume is expressed as $\langle P \rangle_{loss}(\vec{r})$ at a position \vec{r} . If the power absorbed per unit differential volume $\langle P \rangle_{abs}(\vec{r})$ is integrated over the whole discharge volume, we get the total microwave power absorbed by the plasma P_a .

$$P_a = \int_{vol} \langle P \rangle_{abs}(r) dV = \int_{vol} \langle P \rangle_{loss}(r) dV = P_{loss} \quad (4)$$

The absorption and the loss mechanisms in a discharge are quite complicated. The microwave electrical energy is absorbed by the charged particles e.g, electron and the ion gas. However, the work done on a charged particle by an electric field varies inversely as the particle mass, hence the energy imparted to the electron gas is much greater than the energy to the ion gas. Thus the direct energy transfer from the input source through the

electric field to the ions is usually neglected. It is important to note here that the electrons gain energy only between the collisions and they lose energy to other particles during the elastic and inelastic collisions. Because of electron-ion and electron-neutral elastic or inelastic collisions, the energy of the electron gas is shared by ion gas and neutral gas. This is the basic mechanism that heats up the ions and the neutrals. The power absorbed term in equation (4) mainly refers to the energy gain by the electron gas and the power lost term mainly refers to the energy interchange processes that reduce the electron energy.

In a non-ECR reactor, the time-averaged microwave power density absorbed by the electron is given by [2.47]:

$$\langle P \rangle_{abs}(\vec{r}) = \frac{n(\vec{r})e^2|E(\vec{r})|^2}{2m_e\nu_e} \left[\frac{\nu_e^2}{\nu_e^2 + \omega^2} \right] \quad (5)$$

where $n(\vec{r})$ is the steady state electron density, $|E(\vec{r})|$ is the magnitude of applied electric field, ω is the operating frequency, m_e is the electron mass and ν_e is the effective collisional frequency. At very low pressure the mean free path of the electron-neutral and electron-ion becomes very long and the number of probabilistic collisions between electron with neutrals or ions drastically reduces, which means $\nu_e \ll \omega$. Applying this condition, we can approximate equation (5) to the following form:

$$\langle P \rangle_{abs}(\vec{r}) = \frac{n(\vec{r})e^2|E(\vec{r})|^2}{2m_e\nu_e} \left[\frac{\nu_e^2}{\omega^2} \right] \quad (6)$$

It is clear from equation (6) that at very low pressure where the effective collisional frequency is much lower than the operating frequency, $\frac{\nu_e}{\omega} \ll 1$, the power absorbed in a

given differential volume $\langle P \rangle_{abs}(\vec{r})$ falls off rapidly and sustaining the discharge becomes extremely difficult. Microwave ECR reactors overcome this difficulty of low pressure processing. At very low pressures such as 1 mtorr, the coupling of microwave energy to the electrons is achieved by exploiting an externally impressed static magnetic field. The following discussion briefly shows the phenomenon of electron resonance and its effect on the power coupling expression. The details for the ECR theory may be obtained from [2.48].

The presence of the static but spatially varying magnetic field influences the electron ballistics inside a discharge and the power absorbed term of the expression (5) modifies.

$$\langle P \rangle_{abs}(\vec{r}) = \frac{n(\vec{r})e^2|E(\vec{r})|^2}{2m_e v_e} \left[\frac{v_e^2}{2} \left\{ \frac{1}{v_e^2 + (\omega - \omega_{ce})^2} + \frac{1}{v_e^2 + (\omega + \omega_{ce})^2} \right\} \right] \quad (7)$$

The above equation shows the introduction of ω_{ce} in the modified power absorbed expression. ω_{ce} is the natural resonance frequency for the electrons and was defined before in equation (1). At the resonance frequency, $\omega_{ce} = \omega$, trivial mathematical manipulation of equation (7) shows that a very high power absorption will occur because of the presence of the pole at that frequency. Physically, at the electron cyclotron frequency, the component of the electron velocity that is perpendicular to both static magnetic field and electric field, experiences a force, resulting into an outward spiraling motion with increasing radius. The electron gains energy proportional to the square of time it spends inside the ECR zones. Typically in a discharge the electron orbit radius remains limited either by the elastic or non-elastic collisions with other particles, or moving out of the ECR zone. Sometimes the charges are lost on the walls as well. The electron motion during ECR coupling is shown

in the Figure 2.1. The ECR effect is largely lost at sufficient high pressures, where the time between the collisions is small compared to an ECR cycle.

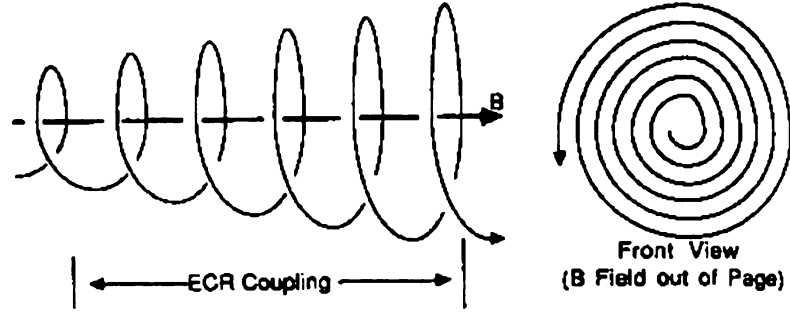


Figure 2.1: ECR effect [2.48]

Through the ECR coupling mechanism, the input microwave energy is thus transferred to the electron gas which then transfers energy with the elastic and inelastic collisions to neutrals and ions. Some of the energy is dissipated through conduction, radiation and convection losses. The complete expression for the power loss term for a given differential volume is given as [2.48]:

$$\langle P \rangle_{loss} = \left[\left(\frac{5k_B T_e}{2} \right) \frac{D_a}{\Lambda^2} + \nu_{men} \left[\frac{2m_e}{M_n} \right] \frac{3k_B}{2} (T_e - T_n) + eV_i \nu_i + \sum_j eV_{exj} \nu_{exj} \right] n(\vec{r}) \quad (8)$$

In the above equation D_a is the ambipolar diffusion coefficient, T_e is the electron temperature, T_n is the neutral gas temperature, k_B is the Boltzmann's constant, Λ is the discharge diffusion length, ν_i is the ionization frequency, ν_{exj} is the j^{th} excitation frequency and V_{exj} is the excitation potential.

At very low pressure both the conduction and convection losses are negligible since the number of carrier particles are very few at high vacuum. In most cases, the radiation

loss is also neglected.

Once the plasma species are created inside the discharge, they diffuse in all directions. In a conventional ECR etching machine, usually the substrate is independently rf biased, inducing a negative dc voltage. Since the plasma is quasi-neutral in nature, only those positively charged species that diffuse and come close enough to the applied rf bias, experience an attracting force. A nearly collisionless plasma sheath is formed around the rf biased substrate and the ionized species gain energy when travelling through this sheath before striking the surface of the work-piece.

Energetic ion fluxes to the substrate surface are mainly responsible for enhancing reactive ion etching. Further details about the etching process on the work-piece are discussed later in chapter 5.

Chapter III. Introduction to Instruments & Experimental Set-up

Many instruments were used at different points to carry out the diamond etching research. An introduction to these instruments will briefly be presented in this chapter. The general theory of ECR plasmas was already presented in section 2.3. In this chapter, section 3.1 focuses more on the constructional and operational details of the particular etching machine that we used for diamond processing. Section 3.2 describes other related equipment that were often or occasionally used for our research.

3.1 Description of the Microwave ECR system

3.1.1 PlasmaQuest-Wavemat ECR Etching Machine

Our plasma etching machine uses a 30.5 cm internal diameter cylindrical ECR cavity applicator. This ECR cavity, also known as a Microwave Plasma Disk Reactor (MPDR) was developed at Michigan State University and is commercially manufactured by Wavemat Inc [3.1] as their model 325iTM. This ECR source and the other required components such as the main processing chamber, the vacuum system, the microwave power source, the computer controls, the rf biasing etc. are housed together in one embodiment and manufactured by PlasmaQuest Inc. [3.2]. This whole plasma etching system is commercially identified as the PlasmaQuest model 357 W plasma system and is schematically shown in Fig 3.1. The discharge in this reactor is confined by a 25 cm diameter microwave-transparent quartz bell jar. The height of the cavity applicator can be adjusted by varying the sliding short position which gives the user a freedom to choose the vertical dimension of the cavity and in principle fix a resonant mode for a particular processing run. Usually an appropriate resonant mode for ECR coupling was pre-established by manually changing

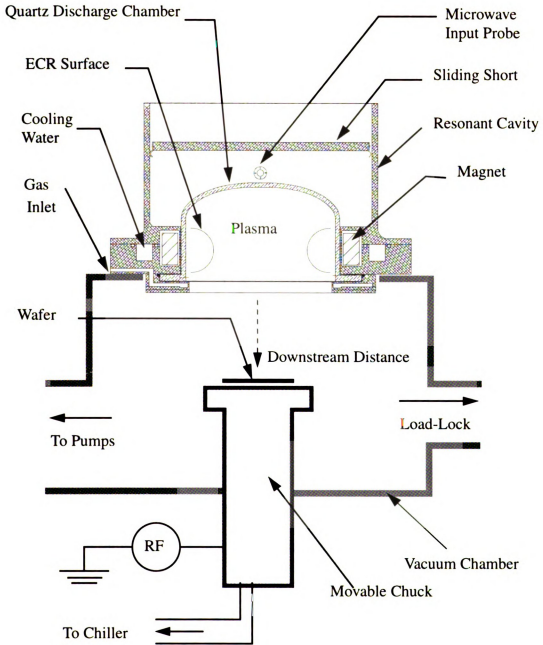


Figure 3.1: MPDR 325i -An ECR System with 25 cm discharge diameter

the short position and was not disturbed during an experimental run. The cavity is fixed to the stainless steel main processing chamber with high vacuum seals. The main chamber and the bell jar together form an enclosure for the plasma species. This part of the reactor almost always stays under high vacuum which is maintained by a roughing pump and a turbomolecular pump. The roughing pump takes the pressure down from an atmosphere to around 100 mtorr, when the turbo pump further brings it down in the range of microtorr or below. The turbo pump and the roughing pump are connected in sequence one after the other. The outlet for the turbo pump is called the foreline and is the inlet to the roughing pump. Under normal condition, when no processing is done, no gas flows through the cavity and the chamber remains under a high vacuum called the base pressure. The base pressure is monitored by a cold cathode gauge and usually for our system, the base pressure is around ~ 1 micro-torr. However, with gas flows during processing, the pressure inside normally rises to the mtorr range and is monitored by a Pirani gauge. During processing, the chamber pressure is automatically established at the user-set total processing pressure which comprises of the proper partial pressures of the gases of choice. This is done by an automatic control system which reads the measurements of the main chamber pressure and adjusts the throttle valve opening. The throttle valve is located in between the main chamber outlet and the inlet of turbomolecular pump. When the system is in standby between runs, the throttle valve remains open to its maximum and the turbo pump maintains the system at its base pressure.

Our etching system has a microwave power source of maximum power output of 1.5 KW at 2.45 GHz frequency. The nature of electromagnetic field patterns created inside the cavity are determined by the cavity dimension or the position of the sliding short. To

create and maintain a discharge in a preselected resonating mode, both the sliding short and coupling probe length may be adjusted to tune the discharge to a matched operating condition [3.3] and obtain minimum reflected microwave power. The microwave energy is primarily absorbed by the ECR heating mechanism described in chapter 2. To create the necessary static magnetic field, twelve rare-earth magnets are equally spaced in a circle around and adjacent to the quartz chamber. The magnet pairs are arranged on a soft iron keeper with alternate poles forming a twelve pole multipolar static magnetic field across a radial plane. The required static magnetic field at 2.45 GHz can be easily calculated as:

$$v = \frac{\omega}{2\pi} = \frac{eB}{(2\pi)m_e} \Rightarrow B = \frac{2.45 \times 10^9 \times 9.1 \times 10^{-31} \times 2 \times \pi}{1.6 \times 10^{-19}} = 875 \text{ Gauss} \quad (9)$$

Each magnet pole pair that is used in this reactor produces a pole face maximum field strength of 3000 Gauss which is well above the 875 gauss line required for coupling the microwave energy at the excitation of 2.45 GHz. The strength and the position of these magnets form a magnetic field surface of 875 Gauss approximately 1 cm inside the discharge zone and results in a three-dimensional radial ECR surface inside the chamber [3.4].

A water cooled, 13.56 MHz rf biased chuck having a freedom of movement along the z-axis is housed inside the vacuum chamber. The wafer sits on this movable stage during processing. The chuck can stay in two different locations, one is called its home position where it rests between processing runs and the other is a user-fixed higher position to which the chuck moves up before the beginning of a run and remains till the end of etching. The downstream distance is generally defined as the distance between the generation region of the bulk plasma and the position of the wafer while processing. For our system,

the downstream distance is specifically measured from the bottom of the ECR magnet housing to the top of the chuck.

The rf bias is obtained from a 0-300 watt, 13.56 MHz variable rf power supply which is coupled to the chuck by a matching network. Once the ions and neutral species are created through the elastic and inelastic collisions with the ECR heated electrons, they diffuse in all directions including towards the chuck on which the processing sample sits. When the positively charged species diffuse close to the substrate, they are attracted by the independently applied rf bias. The independent rf bias on the chuck provides an additional control over the energy of the ionized species before they hit the surface of the substrate.

This ECR system is a dedicated etching apparatus and has a clear-lid load-lock extension chamber for loading and unloading convenience. The pressure of the load-lock chamber is maintained by a separate mechanical pump. The main chamber pressure is cycled between the base pressure and the processing pressure. It is not exposed to atmosphere. The load-lock chamber, which is a small chamber compared to processing chamber, takes considerably less time to cycle from vacuum to atmosphere for sample loading. Once the processing sample is placed on the wafer-dish inside the load-lock chamber, the pressure reduces to a pre-selected transfer pressure (~2 mtorr) and a robot arm carries the wafer inside the main chamber.

Similarly when the processing finishes, the wafer is brought back to the load-lock chamber by the robot arm, which is then sealed from the main chamber and taken up to the atmospheric pressure for unloading. Further details of operation of this machine are described in the following section.

3.1.2 Operation of the PlasmaQuest-Wavemat ECR Etching Machine

Our ECR system is a computer controlled machine and the etching conditions, including environment such as the composition of the etching gases and the flow rates, the pressure inside the chamber, the input microwave power, and the rf bias are specified by the user while programming a particular process. Also the steady state and the transient times for each process or sub-processes can be specified while programming [3.5]. For example, the run time for an experiment, or the separating time between establishing the gas flows and turning on the microwave power can be programmed. The machine can remain in one of four different states, namely the sleep, edit, run or diagnostics mode as selected from the main menu. Note that this software mode of the machine is no way related to the resonant mode of the cavity.

When no etching is done, the system stays in the sleep mode. At this time, the microwave and the rf power source remain turned off but the turbomolecular and roughing pumps run in order to maintain the base pressure inside the chamber.

In the edit mode, the process sequences are programmed which are then followed during the running of an experiment. The actual sequence is programmed by establishing various "screens" in the edit mode. Each screen in the edit mode, corresponds to specified gas flows, pressure, rf power and rf bias for a specified time duration. For a typical first screen, the gas flows are established at a pressure slightly higher than the processing pressure. This is useful because at higher pressure the higher collision rates among the electrons and gas molecules facilitate initiation of a discharge. Once the plasma is initiated, it is easier to sustain it even at lower pressure. Therefore, in most of our experiments, the plasma is ignited at a higher pressure (about 7-10 mtorr) and later brought down to the processing

pressure (around 1-5 mtorr). Once the gas flows are established in screen 1, an appropriate forward microwave power is specified for screen 2. While executing this step in the run mode, a plasma glow should appear if the sliding short position and the probe length is not too far away from the tuned position. After allowing a short interval for settling the transients, the main chamber pressure is brought down to the desired processing pressure in the third screen. In the fourth screen, rf bias is applied to the chuck, and the etch time is specified. Once the etch time is elapsed, all the power supplies and gas flows are programmed to zero in the final screen, screen 5.

In summary, during the execution of an etching experiment, first the load-lock is vented to atmosphere for loading the wafer and then the load-lock is pumped down. The load-lock is then purged with nitrogen and again pumped down. When the pressure is at the pre-set transfer pressure a separating valve between the load-lock and the main-chamber opens allowing a mechanical arm to place the processing wafer on to the chuck. The robot arm comes out of the main-chamber to its home position and the valve between the main-chamber and load-lock closes. The chuck goes up to a pre-selected height corresponding to a desired down-stream distance. The gas starts to flow and the pressure inside the main-chamber increases from approximately a microtorr to the user-specified pressure for initiating the discharge. The microwave power is turned on next and the cavity is tuned manually if required, for the plasma to appear. The main chamber pressure then goes down to the processing pressure and the probe length is manually varied to ensure maximum power input. The etching process continues for the specified amount of time. Upon finishing the processing, the chuck returns to its home position, and the valve between the load-lock and main-chamber opens. The robot lever goes inside the main-chamber to

collect the sample. When the sample returns to the load-lock chamber, the chamber is vented to an atmosphere for unloading the sample. At this point, the machine can either be re-used for another run or made to exit the run mode.

The diagnostic mode is usually not used on a regular basis. The utility of this mode is in detecting faults or correcting the machine when it malfunctions. This mode gives the user a lot of freedom over the drivers and controllers. However, it is advised not to use this mode if the user is not very confident of the details of process sequences, because the system might be damaged if wrong commands are placed.

Some more system related general safety issues are addressed in Appendix A.

3.2 Description of Other Related Instruments

- *Cleanroom, Wet Station and And Ancillary*

A class 1000 cleanroom situated in C16, Research Complex for Engineering, was used for most of the research. Several essential equipment items for our research including the ECR plasma reactor, an ellipsometer, a microscope, a spinner, different kinds of furnaces and a mask aligner are housed here. Except for the ECR system, the individual equipment items are housed in class 100 individual work stations. A class 100 wet station with a hood for safe chemical handling is also provided inside the cleanroom.

- *Ellipsometer*

A Gaertner WaferscanTM (Model: L115B) ellipsometer was used for measuring the

thickness of various spin-on transparent layers on the top of a diamond or diamond coated sample. The principle of operation involves illuminating the surface of a sample with monochromatic light having a known and controllable state of the polarization and then analyzing the polarization state of the reflected light. The WaferscanTM ellipsometer uses a Helium-Neon, 1 mw, 6328 Angstroms, laser as the monochromatic source of light [3.6]. The position of the stage containing the wafer can be linearly and angularly adjusted such that the intersection of the incident, and reflected optical axes fall on the surface of the wafer. A computer is used for recording the photo-detector-converted output data to finally calculate the thickness of the transparent layer. However, for finding the thickness of the layer, knowledge about the refractive index of the coating material is required. For all measurements, the two angle method at 50^o and 70^o incident angles, was chosen.

- *Chemical Balance*

Though natural diamond in pure form has an excellent transmission of light in the visible spectrum, the polycrystalline CVD diamond samples that we processed are not perfectly transparent. Rather they range from being translucent to black, so the optical devices such as an ellipsometer can not be used to precisely determine the etch rate of diamond. Also for many of the samples, the polycrystalline surface is too rough to allow ellipsometry.

The alternative approach taken to measure the average etch rate over the area of the sample was simply to weigh samples before and after etching. From the weight difference the etch rate was then computed using the simple expression stated below:

$$\text{Etched Thickness} = \frac{\text{Weight Difference}}{\text{Surface Area X Density of Diamond}} \quad (10)$$

For all our calculations, the density of diamond is assumed to be 3.515 g cm^{-3} . Since the samples that we processed for our experiments had regular geometrical shapes, such as circular or rectangular, the surface area of these samples was well known in all cases.

A chemical balance (Model: Sartorius Balance A 2005) located in the Composite Materials and Structure Center Laboratory, Research Complex For Engineering was used for weighing samples. This balance has a digital display with a read-out resolution of 0.1 mg.

- *Micrometer*

The measurement of etch rate using weight method is only good for determining the average etch rate over the whole area of the sample, but it is not sufficient to establish whether the sample is preferentially etched in any location. A micrometer (Model: - Scherr-Tumico-Inc. St. James, Minn. USA) was used to verify the uniformity of the etching process at MSU. For measuring the 100 mm wafers, a deep throat micrometer (Model: Mitutoyo 389) was used by colleagues at Norton Diamond Film. Different types of attachments to the micrometer, namely ball and cone and flat end were used to improve the measuring accuracy. Finally no attachment to the micrometer was chosen giving an approximate measurement accuracy of $\pm 10 \text{ }\mu\text{m}$.

It is noted at this point that the uniformity is generally an important criterion to make an etching process useful in production. However, if the diamond wafer in the as-grown state is non-uniform in thickness it may be desired to intentionally produce non-uniform

etching to achieve uniform thickness. This is discussed further in chapter 6.

- *Dektak Profilometer*

A Dektak profilometer (Sloan Model: II A) located in the Open Laboratory at the Department of Physics, was mainly used for measuring the surface roughness (R_a) of a sample. The profilometer traces the surface of the sample with a floating diamond needle that records the z-axis fluctuations. The R_a computed by the instrument is an average of line-of-sight measurements. The direction and the length of the trace is determined by the operator where the scan length can be a maximum of 1 cm.

- *Optical Microscope and Scanning Electron Microscope*

Imaging is important for surface analysis of diamond films. Details of different approaches for imaging characterization of diamond films may be found in [3.7]. Various microscopy techniques were used in this research for quantifying the uneven sample surfaces. A simple optical microscope, manufactured by Zeiss, (Model Axioskop), was used for observing and taking micrographs of the diamond samples in order to characterize surface morphology. The eye-piece of the microscope has a fixed magnification of 10 and the objective magnification can be varied to 2.5X, 10X, 50X, and 100X depending on choice of the lens. The 50X and 100X objectives have differential interference contrast or Nipkowski capability. The microscope can also be used for an estimation of the z-axis fluctuation on the surface.

However, the optical microscope was often not adequate for viewing the detailed

structure of the surface. Scanning electron microscope is therefore the most widely utilized technique to inspect the surface morphology of diamond. SEM operates by scanning a focused electron beam over a surface and sensing the secondary electrons emitted from the surface. The electron beam can be focused to an extremely small diameter (in the range of 10-20 nm). This beam size is responsible for the resolution. The sample surface topography is magnified into an image on the monitor. SEM has many advantages over optical microscope in its high magnifications (in the range of 50X-40000 X), high resolution (2.5 - 10 nm), its extra-ordinary depth of field (500 times greater) which results in three dimensional imaging.

A JEOL, JSM-35 C SEM was used for getting views of the detailed features at 1000X and 10,000X on the surface of the free standing diamond samples. Since diamond is a non-conducting material, the samples in some cases were pre-coated with a gold film. The film was then connected electrically to the conducting substrate surface with vacuum compatible graphite paints to avoid the charging problem while taking the micrograph. The SEM facility is available in the Electron Optics Center at the Pesticide Research Center of Michigan State University.

- *Spinner*

A spinner manufactured by Headway Research Inc. [3.8], located inside the clean-room, was used for coating the samples with spin-on layers. Photoresist, spin-on-glass, titanium silicate etc. were spun on the top of the process wafer. The spinner can rotate at very high speed (about 20,000 rpm) and the time for rotation can be adjusted to a maximum of 120 s [3.9]. In most cases, spinning work for this research required 3000 rpm

for 30s.

Photoresist has some inherent hazardous characteristics, so the spinner needs to be placed under a proper ventilating hood. All necessary precautions should be followed before using the spinner since spinner can rotate at a dangerously high speed.

- *Mask Aligner*

The mask aligner, as the name suggests is generally used for aligning an optical mask to an existing pattern developed on the process wafer from previous operational steps. Normally the photoresist layer laid on the top of the wafer surface is exposed to ultra-violet light through the mask for a pre-decided duration of time which causes the photoresist to harden or soften depending upon the nature of the photoresist. Then the soft part of the photoresist is etched followed by the etching of an underlying material. This is how a pattern is conventionally transferred during the lithography [3.10]. For our experiment, a contact printing mask aligner (Model: Karl Suss MJB3) was used which has three independent (e.g, x, y and θ) controls for moving the wafer holding chuck relative to the mask. The process wafer mounted on the chuck is tightly held by the vacuum. The relative positioning of the wafer can be precisely adjusted manually by looking at the TV monitor. When the alignment is complete the mask and the wafer are clamped together for the ultraviolet light exposure. The UV light source can operate either in constant illumination or in constant power mode. The rated maximum output power for this UV lamp is 350 W. In most cases, the constant power mode was chosen for operation [3.11]. The mask aligner was used in this research for patterning photoresist through a mask for selective etching studies. It was also used for UV-hardening photoresist layer for planarization studies.

The main hazard associated with the mask aligner is the exposure to the UV radiation, hence appropriate precautions are advised before using the mask aligner.

- *Ultra-sonic Cleaner*

The ultrasonic cleaner, (Model: Branson 1200) was found to be extremely useful for cleaning graphite paint from diamond samples. The graphite paint, being a conductive adhesive was used for gluing small diamond samples to a silicon wafer so that they could be mounted onto the chuck of the ECR system. After the etching run, the remaining carbon paint beneath the samples needed to be ultrasonically cleaned with acetone. As the average diamond etch rate was calculated from the weight difference of diamond, cleaning played an important role for getting accurate results.

It is important to mention here that water in the ultrasonic cleaner that surrounds the beaker containing the graphite-painted diamond in acetone should always be maintained at the specified level. Water helps cool the vibration generated heat and since acetone is flammable, care must be taken to avoid fire hazards.

The ultrasonic vibrations generated from this equipment were also used for mixing chemicals for our research t.

- *Heating Apparatus*

There are several kinds of heating apparatus in the cleanroom. Hot plates (manufactured by Corning) are normally used for heating the chemicals etc. to a maximum of 150°C. Closed heat chambers can reach up to 300 °C. To go to higher temperature

treatment a diffusion furnace (manufactured by Thermo Systems) was used which can

operate between 400 °C and 1400 °C.

For the diffusion furnace, the furnace environment can be controlled with the appropri-

ate choice of gas (such as nitrogen, oxygen etc.). The maximum flow rate of any is about 5

liter/min.

- *Raman Spectroscopy*

Raman Spectroscopy is based on inelastic light scattering arising from the interactions

of photons with phonons. Raman scattering has been very useful for detecting the exist-

ence of diamond and studying the purity of diamond. It is very sensitive to the nature of

the carbon bonding, therefore the presence of various types of carbon bonding can be dis-

tinguished using this method. The first order peak of the diamond is located at 1332 cm^{-1}

[3.12]. Surface etching of diamond with different plasma environments may cause the

conversion of diamond into graphite or into other complex compounds. Hence it is

extremely important to detect and confirm the purity of diamond after processing. This

holds also true for the selective etching in case of the diamond coated ICs. The Raman

spectroscopy used in this research, is located in the Optics Laboratory of the Electrical

Engineering Department.

Laser radiation is an inherent hazard associated with the Raman spectroscopy, hence

necessary precautions such as eye-protection need to be taken before using the Raman

spectroscopy.

- *Probe Station and HP parameter Analyzer*

A probe-station and a HP 4145B semiconductor parameter analyzer in conjunction were used for measuring and documenting the IC device characteristics with regard to selective etching of diamond overcoated layers on ICs. This set-up is located in the Electronic Devices and Circuits Laboratory, of the Electrical Engineering Department.

From selected ICs on the wafer, the I-V characteristics for the resistors and the Gummel plots for the transistors before the diamond coating and after diamond patterning were made. By comparing these plots, the functioning of the devices after selective etching was confirmed.

Chapter IV. Theory of Etch Processes

Many diverse and complex phenomenon take place in a plasma etching process which are not fully understood yet. However, some key steps of plasma etching are identified and are broadly outlined here:

- 1. Generation of the species in the discharge
- 2. Diffusion of the species towards the substrate
- 3. Adsorption of the reactants on the substrate surface
- 4. Surface reactions
- 5. Desorption of the reaction products from the surface
- 6. Diffusion of the volatile etch products to the outlet of the chamber
- 7. Disposal of the etch products to the environment

This chapter mainly focuses on the details of steps 3, 4, and 5, i.e., adsorption, surface kinetics of etching and desorption of products. Other related mechanisms such as the generation of species in step 1, and diffusion of species in step 2 and 6 are only briefly discussed.

In some plasma processing, reaction products can be quite hazardous and proper gas disposal measures must be taken following standard guidelines and procedures. Step 7, the disposal of etch products to the environment is therefore an important issue and is usually

addressed when an etcher is initially installed for specific etching purposes. For our processing, carbon in diamond form is etched in plasma whose feed gases mostly include oxygen and SF₆. In addition, C containing compounds result from substrate etching. Therefore, the possibility exists for the production of CO, COF₂ and F₂, all of which are extremely toxic.

Chapter four begins with the introduction of different types of plasma etching processes in section 4.1. Section 4.2 discusses the diffusion, adsorption and the desorption of neutral species. Section 4.3 reviews the reaction rate constants and the concepts of elementary reaction processes. It also describes the simple first and second order reaction kinetics. Section 4.4 attempts to theoretically understand the reaction processes involved in oxygen ion-assisted diamond etching. Some fundamental reasons for etch rate limitations of diamond oxidation are identified.

4.1 Different Types of Etching

Four types of low pressure plasma processes are commonly used to remove material from the surface of a substrate. These etching mechanisms are often identified as sputtering, pure chemical etching, ion energy driven etching (also called reactive ion etching), and ion inhibitor etching. A brief introduction to each type of etching is given here; the details of these process may be obtained from [4.1, 4.2].

4.1.1 Sputtering

Sputtering is basically a non-selective, physical process where the kinetic energy of the **bombarding** charged particles is simply transferred to the surface molecules to liberate

the atoms. A noble gas which does not react chemically with target substances is often chosen to create a discharge for sputtering. These non-reacting ions impact on the surface, eject the atoms from the surface layer, and form the sputtered product. The mechanism is illustrated in Figure 4.1.

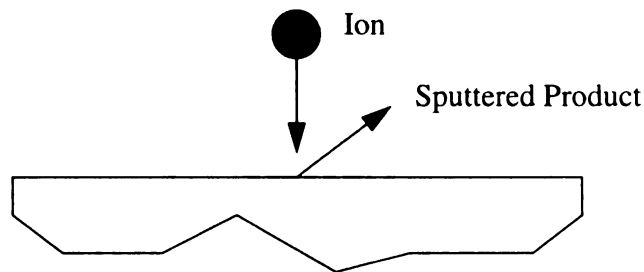


Figure 4.1: Sputtering

The sputter rate is directly dependent on the surface binding energy and the masses of the targets and projectiles. In general, at energies above 20-30 eV, heavy particles can sputter atoms from a surface. However, the sputtering yield, defined as the atoms sputtered per incident ion, increases rapidly with energy up to a few hundred volts. Sputtering is an anisotropic process and is strongly sensitive to the incident angle of the ions to the substrate. Sputtering is used for both etching and deposition. In case of sputter-enhanced deposition, the sputter product is collected on another target for growth.

4.1.2 Chemical Etching

A second etch process shown in Figure 4.2 is purely chemical etching. The discharge **supplies** the gas phase etchant species, including the radical atoms and molecules, that **chemically** react with the target surface and form gas phase products. It is important to

choose proper etchant gas species such that the chemical reaction yields gas products, that are volatile and preferably non-hazardous.

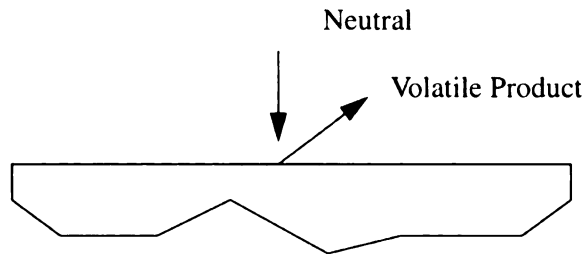


Figure 4.2: Pure chemical etching

Usually this process is highly selective which means that the same discharge can produce extremely different etch rates for different substances. For example, oxygen atoms chemically react with carbon but do not attack SiO_2 , so if a substrate contains both carbon and SiO_2 , the carbon containing part of the substrate etches at a significantly faster rate than the other part in an oxygen plasma and thus etch selectivity is achieved.

Pure chemical etching, is almost in all cases, isotropic since the gas phase etchant arrive at the substrate with near uniform angular distribution. It can be anisotropic if the crystal orientations of the substrate promote preferential etching in certain direction. Since more than 99% of the species in a discharge are neutrals, the flux of the neutral species to the substrate may be significantly large, resulting in a very high etch rate. However, the etch rate for a given material, is not limited just by the arrival of the etchant species to the substrate but also by the complex set of reactions leading to formation of the etch products and their desorption.

4.1.3 Ion-assisted Etching

In ion assisted etching the discharge supplies both neutral chemical species and energetic ions to the surface. The combined effect of neutral etchant species and energetic ions in producing etch products can be much larger than that produced by either pure chemical etching or by sputtering alone. Ion assisted etching is a combination of chemical and physical processes and is shown in Figure 4.3.

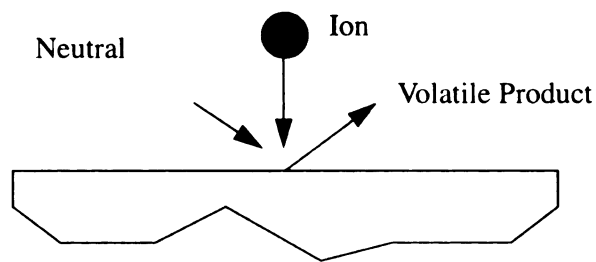


Figure 4.3: Ion-assisted etching

Products from chemical surface reactions can tend to stick to the surface shielding the entrance for the fresh etchant species. For ion-assisted processes, the addition of high energy ion flux to the neutral flux helps the etching mechanism to go in two ways. First, it expedites the desorption of etch products from the surface, and secondly it ruptures the surface bonds exposing the atoms of the substrate to the etchant species. These dangling bonds often work as better active sites. Generally the etch rate increases when the ion energy is increased beyond a certain threshold level determined by the properties of substrate e.g., the bonding energy. However if the ion energy is increased sufficiently then a saturation stage is reached because the rate of adsorption of the species and the formation of etch products limit the etch rate. We know from the previous discussion that chemical

etching can produce very selective etching and that the physical etch process produces extremely anisotropic etching. Ion-assisted etching is a combination of both the physical and chemical processes. Hence the trade-off between anisotropy and selectivity become an important consideration while designing an RIE process although the etch rate in reactive ion etching is often much larger than either sputtering or pure chemical etching.

4.1.4 Ion-Enhanced Inhibitor Etching

Ion-enhanced inhibitor etching involves the use of the inhibitor species. The discharge in this case supplies the etchant, the energetic ions, and the inhibitor precursor molecules that adsorb on the substrate to form a protective layer or polymer film. The etchant is chosen to produce a high chemical etch rate of the substrate in the absence of either ion bombardment or the inhibitor.

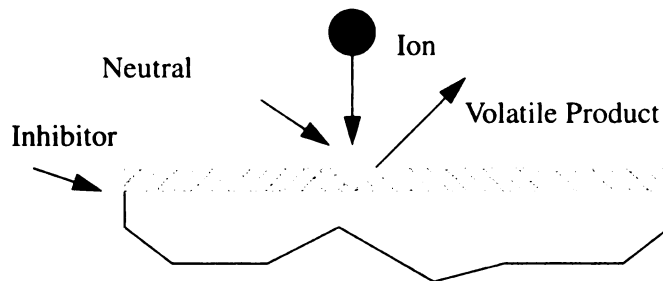


Figure 4.4: Ion-enhanced inhibitor etching

The ion bombardment flux prevents the inhibitor layer from forming or clears it as it forms, exposing the surface to the chemical etchant. Where the ion flux does not fall, the inhibitor layer protects the surface from etching. This is illustrated in Figure 4.4. Ion enhanced inhibitor etching is widely used in the semiconductor industry for etching

anisotropic trenches, where the vertical sidewalls need to be protected simultaneously while the etching proceeds at the trench bottom, as shown in Figure 4.5.

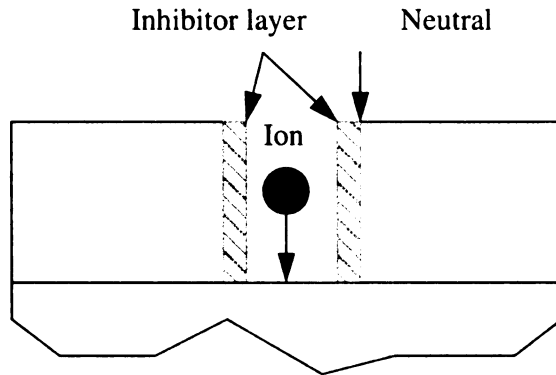


Figure 4.5: Trench etching

4.2 Plasma and Surface Interaction

The presence of the excited neutrals and charged species in addition to the non-excited atomic species often give rise to very unusual chemistries in plasma. Many reactions that are not seen otherwise are seen in a plasma environment. Also many conventional reactions occur at a relatively lower temperature and at a different reaction rate inside the plasma discharge.

In general, two different set of chemistries exist in plasma processing, one in the discharge and the other at the surface of the work-piece. The discharge chemistry is responsible for maintaining a steady state concentration of different charged and neutral species inside a bulk plasma. However, it is the interaction of plasma with the surface of the substrate that provides the actual etching of the work-piece.

4.2.1 Generation of Species

In plasma reactors, energies in non-thermal forms e.g, rf, microwave etc., are put in to sustain the discharge mechanism. As described in chapter 3, the input energy is primarily coupled to the electrons and then transferred to the neutrals and ions through elastic and inelastic collisions. Scattering, excitation through momentum transfer, and ionization are some of the important phenomena that result from collisions. Thus collisions play a significant role in generating and maintaining different species in the plasma and in determining their energy distributions.

Broadly three distinct set of species, referred to as ions, neutrals and electrons interact both physically and chemically inside a discharge resulting into an emission of photons which appears as a glow of the discharge. Numerous chemical reactions that occur inside the plasma are responsible for deciding the steady state density of each individual species.

The complexity and the number of the elementary reactions drastically increase when more than one processing gases are flown into the chamber. Non-monoatomic gases add further complications to the discharge chemistry and the energy distribution functions. Extensive numerical simulation is required to theoretically predict even in part the different ionized and excited species that constitute a complex laboratory plasma. Therefore, experimental measurement procedures, known as plasma diagnostics, are applied to identify and characterize various species in a discharge. Electrical diagnostics such as Langmuir probe measurements and optical diagnostic such as fluorescence and spectroscopy are some of the commonly used techniques. The probe measurement techniques are largely used for knowing the average energy of the electron and ions, whereas actinometry is used mainly for identifying the existence of different ions and excited neutrals in a

discharge. Unlike the electrical measurement techniques, most optical methods do not introduce local perturbations in plasma and this non-destructive, non-interfering nature of this diagnostics is often considered to be an advantage. Details of all these techniques may be found in [4.3, 4.4, 4.5].

However, even after combining the information obtained experimentally, modelling a discharge in reality remains quite a challenge. To briefly illustrate the degree of difficulty associated with the discharge chemistry, we consider here the diatomic gas oxygen which is used for our plasma processing experiments. According to [4.6] in a pure oxygen discharge, there can be significant ground state concentrations of O, O₂, O₃, O⁺, O₂⁺, O₄⁺, O₃⁺, O⁻, and electrons, as well as metastable states such as ¹D and ¹S states of O ¹Δ_g and ¹Σ_g states of O₂ molecules. Determining the cross-sections for the binary processes among these species are quite difficult and many of these cross-section values are yet to be precisely measured or calculated. Here the cross-section for a binary process implies the cross-section associated with momentum transfer or ionization of any two colliding species, say O₃⁺ and O₂ for example.

Besides the complexity generated from the physical interactions such as collisions among numerous oxygen ions and excited atoms or molecules, different types of chemical reactions such as dissociation, recombination, attachment, excitation, resonant and non-resonant charge transfer, etc. complicate the mechanism of species generation further. Moreover, in actuality, our plasma for diamond etching is not a pure oxygen plasma, rather it is composed of three gases, argon, oxygen and SF₆.

Electron temperature and the species densities at the sheath and the substrate surface

are the main diagnostics results that we are interested in for knowing the etching mechanism and the etch rate. However, plasma diagnostics was not included in this dissertation research, and for all our theoretical calculations we rely on reasonable assumptions and approximate values obtained from the available literature.

Later in chapter 5, we will see that even with many simplified assumptions our calculation of diamond etch rate in oxygen plasma roughly matches the experimental results using plasma parameters within the range reported by other investigators.

4.2.2 Diffusion of Species

Diffusion is a net flow of particles resulting from the spatial variation of particle concentrations in an environment. This common phenomenon has been studied and modeled over many years for different particles e.g. atoms, molecules, ions, electrons, etc. in different environments, e.g. solids, liquids, gases, and plasmas [4.7, 4.8, 4.9]. Study of diffusion of species in plasma has drawn significant attention of the researchers in the area of plasma processing since diffusion is the only means of transportation for neutrals in plasma and an important means of transportation for charged species. Also it often controls and limits many etch results e.g. etch rate and etch uniformity.

For effective etching to continue under steady state, the reactant species travel from the generation region to the substrate surface and the etch products leave the surface and travel through the bulk plasma to the outlet of the process-chamber where they are pumped out as gaseous disposals. The mechanism of the charged particle diffusion in plasma is different from that of neutrals and a separate model called ambipolar diffusion model is used to describe the combined diffusion motion [4.10] of the ions and electrons. The ambipolar

diffusion mechanism is elaborated later in chapter 6 and this chapter briefly discusses the diffusion of neutral species following the discussion given in [4.11].

Random thermal motion is responsible for diffusion and the direction of the flow is determined by the gradient of concentration. The mathematical description of a diffusional flow is obtained from Fick's expression.

$$\Gamma_A = -D_{AB}\nabla n_A \quad (11)$$

Γ_A is the flux of particles of type A, D_{AB} is the effective diffusion coefficient of neutral species A due to the collisions with B particles, and ∇n_A is the gradient of density for particles A. The effective diffusion coefficient can further be expressed as:

$$D_{AB} = \frac{k_B T_g}{M_R \nu_{AB}} \quad (12)$$

where k_B is the Boltzmann's constant, M_R is the effective reduced mass and ν_{AB} is the collision frequency. When the particles collide with each other, they scatter both in coordinate space and in velocity space. There is a net flux from regions of higher particle concentration to regions of lower particle concentration. Often the assumption of a Maxwellian distribution of particle velocities is used for simplification of mathematical expressions. The concept of collisional frequency can be related to the velocities of the particles following the expression given below:

$$\nu_{AB} = n_B \langle \sigma_{AB} v_{AB} \rangle \quad (13)$$

where n_B is the density of the B molecules, σ_{AB} is the collisional cross-section of A as seen by the B molecule, and v_{AB} is the relative speed of the A molecule with respect to

the B molecule. $\langle \sigma_{AB} v_{AB} \rangle$ represents the average of the product of collisional cross-section and random velocity over the velocity space. The actual cross-sections are non trivial to compute as they are the functions of many parameters such as the temperature, the scattering angle, the physical distance between colliding species etc. and it becomes more difficult to calculate if the colliding species are charged particles because the presence of the additional Coulomb force complicates the phenomenon. Important gas kinetic cross sections can be found from Tables [4.12].

However for rough calculations of diffusion coefficients, charge-free species are assumed to be hard spheres with constant cross-sections. This simplifies the collision frequency term and the average of $\langle \sigma_{AB} v_{AB} \rangle$ becomes $\sigma_{AB} \langle v_{AB} \rangle$. Further simplification follows from the assumption of a Maxwellian distribution of neutral velocity as stated before. Thus the collisional frequency is finally expressed in terms of more fundamental experimental quantities such as gas temperature T and the effective neutral mass M_R .

$$v_{AB} = n_B \sigma_{AB} \langle v_{AB} \rangle = n_B \sigma_{AB} \left(\frac{8k_B T}{\pi M_R} \right)^{\frac{1}{2}} \quad (14)$$

Often $\lambda_{AB} = \frac{1}{n_B \sigma_{AB}}$ is defined as the mean free path which is the average distance

travelled by a particle before colliding. With the assumption of hard spheres,

$\sigma_{AB} = \pi(r_A + r_B)^2$, where r_A and r_B are the mean radii of A and B particles. In the case

of a homogeneous environment consisting of only one type of particles, the collisional

cross-section becomes $\sigma = 4\pi r^2$ and the effective reduced mass M_R becomes $M/2$ where

M is the mass of the particle and r is the radius of the particle respectively.

It can be easily seen that as the number of different species increases inside a discharge, the diffusion mechanism becomes more complex. Usually a laboratory plasma is in fact made up of more than one processing gases.

However, it is noted that for the low operating pressures in ECR processing, the mean free paths of the species is significantly large, on the order of a few cms, and an almost collision-free environment is achieved. In that case, crude approximations of an effective collisional cross-sections do not affect the calculation of the species flux much, and the calculated etch rate more or less agrees to the experimental result.

4.2.3 Adsorption and Desorption

Once the etchant species reach the vicinity of the surface by diffusion, they can with some probability stick to the surface by a phenomenon called adsorption. This is a key beginning step for the surface reactions that eventually produce volatile etch products. The etch products leave the surface exposing the next layer of the substrate atoms for etching. Thus desorption, the reverse process of adsorption also plays a crucial role for the etching process to continue. In order to understand an etching mechanism and improve the plasma etch rate for a certain material, both adsorption and desorption need to be carefully studied since they often become the limiting steps for the etch rate for a particular surface processing. Since the majority of the species that arrive at the surface are the neutrals, we concentrate here more on the adsorption phenomenon of neutrals.

Adsorption is due to an attractive force between an incoming molecule and the substrate surface and can be of two kinds: Physisorption and chemisorption. Physisorption is an exothermic process and is due to the weak Van-der-waal attractive force between a

molecule or atom and the surface [4.13]. When an atom comes close to the surface, typically within a distance of 0.1-0.3 nanometer, the electrons of the atom and the nucleus of the surface material interact and form a potential well. Atoms trapped in the potential well, remain near the surface oscillating about a mean equilibrium distance. These physisorbed molecules are very weakly bound to the surface and can diffuse rapidly along the surface [4.14].

Chemisorption [4.15] is due to the formation of a chemical bond between the atom or molecule and the surface. The reaction is strongly exothermic. Chemisorption of a molecule having multiple bonds can occur, for example, with breaking of one bond as a molecule bonds to the surface. A molecule with a double bond shown as, $A = B$ is chemisorbed on a surface S when one of the bonds break and the bonding rearranges as $S - A - B - S$. Often $S - A - B - S$ is denoted by $AB:S$ and the chemisorption process is described by:



In the case of single-bonded molecules the bonds are often torn apart as they form bonding to the surface. This is shown in the following reaction equation.



This process of chemisorption following the breaking of a molecule into elemental atoms is called the dissociative chemisorption and requires two adsorption sites. Physisorption and chemisorption normally simultaneously exist in an etching mechanism, with different regimes favored by individual process depending upon the surface temperature and the nature of the energy curves that follows from the potential well formed between the incident atoms and surface. Molecules that impinge on the surface cannot be adsorbed

unless both the conservation of momentum and energy is achieved. The molecules lose their energy in the collision with the surface and those molecules for which the normal component of the energy after collision becomes lesser than the required energy to overcome the potential well, get trapped.

Assuming the gas neutrals in plasma follow a Maxwellian distribution, the flux of the molecules incident upon the surface Γ_A can be expressed as $\frac{1}{4}\tilde{v}_A n_{AS}$ where \tilde{v}_A is the mean speed of the molecules and n_{AS} is the gas phase volume density of the molecules at the surface. If s indicates the sticking coefficients, the chemisorbed molecules on the surface can be written as:

$$\Gamma_{ads} = s\Gamma_A = \frac{1}{4}s\tilde{v}_A n_{AS} \quad (17)$$

In general, the sticking coefficient is a function of the fraction of sites covered θ and the gas and surface temperature. However, when thermal equilibrium is maintained, both the surface and the gas molecules remain at the same temperature T . Generally chemisorption ceases after all the active surface sites are filled with adsorbate which roughly corresponds to a mono-layer of coverage. In absence of external means of creating sites, adsorption is then continued through the physisorption mechanism where the adsorbate trapped by physisorption diffuse along the surface to a vacant location beneath the mono-layer. Thus many mono-layers can be physisorbed and a continuous condensation of adsorbate can occur. However, the process comes to a steady state when the desorption and adsorption balance each other. Under this condition, the stoichiometric equation modifies as:



For an ion-assisted etching, the kinetic energies of the incident ions are transferred to the adsorbed molecules upon bombardment and these molecules gain enough energy to leave the surface. To balance the desorption rate under steady state, the adsorption rate increases and thus a significantly higher etch rate is achieved.

4.3 Elementary Reaction Kinetics

The phrase “chemical kinetics” is often abbreviated as kinetics and is used to describe the quantitative study of change in concentration or pressure of reactants and products with time brought about by the elementary chemical reactions. A reaction is called elementary if it directly proceeds in one step. In reality, the reactants may follow numerous possible intermediate steps before the end product is formed. A significant effort in chemical kinetics has been to determine the set of elementary reactions into which a given stoichiometric reaction can be broken. One type of important elementary reactions are decomposition reactions which are often unimolecular.



Bimolecular elementary reactions, like the one described below are also quite probable because they require only two molecules to come close together and react:



As the number of reactant molecules required for balancing a stoichiometric equation increases, the probability of that equation being elementary reaction goes down. At high pressure discharges, with higher concentration of gas molecules, some termolecular gas-phase reactions are also found to be elementary but in low pressure discharge these types of reactions are much less probable. However, an example of the termolecular reaction is

given below.



The reaction rate is an important parameter used for analyzing the kinetics of elementary chemical equations. It is commonly defined as the per unit decrease of density of one of the reactants or per unit increase of density of one of the products per unit time. Mathematically the reaction rate R for a gas-phase reaction can be defined as:

$$R = \frac{1}{\alpha_j} \frac{d}{dt}[A_j], \quad \text{For all } j \quad (22)$$

where α_j is the stoichiometric coefficients for the reaction and $[A_j]$ is the volume density (m^{-3}) of molecules of j th substance. For example, the reaction rates for the stoichiometric equation $3A + 2B \rightarrow C + D$ can be obtained as:

$$R = -\frac{1}{3} \frac{d}{dt}[A] = -\frac{1}{2} \frac{d}{dt}[B] = \frac{d}{dt}[C] = \frac{d}{dt}[D] \quad (23)$$

In case of surface reactions, the volume density $[A_j]$ is replaced by the area density of the j th molecule $[A_j']$ on the surface. In general, R has a complicated form but it simplifies for the elementary reactions. If we define the proportionality constants K_1 , K_2 and K_3 as the reaction rate constants, then the reaction rates for the elementary reactions given by the equation (19), (20) and (21) can be expressed as equations (24), (25) and (26).

$$R = \frac{d}{dt}[A] = K_1[A] \quad (24)$$

$$R = \frac{d}{dt}[A] = \frac{d}{dt}[B] = K_2[A][B] \quad (25)$$

$$R = \frac{d}{dt}[A] = \frac{d}{dt}[B] = \frac{d}{dt}[C] = K_3[A][B][C] \quad (26)$$

Since equations (24), (25) and (26) are linear differential equations of first, second and third orders respectively, the constants K_1 (s^{-1}), K_2 (m^3s^{-1}) and K_3 (m^6s^{-1}) are known as first-order, second-order and third-order reaction rate constants. These rate constants are not dependent on the densities of the reactant or the product molecules but are functions of the temperature. The thermal dependence of reaction rates is described by the Arrhenius expression:

$$K_T = K_O e^{-\epsilon/k_B T} \quad (27)$$

where K_T is the rate constant at a temperature T , K_O is a pre-exponential factor, ϵ is the activation energy and k_B is the Boltzmann's constant. Further details related to the chemical reaction kinetics can be found in number of books [4.16, 4.17].

However, to understand the etching related surface kinetics, the concepts of the elementary reactions and reaction rates are applied to gas-solid reactions. The simplest mathematical model for gas-solid reactions was first developed by Langmuir for a single site mechanisms which was later extended for dual site mechanism by Hanshelwood [4.18, 4.19]. Active site theory is the basis for this kinetics which proposes that the reactions occur at the favored sites on the surface. It also presumes that the surface is not fully covered by a mono-layer of adsorbed species and one atom or molecule is adsorbed per active site due to strong valence bond. The Langmuir kinetics theory further assumes the following conditions:

1. The surface is homogeneous, i.e., a uniform average activity can be defined over the entire surface. This assumption clearly requires an uniform distribution of sites.
2. No interaction occurs among the adsorbed species, i.e., the amount adsorbed has no

that

as W

an to

+

I

ing in

pract

disse

A

numi

begin

the re

admit

for mu

CO₂ a

increa

accepte

effect on the adsorption rate per site.

3. Surface migration is either non-existent or so rapid that only adsorption and desorption can be the rate-controlling mechanism.

It is important to mention here that the homogeneous, non-interacting surface implies that both the activation energy for adsorption E_a and desorption E_d remain constant in time as well as from site to site.

The next section utilizes the concepts of the Langmuir kinetics to develop a model for an ion assisted surface etching of carbon with oxygen only plasma.

4.4 Surface Kinetics of Ion-assisted Carbon Etching

In this section, we attempt to understand the ion-assisted mechanism of diamond etching in pure oxygen plasmas and find an expression for etch rate of carbon based on some practical assumptions. The approach presented here for development of this expression closely follows the method given in [4.20].

Although etching of diamond in oxygen plasma may be a relatively new topic of study, burning of carbon in molecular oxygen is a phenomenon known to mankind since the beginning of the civilization. Surprisingly, even after knowing this phenomenon for ages, the reaction mechanism of carbon and oxygen is not well understood. Whether direct oxidation of carbon yields CO or CO₂ or both as the primary products remained a question for many years [4.21, 4.22]. Finally researchers came to a consensus that both CO and CO₂ are formed as primary products from carbon-oxygen reactions and the CO/CO₂ ratio increases substantially with higher temperature and lower pressure [4.23, 4.24, 4.25]. An accepted model for calculating the ratio of CO/CO₂ from direct oxidation of carbon is

given by equation (28) [4.26]:

$$[CO]/[CO_2] = A e^{-\frac{E}{RT}} \quad (28)$$

At low pressures $A \cong 10^{2.5}$, and $E \cong 6 - 9$ kcal/mol. R and T in the above equation are the universal gas constant and gas temperature respectively.

In the case of ECR etching, the processing pressure is usually in the order of a few mtorr and the gas temperature is about 300 K. Therefore an approximate volume density ratio of CO to CO₂ becomes 300:1 which suggests that at low pressure very little CO₂ is directly formed from oxidation of carbon. CO₂ is rather formed in the gas-phase independently through the oxidation of CO. So we can simplify the problem of the finding carbon etch rate with oxygen ECR plasma by neglecting the formation of CO₂ from the chemical etching of carbon. We also assume that the necessary conditions for Langmuir kinetics hold true on the surface of carbon and the positive oxygen ions that strike the substrate either help in desorption of CO molecules or sputter the carbon atoms depending on where the ions are incident.

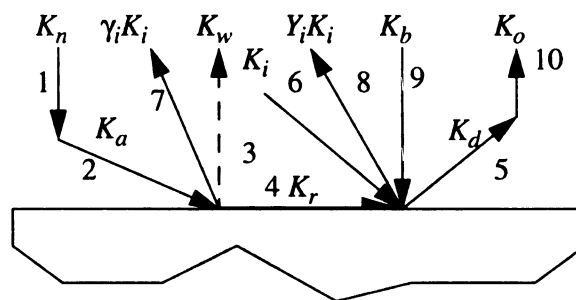
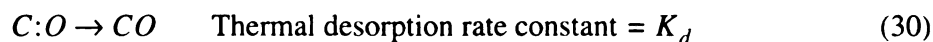
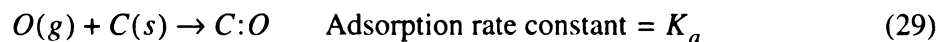


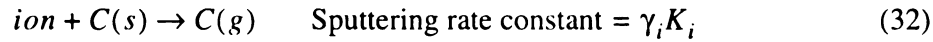
Figure 4.6: Details of RIE processes

Several important intermediate steps numbered as 1 through 10 in Figure 4.6 show different processes that take place between the generation of atomic oxygen in an oxygen plasma and completion of the etching process by producing CO. These processes are explained below along with their appropriate rate constants.

- 1: Diffusion of the etchant oxygen atoms to the surface at a rate constant K_n
- 2: Adsorption of O atoms on the surface at a rate constant K_a
- 3: Desorption of etchant species without reaction at a rate constant K_w
- 4: Reaction of O atoms with the surface C at a reaction rate K_r to form CO.
- 5: Thermal desorption of CO from the surface at a rate K_d .
- 6: Ions are incident on the surface at a rate constant of K_i .
- 7: Carbon atoms are sputtered at a rate constant of $\gamma_i K_i$.
- 8: Ions assisted desorption process at an effective rate constant $Y_i K_i$.
- 9: Adsorption of etch products in gas phase back to the surface at a rate constant K_b .
10. Diffusion of CO through the bulk plasma to be pumped out at a rate constant K_o

Following Langmuir kinetics we assume that all O atoms incident on the available sites react instantaneously with the surface carbon to form a surface bond. Therefore, step 3 is neglected and reaction rate K_r in step 4 is assumed to be very large. Also we neglect the processes such as 1, 9, and 10 that are not directly related to the surface kinetics and assume that the effective etching of carbon in oxygen plasma is given by the following four reactions:





Equation 29 describes the adsorption of O atom species on the surface, equation 30 features the regular thermal desorption phenomenon, equation 31 describes the ion-assisted desorption in case of reactive etching, and equation 32 represents the sputtering of carbon atoms due to high energy oxygen ion bombardment. The (g) and (s) notation refer to the gas and surface respectively and C:O indicates a surface carbon-oxygen bond. Here γ_i is the carbon atoms sputtered per incident oxygen ion on the uncovered carbon sites and Y_i is the yield of the CO molecules desorbed per incident ion on a fully covered surface in the absence of other desorption mechanism. Often Y_i is approximated by a simple model

$$Y_i \sim \eta \frac{E_i}{E_b} \quad \text{for } E_i \gg E_b \quad (33)$$

where E_b is the energy binding the CO molecule to the surface, E_i is the ion energy and η is the bond breaking efficiency factor where $\eta \leq 1$.

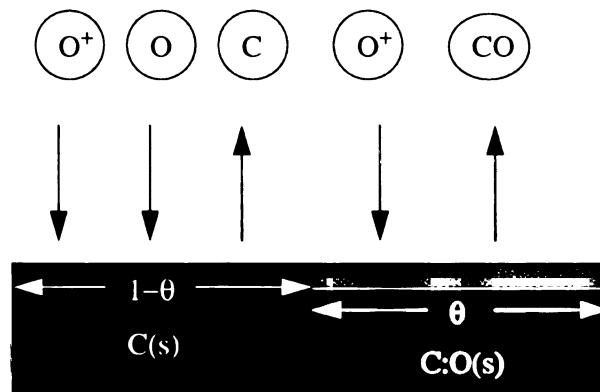


Figure 4.7: Reactive ion etching of diamond

Let us assume that the carbon substrate shown in Figure 4.7, has a surface site area-density n_o' of which θ fraction is covered with C:O bonds. Then the area-density for the uncovered carbon atoms and oxygen-bonded carbon atoms [C:O] on the surface becomes $n_o'(1 - \theta)$ and $n_o'\theta$ respectively. We assume that n_{OS} is the density of the oxygen atoms in gas phase near the surface of the carbon substrate and n_{iS} is the oxygen ion density at the boundary of the plasma sheath.

Reactive ion etching of carbon with pure oxygen plasmas is achieved in two ways; by forming the C:O bonds through the surface reactions and desorbing the CO molecules from the surface and by physically sputtering the carbon atoms by the positive ions of oxygen. Both these processes contribute to the removal of the carbon from the surface.

Here we first consider the etching mechanism following the formation of CO which is described by the equations 29, 30, and 31. The rate of [C:O] formation, and the thermal and ion-assisted desorption of [C:O] can be calculated using the relation given in equation 25.

$$\left. \frac{d}{dt}[\text{C:O}] \right|_{\text{formation}} = K_a[\text{O}][\text{C}] = K_a n_{OS} n_o' (1 - \theta) \quad (34)$$

$$\left. \frac{d}{dt}[\text{C:O}] \right|_{\text{thermal-desorption}} = -K_d[\text{C:O}] = -K_d n_o' \theta \quad (35)$$

$$\left. \frac{d}{dt}[\text{C:O}] \right|_{\text{ion-assisted}} = -Y_i K_i [\text{C:O}][\text{ion}] = -Y_i K_i n_o' \theta n_{iS} \quad (36)$$

Adding all the effects described by the above three equations, the rate of change of surface coverage can be calculated:

$$\left. \frac{d}{dt}[C:O] \right|_{net} = \frac{d}{dt}n_o'\theta = K_a n_{OS} n_o' (1 - \theta) - K_d n_o' \theta - Y_i K_i n_o' \theta n_{iS} \quad (37)$$

Finally equation 37 can be rearranged in the following form.

$$\frac{d\theta}{dt} = K_a n_{OS} (1 - \theta) - K_d \theta - Y_i K_i \theta n_{iS} \quad (38)$$

Applying the steady state condition $\frac{d\theta}{dt} = 0$, we can further simplify equation 38, and calculate θ .

$$\theta = \frac{K_a n_{OS}}{K_a n_{OS} + K_d + Y_i K_i n_{iS}} \quad (39)$$

The steady state CO desorption flux can be easily found by adding the two different desorption phenomenon (thermal and ion-assisted):

$$\Gamma_{CO} = (K_d + Y_i K_i n_{iS}) \theta n_o' \quad (40)$$

Now, we focus on the etching contributed by the sputtering of carbon atoms described by the equation (32). The rate of carbon sputtering can be calculated as:

$$\left. \frac{d}{dt}[C(s)] \right|_{sputter} = \frac{d}{dt}n_o'(1 - \theta) = -\gamma_i K_i [C(s)] [ion] = -\gamma_i K_i n_o' (1 - \theta) n_{iS} \quad (41)$$

The carbon atoms are ejected only when an energetic ion hits an uncovered carbon atom on the surface. $(1 - \theta)$ portion of the total substrate area on the surface sites is not covered with CO, therefore the flux of sputtered carbon atoms can be calculated as:

$$\Gamma_C = \left. \frac{d}{dt}[C(s)] \right|_{sputter} = \frac{\gamma_i K_i n_o' (1 - \theta) n_{iS}}{(1 - \theta)} = \gamma_i K_i n_o' n_{iS} \quad (42)$$

Usually the sputter-yield γ_i increases as the energy of the incident ions increases. The vertical etch rate is directly related to the flux of CO molecules and the sputter ejected

carbon atoms that are leaving the surface and is given by:

$$E_V = \frac{\Gamma_{CO} + \Gamma_C}{n_C} \quad (43)$$

where n_C is the carbon atom volume-density of the substrate. Combining and rearranging the equations 29, 30, 42 and 43, we obtain the vertical etch rate of carbon due to the formation of CO and sputtering of carbon atoms:

$$E_V = \left[\frac{n_o'}{n_C} \right] \left[\frac{1}{\frac{1}{K_d + Y_i K_i n_{iS}} + \frac{1}{K_a n_{OS}}} + \gamma_i K_i n_{iS} \right] \quad (44)$$

In order to calculate the total vertical carbon etch rate, the rate constants need to be evaluated from the plasma characteristics which can be approximately related to some of the plasma properties such as the electron and neutral temperatures, ion density at the sheath etc. From the previous assumption that all O atoms reaching the surface are immediately adsorbed, and the adsorption rate /site does not depend on the density of covered sites, we can find an expression for the adsorption rate coefficient K_a . This expression is given below:

$$K_a = \frac{\text{Average velocity of O-atom}}{\text{Surface density of open C-sites}} = \frac{\Gamma_o}{n_o'} \quad (45)$$

If a Maxwell-Boltzmann's distribution is assumed for the neural O species inside the bulk plasma then the flux of the O-atom can be related to the neutral O temperature T_O and the mass of oxygen atom M_O through the following expression.

$$K_a = \frac{1}{4} \left(\left[\frac{8k_B T_o}{\pi M_O} \right]^{\frac{1}{2}} / n_o' \right) \quad (46)$$

Similarly the rate constant for the ion driven desorption K_i , is related to the electron temperature T_e , mass of the ion M_i , Bohm velocity u_B and the surface carbon sites density n_o' . Equation (47) describes the relation.

$$K_i = \frac{u_B}{n_o'} = \frac{((k_B T_e)/M_i)^{\frac{1}{2}}}{n_o'} \quad (47)$$

The vertical etch rate given by equation 44, describes a combined effect of both chemical and ion-assisted processes. If the ion-assisted contributions e.g, ion-enhanced desorption and sputtering parts in the equation 44 are equated to zero, the equation modifies to give only the rate of chemical etch process. From section 4.3, we know that pure chemical etching is an isotropic process and thus has the same etch rate for both horizontal and vertical direction. Therefore, with $Y_i K_i$ and $\gamma_i K_i = 0$ we get the following expression for chemical etching:

$$E_H = E_V|_{chemical} = \left[\frac{n_o'}{n_C} \right] \left[\frac{1}{\frac{1}{K_d} + \frac{1}{K_a n_{OS}}} \right] \quad (48)$$

In case of reactive ion etching of a side-wall structures as shown in Figure 4.8, equation 44 describes the vertical etch rate E_V since ion-assisted etching is mainly vertically directed for low pressure processing and equation 48 describes the horizontal etch rate E_H . Often in plasma processing, anisotropy, a_h becomes an important factor and in mathematical terms it is defined as:

$$a_h = \frac{E_V}{E_H} \quad (49)$$

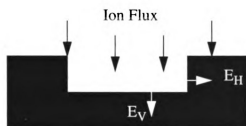


Figure 4.8: Vertical and horizontal etching

It is important to note that under steady state conditions, the horizontal and vertical etch rate and thus the anisotropy are functions of temperature and can widely vary as the temperature of the substrate changes. At low temperature and low pressure processing, e.g. in ECR reactors, the etching is usually extremely anisotropic.

The following chapter utilizes the surface kinetics and the etch rate expression developed in this section for calculating the diamond etch rate in an ECR oxygen plasma.

Chapter V. Etching Experiments and Results

5.1. Variable Identification

Usually development of a process involves a detailed exploration of the experimental parameters with an aim to set them at appropriate values such that an optimum yield of interest is achieved. Because of the large number of combinations of experimental variables, this is not always easy. In our case, a high and uniform etch rate of diamond was defined as the primary yield of interest. We fixed our attention only to the ECR type of reactor with cylindrical discharge, specifically a Wavemat reactor of model 325iTM. Since the reactor geometry plays an important role on the etch rate, the sliding short height was set at the beginning of an experiment and kept unchanged for the duration of the whole run.

With repetitive observation of relatively low diamond etch rates during early pilot experiments, it was realized that a better insight into the major rate-affecting variables was needed. Therefore, the following list of external variables was investigated based on the existing knowledge of plasma and material processing theory.

1. Gas Composition: Use of the right gas composition enhances the plasma chemistry for the etching reactions, hence the etch rate is expected to vary strongly with the gas composition. As described before, an ECR plasma consisting of varying proportions of argon, oxygen and sulfur-hexafluoride was chosen for our purpose. The reason for choosing oxygen is obvious, as diamond is elementally carbon, and one easy way of etching diamond is to oxidize it. However, the choice of SF₆ and argon came more from experience which

will be described later. From the theory of etching, a higher proportion of oxygen in plasma is expected to produce a higher diamond etch rate, hence an oxygen rich environment was chosen for most of the etching experiments.

2. Flow rate of the etching gas and their proportion: For a given gas composition, the total gas flow rate can also be an important variable. For a given pressure, flow rate determines the residence time of the gas molecules inside the main chamber. The average residence time of a gas molecule decreases with high gas feed, as is quantized by the simple relation [5.1] given by $\tau = \frac{pV}{Q}$ where τ , p , V and Q are the residence time, operating pressure, main chamber volume and gas flow rate respectively. Thus the flow rate plays a critical role in determining the probability of the species to react with the work-piece.

Also at low gas feed rates, etch rates often decrease as the area of the substrate increases. This happens due to the lack of adequate etchant species. Hence a minimum amount of flow rate is required to avoid this phenomenon known as the wafer loading effect.

3. RF bias to the substrate: The flux of ions is defined as $\Gamma = n(\vec{r}) \langle v \rangle$ where Γ is the flux, $n(\vec{r})$ is the spatially varying average number density of the species, and $\langle v \rangle$ is the velocity of the species averaged in the velocity space. The independently applied rf bias influences the average velocity, and the kinetic energy of the ionized species incident upon the substrate. The energy of the impinging species is very important to both sputtering effects and reactive ion etching.

4. *Microwave input power:* Microwave power is required to ionize the gas atoms and molecules in order to sustain the generation of ion-electron pairs under steady state conditions. It is easy to imagine following the discussion in section 2.3, that more input power in a discharge would cause more ionization yielding a higher ion density in the bulk plasma and a higher flux of ions to strike the substrate surface. Therefore, the etch rate is expected to increase with the increase of microwave input power.

5. *Down stream substrate distance from the plasma:* Previous work has experimentally shown [5.2] that the sputter rate decreases as the distance between the substrate and the plasma generation region increases. The experimental results agree with the theoretically derived expression for the spatial distribution of species in the downstream region [5.3]. This expression for a cylindrical discharge is given below.

$$n_{e,i}(r, z) = N_0 \left(\frac{2b}{a} \right) \sum_{m=1}^{\infty} \frac{1}{x_{om}} \left[\frac{J_1 \left(\frac{x_{om} b}{a} \right)}{J_1^2(x_{om})} \right] J_0 \left(\frac{x_{om} r}{a} \right) e^{(-k_z z)} \quad (50)$$

In equation (50), $n_{e,i}(r, z)$ represents the electron and ion density at a radial location r and downstream distance z . Here, $z=0$ is taken to be the plane where a constant species concentration of N_0 is maintained. In comparison with the experiments, $z=0$ is taken to be the bottom of the ECR base plate. $r=0$ implies the central axis of the cylindrical cavity.

a and b in the above expression, represent the radius of the downstream chamber and the plasma discharge respectively. J_0 and J_1 are the bessel functions of order zero and one.

x_{om} are the m^{th} zeros of the zero-order bessel function and k_z is given by

$$k_z = \sqrt{\left(\frac{x_{om}}{a}\right)^2 - \left(\frac{\nu_i}{D_a}\right)}. \text{ The terms } \nu_i \text{ and } D_a \text{ are already defined and are known as the}$$

collisional frequency and the diffusion coefficient.

Derivation of equation (50) assumes a spatially uniform species density N_0 at the generation region. Also the species density is taken to be zero at the metallic walls, and the charged particles are assumed to follow the ambipolar diffusion theory. Equation (50) clearly shows that the species density decreases exponentially with the downstream distance. Consequently the etch rate will increase as the downstream distance decreases. However, this must be balanced against the uniformity concerns.

6. Main chamber processing pressure: The processing pressure directly affects the mean free path of the species and the frequency of the species collision. From the $T_e - Cp\Lambda$ curve [5.4], it is known that for a given gas mixture and reactor geometry, lower pressure results in a higher electron temperature, corresponding to a higher ionization rate due to more energetic electrons. On the other hand, a lower pressure corresponds to a reduced number of particles to be ionized. These contradictory contributions to production of ionized species complicate the etch rate dependence on pressure.

In addition, the sheath potential across the rf biased chuck is known to vary with the change of pressure which further complicates the dependence of etch rate on pressure. Besides the etch rate, the etch uniformity is also affected by the processing pressure. At lower pressures, say 1 mtorr, one expects a more uniform plasma environment and a

higher etch uniformity than compared to 20 mtorr. Thus it is apparent that the processing pressure is a vital variable for both etch rate and etch uniformity.

7. Operating mode of the plasma: The operating mode in a microwave reactor determines the patterns of \vec{E} and \vec{B} fields inside the circular metal cavity. These modal patterns influence the spatial distribution of the species and are therefore expected to have effects on etch uniformity. The spatial distribution of patterns for different TE and TM modes and its effects on uniformity are explained in more detail in chapter 6.

5.2. General Discussion on Experimental Design

A typical approach to find the dependence of etch rate on the each variables, is to vary each variable one at a time keeping others fixed at certain values. But this method leads to performing a huge number of experiments. If a set of experiments is designed in which each of our seven variables takes 5 independent values, then the number of necessary runs becomes $5^7 = 78,125$. If each experiment takes two hours to perform and analyze, nearly 1 or more years of round the clock experiments would be required. This unacceptably large number of experiments and experimental hours do not even include the experiments needed to test the repeatability. Obviously this inefficient approach is not useful and needs to be modified. At this point, a tempting compromise would be to maximize etch rate for only one variable keeping others constant. Then fixing this variable at that value, other variables are investigated for their corresponding maxima. The process continues until all the variables are maximized. Though this method results in a reasonably lower number of experiments to perform, at times the method can fail miserably. The example illustrated in

Figure 5.1 shows that the success of this method totally depends on the nature of the response surface. Referring to the hypothetical response curve shown in Figure 5.1, it can be seen that while a single-variable-at-a-time optimization could lead to an apparent maximum of $\sim 6 \mu\text{m/hr}$ the actual maximum of etch rate of about $15 \mu\text{m/hr}$ exists under a different set of parameter values. The experimentalist would need to be lucky to reach this correct global maximum with the technique described. However, various methodical design approaches address this problem and are available in statistics books [5.5, 5.6, 5.7]. Statistically designed experiments help to evaluate the etch performances based on relatively fewer experiments. Some of these commonly adopted design structures are listed below.

1. *One-way treatment structure*: Often in statistical language, the treatments refer to effects over which the experimenter has full control such as, the power, bias etc. in our case. The one-way treatment structure consists of a set of treatments where no relationship between the treatments is assumed and each treatment is analyzed independently. This is essentially a one-variable-at-a time technique, described before.

2. *Factorial arrangement treatment structure*: A full factorial arrangement of treatments structure consists of the set of treatment combinations constructed by combining two or more levels of treatments. This is a very general way of constructing the experimental design. If there are n treatments or variables to be analyzed with each having s different levels then s^n becomes the total number of combined experiments. A special case of factorial arrangement is the two-way treatment structure consists of the set of treatments constructed by the levels of two different types of treatments. In general, if the first treatment type has s levels and the second treatment has r levels then they produce sr treatment

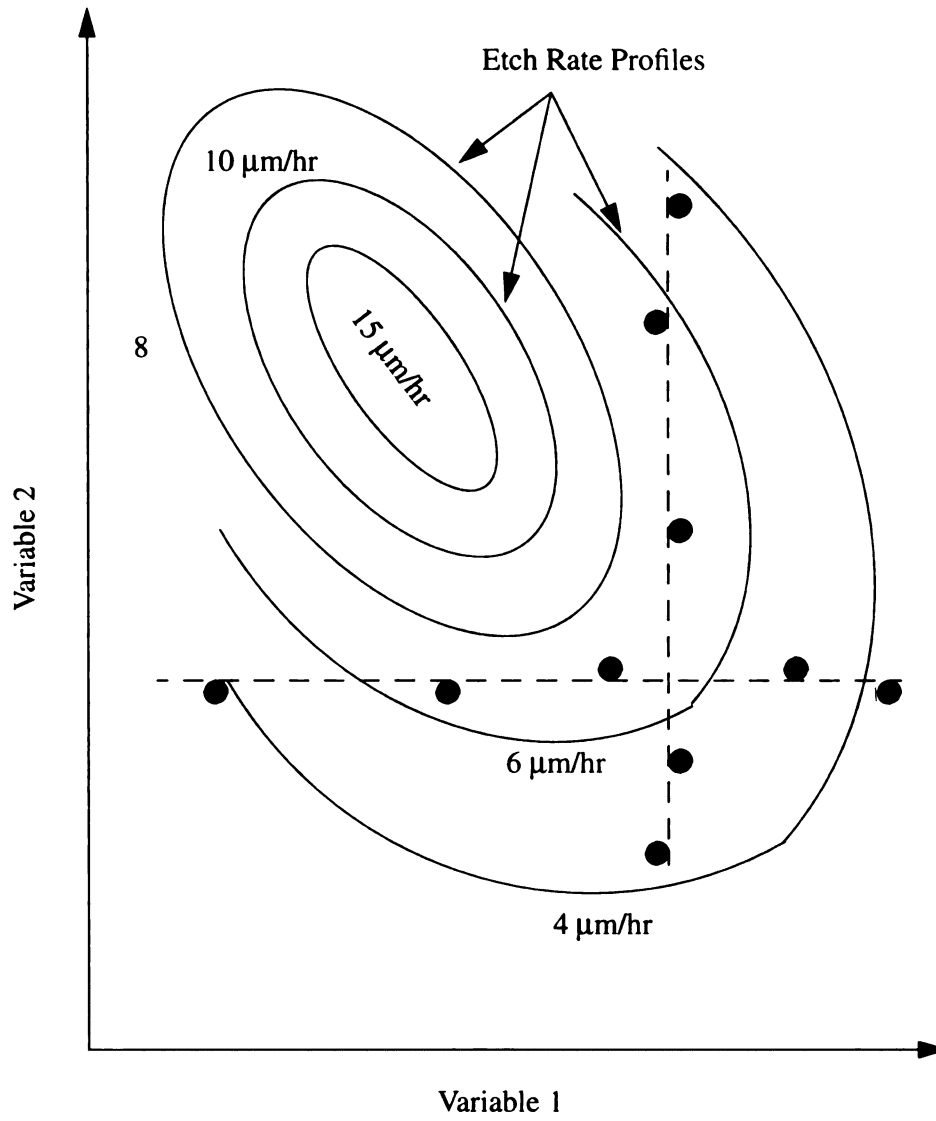


Figure 5.1: One at-a time experimental approach

combinations. As previously noted this approach can lead to a very large number of experiments.

3. *Fractional factorial arrangement treatment structure*: A fractional factorial arrangement treatment structure consists of only a part or fraction of the possible treatment combinations in a full factorial treatment structure, described before. There are many techniques for selecting an appropriate fraction, most of which depend on the assumptions the experimenter makes about the interactions between the various types of treatments in the treatment structure.

Recently, statistical designs of experiments, especially fractional factorial designs have been largely used in the area of plasma etching [5.8, 5.9]. This approach commonly begins with two distinct levels of treatments about a center point, one higher and one lower value for each treatment. The purpose of the initial experiments is to determine the slope of the response curve. In the case of n variables, the number of the experiments suggested by the full factorial design is 2^n . Often the number of treatments in a plasma processing is large e.g, $n = 5$ or 6 , and the number of initial experiments suggested by the full factorial design becomes unaffordable so a fraction of the experiments are usually eliminated using appropriate statistical elimination formats.

During simultaneous variation of different factors, the level of response changes because of main treatment effects and different combination of treatment interactions. Mathematically, the difference between the average responses at the two levels of a factor is defined as the main effects. Interaction effects result from the presence of joint factor effects. When the nature of response change with one factor depends on the levels of other factors, then the interaction is said to exist between the prime factor and the other factors.

h
b
h
re
e
w
th
m
fo
th
th
co
m
w
m
to
Tr
th
e
m
88

Interactions between two factors are called two-factor interaction effects, interactions between three factors are called three-factor interaction effects and so on. Mathematically, half the difference between the main effects of one factor at the two levels of a second factor is known as the two-factor interaction effects.

Interaction effects are not necessarily present between two given factors. Also the experimentalist may not be interested in knowing about all interaction effects. Therefore, while designing the fractional factorial design, the experimentalist can choose to confound the unimportant effects in order to reduce the total number of experiments. Resolution formats e.g, resolution III, IV, V etc. are different standard formats that can be used to confound different effects and eliminate half or more number of the experiments. With half of the experiments eliminated from the full factorial design, a resolution III design ensures that main-effects are not confounded with other main-effects but some main-effects may confound with two-factor interaction effects. A resolution IV does not confound one main-effect with other main-effects or two-factor interaction effects but does confound two-factor interaction effects with other two-factor interaction effects. Similarly, a resolution V does not confound main effects and two-factor interaction effects with each other, but does confound two factor interactions with three-factor interaction effects and so on. The details of design aspects of experiments and use of different formats may be found from [5.10].

However, once the initial experiments are performed following the design, the results are linearly regressed to find a best linear fit for the output function which is to be optimized; etch rate for our case. Common computer packages for statistical analysis such as, SPSS [5.11] may be used for the purpose of regression [5.12]. The coefficient of each of

the variables in the obtained linear equation determines the weight of that variable for the output function. These response surfaces are plotted using the linear equation and the direction of steepest ascent is chosen as the direction to further vary the variables to determine a new center point. This way the improvement of the result is continued at each iteration till the global maxima of the function is reached.

The repeated use of fractional factorial design technique with two levels of treatments about a center point to determine the direction of the steepest ascent in order to optimize an yield is often referred to as response surface methodology (RSM). This method suggests a total of 2^{n-1} initial experiments to perform, where n implies the number of variables to be investigated. With this method, half the number of experiments suggested by the full factorial designs are eliminated.

5.3 Process of Optimizing the Diamond Etch Rate

The general response surface method was applied to our specific problem of maximizing the plasma etching rate for diamond while avoiding the non-uniformity of etching and other undesirable effects. In the very beginning of this study, microwave input power, rf bias to the substrate, and gas composition as determined by individual flow rate were thought to be the most important variables and the rest were kept constant. A full factorial experiment to determine all effects would require 2^4 or 16 experimental runs. In order to reduce the number of runs, a 2^{4-1} fractional design was used, requiring only 8 experiments to be identified from the initial design of 16 experiments. This elimination based on resolution IV formats, guaranteed no confounding between the main effects with other main effects or two-factor interaction effects. However, at this point, we were simply interested

in the main effects.

In addition to these 8 experiments the center point experiment was run thrice to learn about the standard error of the process. The order of the experiments was randomized to avoid hidden time effects. For all these experiments, the factors were varied between a high value and low value which are shown in Table 5.1.

Table 5.1: Ranges of the variables for the initial design

Factor	Center Value	Higher Value	Lower value
Power	650	700	600
Bias	94	102	85
O ₂	4	6	2
SF ₆	4	6	2

All these etching experiments were performed on a 50 mm diameter semi-transparent diamond sample NTA1-005. This sample was initially 250 micron thick and 1.2518 grams in weight and was cut out of a 100 mm diamond wafer. Our aim was to precisely and uniformly etch 25 microns from the 50 mm diameter diamond wafer at a reasonably high rate.

Each etching operation was 1 hour in length, with the main chamber process pressure maintained at 7 mtorr, the Argon gas flow fixed at 12 sccm, and the downstream distance at 11 cm. The etching thus obtained during the time period of March-April 1994 is presented in the Table 5.2. Here the average etch rate was determined by weighing the sample before and after the etching.

From the output of the statistical software SPSS/PC+ described in Appendix B, the dominance of the chosen variables on the etch rate over the random error can be recognized. The value of signif F identifies the significance of the factors considered for the

analysis. For our case, the SPSS output shows the value of (1-signif F) is almost 1, which implies that bias, oxygen flow rate, microwave power and SF₆ flow rate in combination showed have a significant effect (~100%) on etch rate over the uncontrolled random experimental error. Thus we conclude that our initial choice of variables was appropriate.

Table 5.2: The first design of experiments

Run #	Order	Power	Bias	O ₂	SF ₆	μm/hr
1	5	600	85	2	2	1.36
2	8	700	102	2	2	1.98
3	4	600	102	2	6	1.68
4	7	700	85	2	6	1.27
5	9	600	102	6	2	2.42
6	2	700	85	6	2	2.02
7	1	600	85	6	6	1.58
8	11	700	102	6	6	2.19
9	3	650	94	4	4	1.92
10	6	650	94	4	4	1.69
11	10	650	94	4	4	1.88

The analysis of variance (ANOVA) performed with SPSS was found helpful in identifying the significance of individual variable on the etch rate. This effects of individual factors are ranked in the descending order of influence in Table 5.3 which shows that the effect of the first three variables, bias, oxygen flow rate, microwave power was positive on the etch rate whereas the effect of the SF₆ was negative.

From the linear multiple regression of the data reported in Table 5.2 the following equation of etch rate was generated.

$$\text{Etch Rate} = 0.0338(\text{bias}) + 0.139(\text{O}_2) + 0.00198(\text{power}) - 0.0651(\text{SF}_6) - 2.94$$

In the above equation, etch rate, flow rates, power, and bias are expressed in micrometer/hr, sccm, watts, and volts respectively. MATLAB software was used to plot different constant etch rates with oxygen flow rate and SF₆ flow rate as the two axes. These plots, shown in Figure 5.2, assume 650 watts of microwave power and 2 sccm of SF₆ flow rate.

Table 5.3: Effect of variables on etch rate

Variable	Effect
Bias	positive
Oxygen	positive
Power	positive
SF ₆	negative

The direction of steepest ascent suggests moving towards a higher rf bias. However, the maximum value of the bias for the present configuration of the plasma reactor in the constant bias mode is a set point of 150 V, which induces around 120 V dc bias during etch experiments. Hence it was clearly understood that for obtaining higher etch rate of diamond we cannot follow the steepest ascent indefinitely. To obtain higher etch rate for a dc bias of ~ 120 V, the oxygen flow rate has to be increased. Figure 5.2 shows that for achieving higher etch rate, say 4 μm/hr or above, the oxygen flow rate has to be greater than about 12 sccm. Hence from this analysis, increasing the rate of oxygen flow was identified as an important step for increasing the etch rate.

However, the flow rate of SF₆ and its combined effect with O₂ on etch rate was thought to be equally important to analyze at this point. A next set of new experiments were designed involving O₂ and SF₆ gas flow rates about a center point.

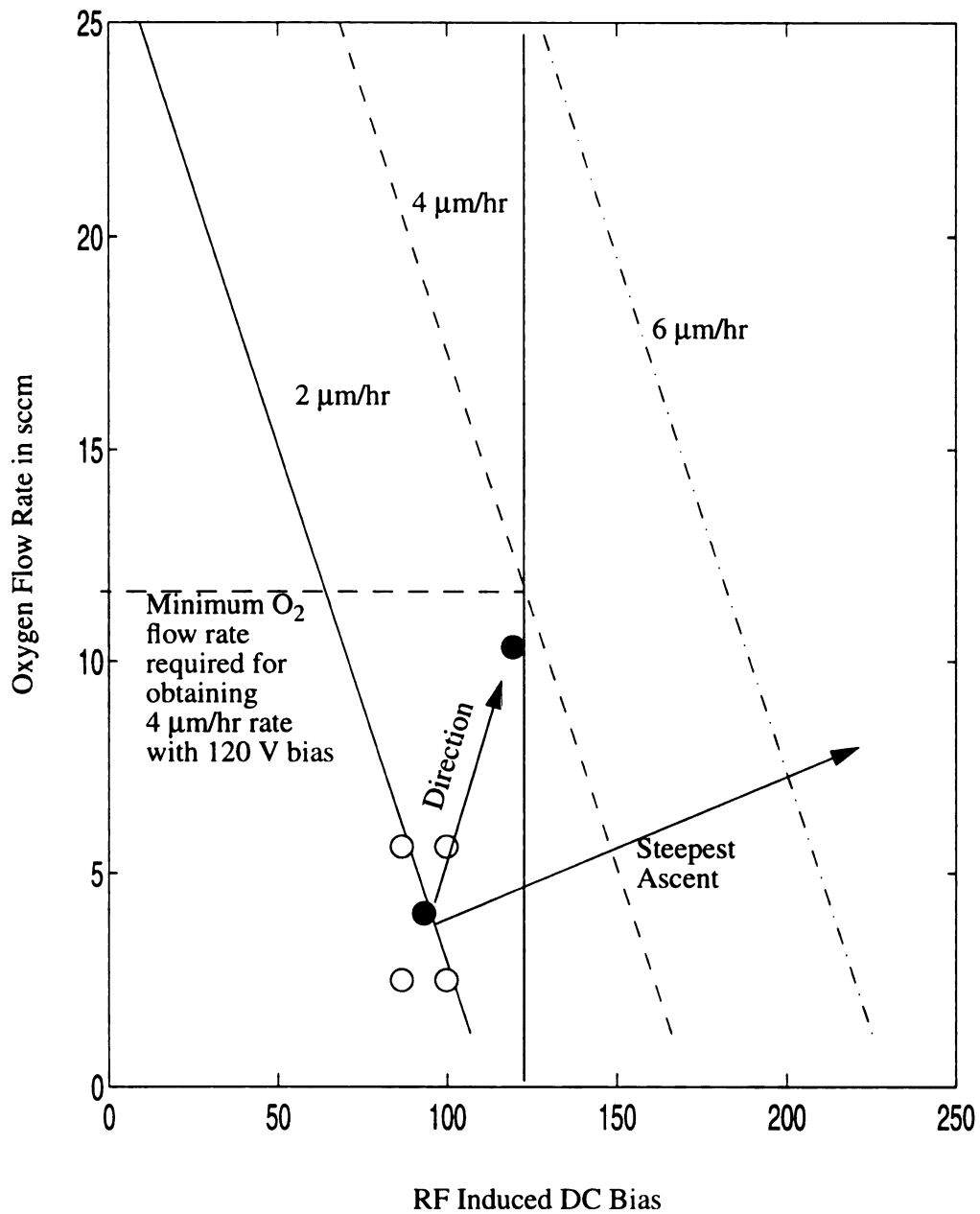


Figure 5.2: Results of regression analysis

During these experiments, oxygen flow rate was increased to 10 sccm from the 6 sccm in order to verify the prediction of increased rate with increased oxygen flow. Table 5.4 shows the new values chosen for the center point, lower and upper bound for the gas flow rates. While performing the experiments, microwave power was fixed at 600 W, the rf induced bias was recorded as ~120 V, the downstream distance was held at 11 cm and the pressure was set to 7 mtorr.

Table 5.4: The choice of gas flow rates

Factor	Center Value	Higher Value	Lower value
O ₂	8	10	6
SF ₆	2	3	1

These experiments were performed in April-May, 1994 and the results are shown in the Table 5.5.

Table 5.5: Exploring the gas effects on the etch rate

Run #	Order	O ₂	SF ₆	μm/hr
1	6	6	1	4.0
2	3	6	3	3.0
3	2	10	1	4.7
4	4	10	3	3.5
5	1	8	2	3.7
6	5	8	2	4.1

For these experiments, the microwave power, the rf induced dc bias and the processing pressure were fixed at 600 watt, 122 volt, and 7 mtorr respectively. The downstream distance was held at 11 cm and the argon flow rate was maintained at 12 sccm. The multiple

regression analysis on the above data yields an expression which is described as:

$$\text{Etch Rate} = 0.155(\text{O}_2) - 0.54 (\text{SF}_6) + 3.68.$$

Constant etch rate surfaces e.g, 4, 6, 8 $\mu\text{m/hr}$ were plotted on an SF_6 -oxygen axis using this linear equation. This plot is shown in Figure 5.3. The direction of steepest ascent is easy to determine from plots and the plots suggest to move in the direction of as small SF_6 percentage as possible. But a separate problem crops up if this ratio of oxygen to SF_6 is continually increased. A black film starts forming when this ratio exceeds a certain value (about 14:1) which appears to be slightly dependent on the diamond sample and perhaps on the diamond quality. Hence finally a direction of 10% SF_6 was chosen in order to increase the etch rate without forming the black film. The new value of O_2 and SF_6 flow rates became 20 and 2 sccm.

At this point it was felt the variables that were initially neglected needed more attention. The pressure was varied between 3 and 10 mtorr which gave the etch rates shown in Table 5.6. It should be noted that the maximum etch rate occurs at about 4 mtorr. To confirm this observation, a set of 10 experiments involving pressure as one of the variables were further designed on a fresh sample NTA1-011.

Table 5.6: Investigating the pressure effects

Run #	Pressure	$\mu\text{m/hr}$
1	7	4.56
2	4	5.78
3	10	4.15
4	3	5.16
5	4	5.86

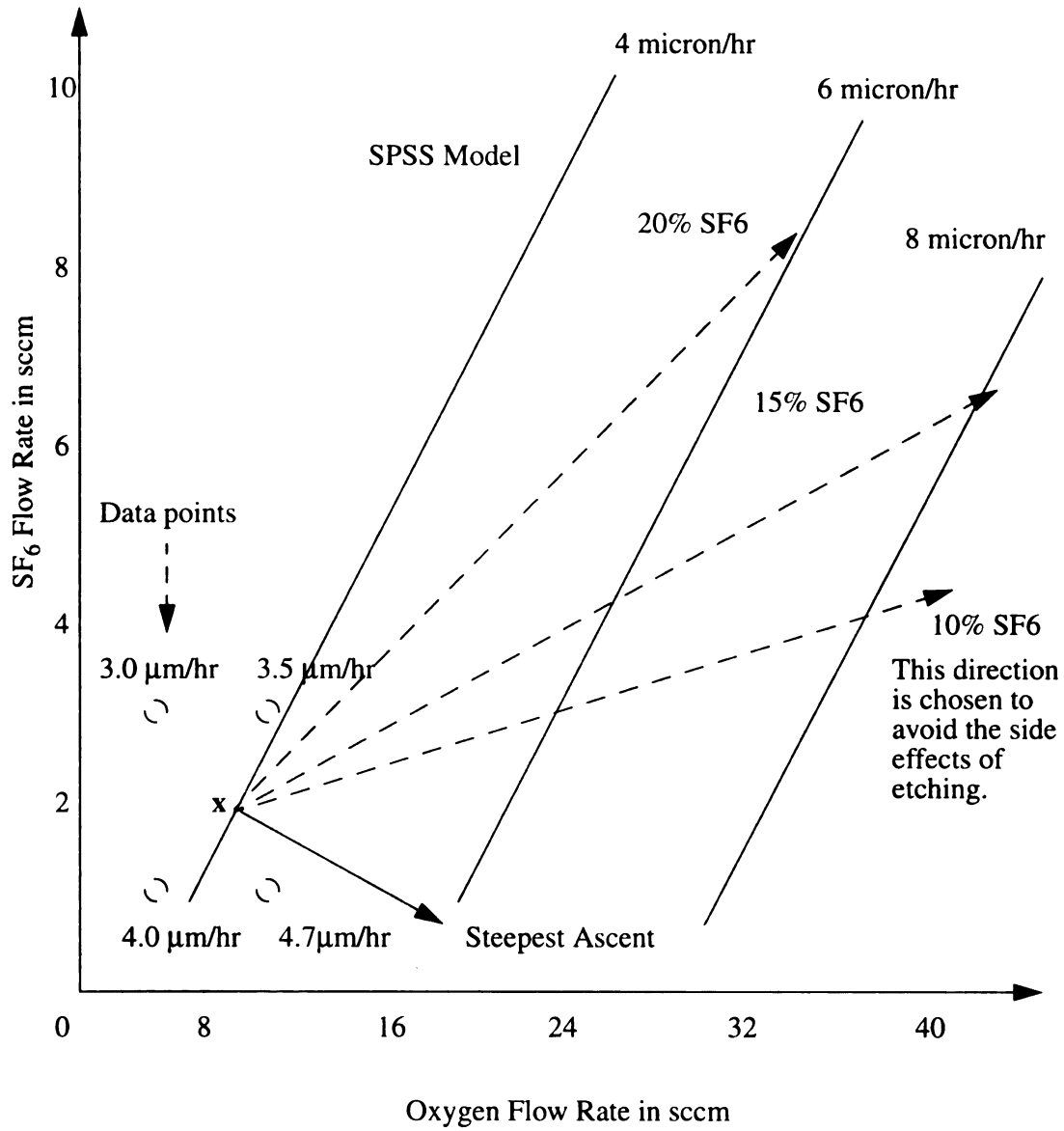


Figure 5.3: The direction of steepest ascent

This sample weighing 1.5988 g was very similar in appearance to NTA1-005 and had thickness ranging from 360 to 440 microns. It was also cut from a 100 mm diamond sample. The experiments confirmed the existence of a maximum at 4 mtorr. From these preliminary experiments, four of the major variables, bias, O₂ flow rate, SF₆ flow rate, and pressure were optimized and fixed at 120 V, 20 sccm, 2 sccm and 4 mtorr respectively. With the help of the statistical design of experiments we reached an etch rate close to 6 μm/hr from an initial low etch rate of 1 μm/hr or less.

With repeatable etch rate results and satisfactory uniformity on 50 mm wafers, 100 mm diameter samples were considered for etching. The first 100 mm sample etched was NTA1-60 which had a thickness of 1.29 mm and a weight of 35.69 g. It was blackish in appearance. In the beginning, 10 runs shown in Table 5.7, were conducted to remove 50 micrometer from the substrate side. For all runs except Run 9, the substrate height was 12 cm downstream from the plasma, the O₂ flow rate was at fixed 20 sccm and SF₆ at 2 sccm. For Run 9, the gas flow rates were doubled. The aim of these experiments was to investigate the combined effect of argon and power on the etch rate. These experiments were not center point experiments. The microwave power was varied at two levels of argon flow rate. Doubling the gas flow rates did not affect the etch rate much which indicated that the etch rate does not depend on the flow rates of the individual gas as long as the mutual ratios among the feed gas are unchanged. This experiment also confirmed that the initial gas settings did not suffer from any wafer loading effect. From the results presented in Table 5.7, no clear combined effect of argon and power on etch rate was identified. Hence a next set of 7 experiments were planned for etching 50 microns at a fixed microwave power level but with two levels of argon.

Table 5.7: Investigating the combined effect of power and argon

Run #	Power	Ar	Run time	$\mu\text{m/hr}$
1	650	18	2	3.96
2	650	12	2	5.42
3	700	18	2	3.83
4	750	12	2	4.36
5	750	18	2	4.31
6	600	18	2	4.15
7	600	12	2	4.00
8	700	12	2	5.08
9	650	24	2	4.82
10	650	12	2	4.85

The experiments shown in Table 5.8 were also intended to test the repeatability of etching runs under similar parameter conditions. This time the attention was focussed on etching the growth side of the sample mainly to know the etching behavior of the growth side. During the etching runs, relevant parameters such as pressure, rf bias, O_2 and SF_6

Table 5.8: Experimental design for understanding the effect of argon

Run #	Power	Ar	Run time	$\mu\text{m/hr}$
1	650	12	2	4.52
2	650	12	1	4.31
3	650	12	1	4.23
4	650	12	2	4.52
5	650	18	2	4.17
6	650	18	2	4.21
7	650	18	1.5	4.40

were kept at their optimized values of 4 mtorr, 150 volts, 20 sccm and 2 sccm respectively.

It can be seen from the results of these experiments that the effect of argon on the etch rate was found insignificant over the range investigated. However, the etch repeatability on the same sample under the same plasma parameters was found to be very satisfactory. Improvements in post-etched uniformity of the samples thickness was observed. The peripheral sides of the samples became rougher after etching.

At this point it was decided to further remove 100 microns from the growth sides with an intention of varying the operating modes. This was one of the variables left untouched. In our reactor the modes are difficult to identify with certainty because the diameter of MPDR 325i is relatively large [5.4]. For this large diameter cavity, some of the existing modes may be degenerate or overlapped. However, for our experiments, the height of the sliding short and therefore the height of the cavity was taken as the variable. For every unique resonant position of the sliding short, an unique modal pattern is generated, may it be single, multiple or degenerate.

Initially three different cavity heights corresponding to sliding short positions 236.54, 225.00 and 248.08 mms were chosen. Table 5.9 shows the details of the design of experiments and their corresponding results. Although the results do not apparently show any significant influence of the modes on the etch rate, an intriguing result was obtained from the analysis of etch uniformity. Processing with one mode (236.54) yielded a standard deviation of about 18% (8 μm standard deviation around an average of 45 μm) which is reduced to 5% (5 μm standard deviation around an average of 103 μm) with all three modes shown in Table 5.9. Since the total amount of etching was limited and specified by the Norton Diamond Film, more investigations on uniformity with individual modes were

not possible on the same sample.

Table 5.9: Variation of the operating mode and the power

Run #	Microwave Power	Sliding Short position (mm)	Run time	$\mu\text{m/hr}$
1	650	236.54	2	5.04
2	600	236.54	2	4.74
3	600	225.00	2	3.59
4	700	225.00	2	5.12
5	600	248.08	2	4.45
6	700	248.08	2	4.84
7	650	236.54	2	4.89
8	650	236.54	2	4.82
9	600	248.08	2	4.53
10	600	225.00	2	3.49
11	700	236.54	2	3.24

Therefore, experiments continued on other samples to identify the overall uniformity of etching on a 100 mm wafer with different modes and their associated etching patterns. After quite a lot of effort we failed to recognize any statistically significant and unique spatial etching pattern for any individual mode. However typical uniformity data as collected from measuring 21 points on a 100 mm wafer are presented in Table 5.10. These points were varied radially and angularly on the surface. All the thickness measurements on different 100 mm diameter wafers were obtained from Dr. Paul Goldman, previously at Norton Diamond Film. The measurements were taken using a Mitutoyo 389 deep-throat micrometer and the measurements were repeatable only within an error bar of 10 μm .

Table 5.10: Uniformity analysis

Sample	Dates	Modes	Uniformity μm	%
NTA1-60	07/06/94 - 07/09/94	236.54	45 ± 8	18%
NTA1-63	08/29/94 - 08/30/94	248.08	49 ± 17	35%
TA-1484	09/01/94 - 09/02/94	225.00	59 ± 7	12%

Table 5.10 shows that the standard deviation of etching was 18%, 35%, and 12% of the mean value for modes corresponding to 236.54, 248.08, and 225.00 mm of cavity height. The standard deviation, implying the non-uniformity of etching, in the case of mixed modes experiments was reduced to 5% of the mean value which suggests that the etch uniformity can be improved with an appropriate combination of different resonant modes. But this hypothesis was not proved statistically because the error associated with the micrometer measurements was comparable with the uniformity improvement claimed. Therefore, we decided to further investigate the mixing modes phenomenon from the theory and simulation of the species distribution in the downstream distance. This has been discussed in detail in chapter 6.

In the meantime, etching experiments were continued in the context of improving etch rate and with 1.1 kW of microwave power and flow rate ratio of oxygen to SF_6 (28:2), finally an etch rate of around $7 \mu\text{m/hr}$ on 100 mm diameter wafers, and $\sim 12 \mu\text{m/hr}$ for 2 cm X 2 cm wafers were obtained. At this point, the bell jar showed a crack which we think may have resulted from the high microwave power.

When the system was fully repaired, it was modified to a great extent. The rf biased chuck was rebuilt, a new bell jar was put in and the water cooling of the rf chuck was

changed to a closed loop cooling system with a chiller circulating a mixture of ethylene glycol and de-ionized water which has a much higher electrical impedance. The results obtained from the modified system set up are reported separately in this work.

The focus of the experimental research at this point was shifted from obtaining a further high diamond etch rate to investigate effects of individual variables on etch rate. The results of these investigations along with some more interesting observations are reported in the next section.

5.4 Effect of Variables on Etch Rate

During performing the statistically designed experiments, we observed that oxygen, argon, SF₆ ECR plasmas can etch diamond from both the substrate and growth side, and that the etch rate is not significantly different from one side to the other under the same plasma conditions. However, the etch rate does vary from one sample to the other under the same plasma processing conditions. The reason for this observation is not yet clear but to avoid the possibility of introducing errors due to some unknown reasons that attribute to the property of an individual CVD diamond sample, in this section the etch rate obtained from etching two different samples are not combined for studying the effects of individual parameters on etch rate.

Most of the previous etching work following the factorial design concepts involved experimental designs with simultaneous variation of multiple variables. Hence conclusions about the effect of one independent variable on the etch rate was difficult to draw from these results. A fresh set of experiments was therefore designed and performed to document single variable dependence. In most cases, every experiment was performed

twice to check the repeatability. The repeatability of the etch rate for polycrystalline diamond films in our system was found very satisfactory. The standard deviation is almost always calculated to be less than 10% of the mean etch rate, and typically 3-4%.

5.4.1 Effect of RF Bias and RF Power on Etch Rate

From the result of statistical analysis, rf bias was concluded to be the most dominating factor in determining the etch rate of diamond. To explore this further, three samples, TF 271, TF 254 A, and TF 267 were simultaneously etched with the rf power varied between 0 W and 235 W. The variation of the rf power in that range resulted in a variation of induced negative dc substrate biasing from 0 V to 138 V for argon-oxygen-SF₆ plasma. Out of the three samples etched, TF 271 was a 92 mm diameter semi-transparent sample with a beginning weight of 12.9346 gram; the other two samples, TF 254 A and TF 267 were 1 cm diameter semi-transparent samples with initial weights of 0.1759g and 0.0445 g respectively.

For the experiments to study the effect of the rf induced dc bias on diamond etch rate an argon, oxygen, SF₆ plasma with flow rates of 6, 28, and 2 sccm at 4 mtorr processing pressure was used. The actual absorbed microwave power was about 400 W and the mode was fixed corresponding to 248.08 mm of sliding short height. The runs were 1.5 hours long and during processing, the wafer was placed at 5.5 cm downstream distance from the baseplate position. Table 5.11 summarizes the results obtained from these experiments. At the end of 16 runs used for studying the effect of bias on etch rate, a total of 73.8 μm, 84.2 μm and 85.6 μm were removed from TF 271, TF 254 A and TF 267 respectively.

Careful study of the experimental results in Table 5.11 shows that at higher values of

dc bias ($> 120\text{V}$), significant increase in rf power leads only to a very little increase in rf induced negative dc voltage.

Table 5.11: Etch rate vs. rf bias: investigating the nature of dependence

RF Power (Watts)	Induced DC Bias	$\mu\text{m/hr}$ TF 271	$\mu\text{m/hr}$ TF 254A	$\mu\text{m/hr}$ TF 267
230	-138	6.94 ± 0.12	7.48 ± 0.99	7.67 ± 0.16
198	-136	6.38 ± 0.05	6.19 ± 0.16	6.73 ± 0.16
150	-134	5.55 ± 0.17	6.19 ± 0.16	6.37 ± 0.66
95	-125	3.04 ± 0.15	4.21 ± 0.33	3.54 ± 0.66
45	-86	1.26 ± 0.09	1.75 ± 0.165	2.00 ± 0.16
25	-42	1.01 ± 0.08	1.65 ± 0.00	1.77 ± 0.167
17	-23	0.52 ± 0.02	0.590 ± 0.16	0.70 ± 0.035
0	0	0.074 ± 0.01	0	0

In practice, matching the rf power to the substrate at a given dc bias requires a two-fold adjustment. The first part is associated with controlling the amplitude of the 13.56 MHz rf sinusoidal signal in such a way that a specified dc bias appears at the substrate and the second part is concerned with matching the dynamic plasma load to the 50Ω impedance of the rf generator for minimizing reflected power and maximizing the rf power flow to the substrate. The amplitude of the rf voltage is adjusted through computer control and matching of the generator impedance to the plasma is achieved using a matching network which can either be manually operated or computer controlled. As seen from Table 5.11, the relationship between the dc bias and the corresponding rf power is clearly non-linear.

To understand this better, let us follow the analysis given by Lieberman [5.13] and

consider a discharge modeled as a load impedance $Z_D = R_D + jX_D$ where R_D and X_D are the discharge resistance and reactances respectively. The rf power source connected to Z_D is modeled by its Thevenin's equivalent circuit, consisting of a voltage source with complex amplitude V_T in series with a source resistance R_T . The time average power flowing into the discharge is: $P_{RF} = \frac{1}{2} \text{Re}(V_{RF} I_{RF}^*)$, where V_{RF} is the complex voltage across Z_D , and I_{RF} is the complex conjugate of the complex current flowing through the series circuit. Solving for V_{RF} and I_{RF} from the series elements we get $I_{RF} = \frac{V_T}{R_T + R_D + jX_D}$ and $V_{RF} = I_{RF}(R_D + jX_D)$. Therefore we can express the rf power flow through the discharge as:

$$P_{RF} = \frac{1}{2} |V_T|^2 \frac{R_D}{(R_T + R_D)^2 + X_D^2} \quad (51)$$

Under a perfect impedance matching which is assumed to be achieved with the matching network, the reactance part of the equation (51) becomes zero and R_T equals to R_D .

For a lossless matching network, we get $|V_T| = \frac{(R_D R_T)^{1/2}}{X_D} V_{RF}$ from Lieberman [5.13].

Therefore, in a matched condition the maximum rf power flow to the discharge becomes:

$$P_{RF}|_{max} = \frac{1}{2} \frac{|V_T|^2}{R_T} = \frac{1}{2} \left(\frac{R_D}{X_D^2} \right) V_{RF}^2 \quad (52)$$

Equation (53) describes a parabolic dependence between the rf power flow and the rf voltage if R_D and X_D are assumed to be constant.

A relation between the amplitude of rf voltage, V_{RF} and the induced dc bias, V_{dc} can

be obtained from the following expression [5.14].

$$V_{dc} = V_f - V_{RF} + \frac{k_B T_e}{2e} \ln\left(\frac{2\pi e V_{RF}}{k_B T_e}\right) \quad (53)$$

Equation (53) is valid for $eV_{RF} \gg k_B T_e$, which is usually true for rf substrate biasing. In equation (53) k_B is the Boltzmann's constant, T_e is the electron temperature, and V_f is the floating potential. V_f can be calculated relative to the plasma potential V_p from the following expression [5.14].

$$V_p = V_f + \frac{k_B T_e}{2e} \ln\left(\frac{M_i}{2\pi m_e}\right) \quad (54)$$

In equation (52) M_i and m_e are the mass of the ions and mass of electrons respectively. If T_e is assumed to be 6 eV for our reactor, then for oxygen plasma $V_p - V_f$ becomes ~ 28 V.

Although equation (53) suggests a non-linear relationship between V_{RF} and V_{dc} , the part $\frac{k_B T_e}{2e} \ln\left(\frac{2\pi e V_{RF}}{k_B T_e}\right)$ in equation (53) is relatively small for the range of V_{RF} we are interested in. Therefore, for all our purposes, $|V_{dc}|$ is slightly less than the peak voltage V_{RF} and proportional to it. Hence, equation (52) can now be rewritten as equation (55) which indicates a non-linear parabolic relationship between rf power and induced dc voltage.

$$P_{RF}|_{max} \propto V_{dc}^2 \quad (55)$$

It is important to note that for the derivation of the above relation, R_D and X_D are assumed to be constant under all rf power levels but in reality, this assumption does not hold true.

To further document the relation between the rf power and the dc bias in an microwave

reactor, an interesting experiment was conducted. An argon-oxygen-SF₆ plasma was generated with only rf power input in the absence of microwave power, and the rf induced dc bias was measured as the rf input power was varied. In a similar experiment rf induced dc bias was measured at the same values of rf input power but in the presence of 500 watts of microwave input power. The rf power vs. measured induced dc bias with no microwave power and with 500 watts of microwave power are plotted in Figure 5.4. The shape of the curves showing the dependence of dc bias on rf power looked similar in both cases, but the with-microwave curve is shifted lower by about 50 V. The non-linear dependence of rf power on the dc bias is not the simple square relation of equation (55). This may be in part because the discharge impedance decreases as the level of rf power flow increases. Such a decrease would be due to the local generation of species around the rf biased substrate which is effectively decreases R_D as the rf power increases. Note that for the higher density with microwaves, a given rf power creates less dc voltage than with rf only.

With this understanding of rf power flow and the induced dc bias, we turn our attention to study their effect on etch rate. From Table 5.11, it can be seen that the for the same applied rf bias or power, the etch rate varies from sample to sample, although a similar nature of etch rate dependencies with both rf power and dc bias were shown by all three samples. The data of etch rate vs. dc bias and etch rate vs. rf power for TF 271 were picked for plotting in Figure 5.5 and 5.6. This sample was chosen particularly because the measurements of weight difference for the larger diameter and heavier sample TF 271 are more accurate. The solid line of the Figure 5.6 represents the best cubic fit to the experimental data. Analysis of the Figure 5.5 and 5.6 shows that diamond etch rate improves with both rf power and induced dc bias which means that higher ion energy or higher ion

flux or both can increase the etch rate. This is expected because higher ion energy increases the ion-energy driven desorption of C:O bonds from a location on the carbon surface and an increased ion flux on the surface increases the rate of incident ions and yields a faster etch rate.

Although Figure 5.5 and 5.6 are very useful to know the behavior of etch rate with dc bias or the rf power, these plots are not adequate to understand the dependence of etch rate on only ion energy. As mentioned before, the rf power level influences the discharge impedance, so the increase in etch rate may be due to both increased energy of the species and increased number of species. To account for the effect of increased species density around the substrate, a normalized etch rate is considered for plotting. Since the actual ion flux is not measured, the normalization is done by dividing the etch rate with a quantity proportional to the ion flux. The ratio of rf power to induced dc voltage is proportional to the ion flux, hence the effect of increased species density can be eliminated when the etch rate is divided by this quantity. Figure 5.7 shows the normalized etch rate for different values of rf induced dc bias. The plot approximately supports a linear dependence of etch rate with the ion energy. The distinction between the ion-energy driven etching processes namely, the sputtering and RIE, is not possible until the sputtering results are discussed later in this dissertation: at this point however, note that the linear dependence of etch rate on ion energy agrees with a key assumption made in section 4.4 while deriving the theory for reactive ion etching of diamond. This assumption described that the etch rate of diamond in a pure oxygen plasma is mainly limited by the desorption rate of C:O and not by the arrival rate of the flux of O atoms, therefore the etch rate linearly increases with the

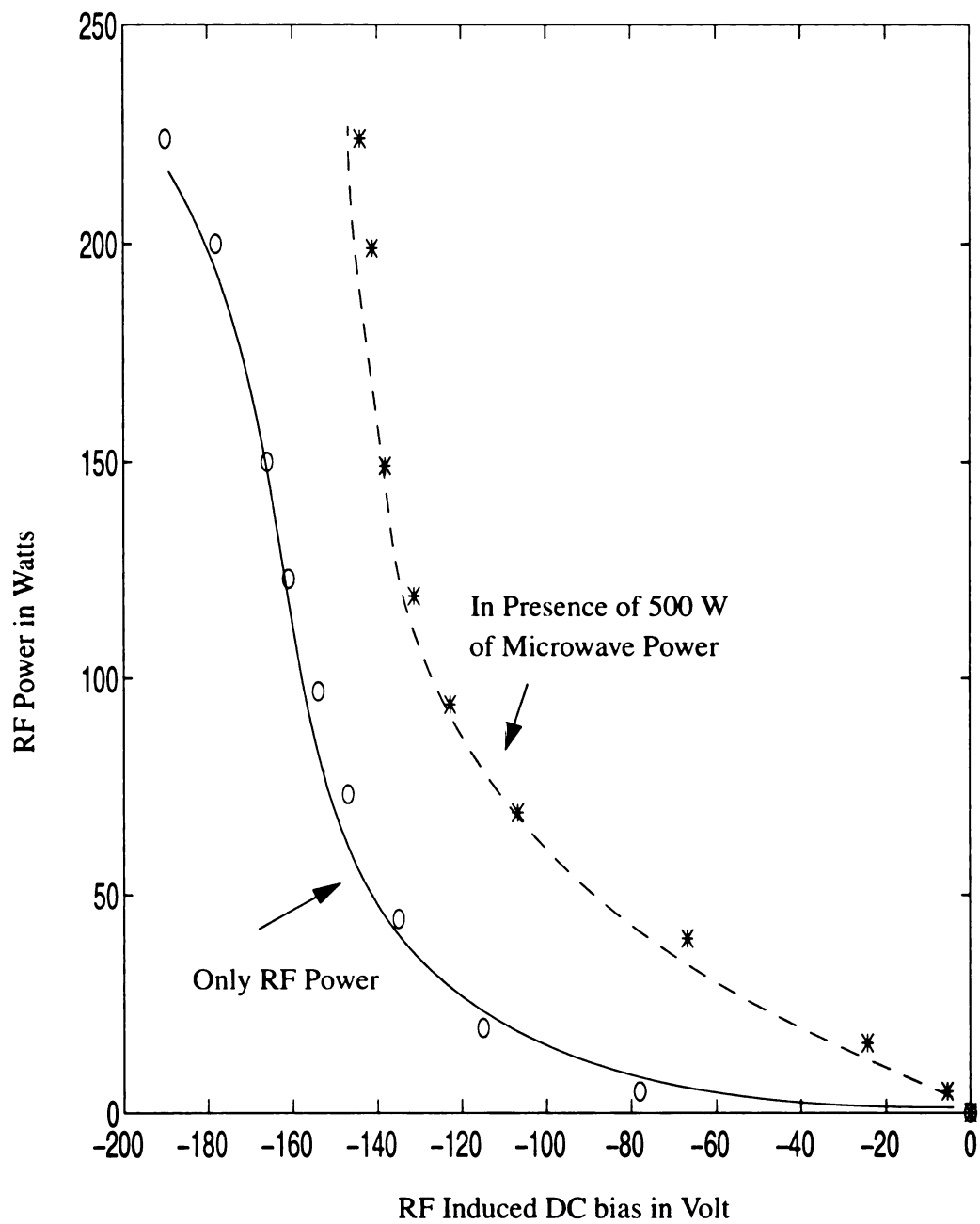


Figure 5.4: Role of microwave power in rf induced dc bias

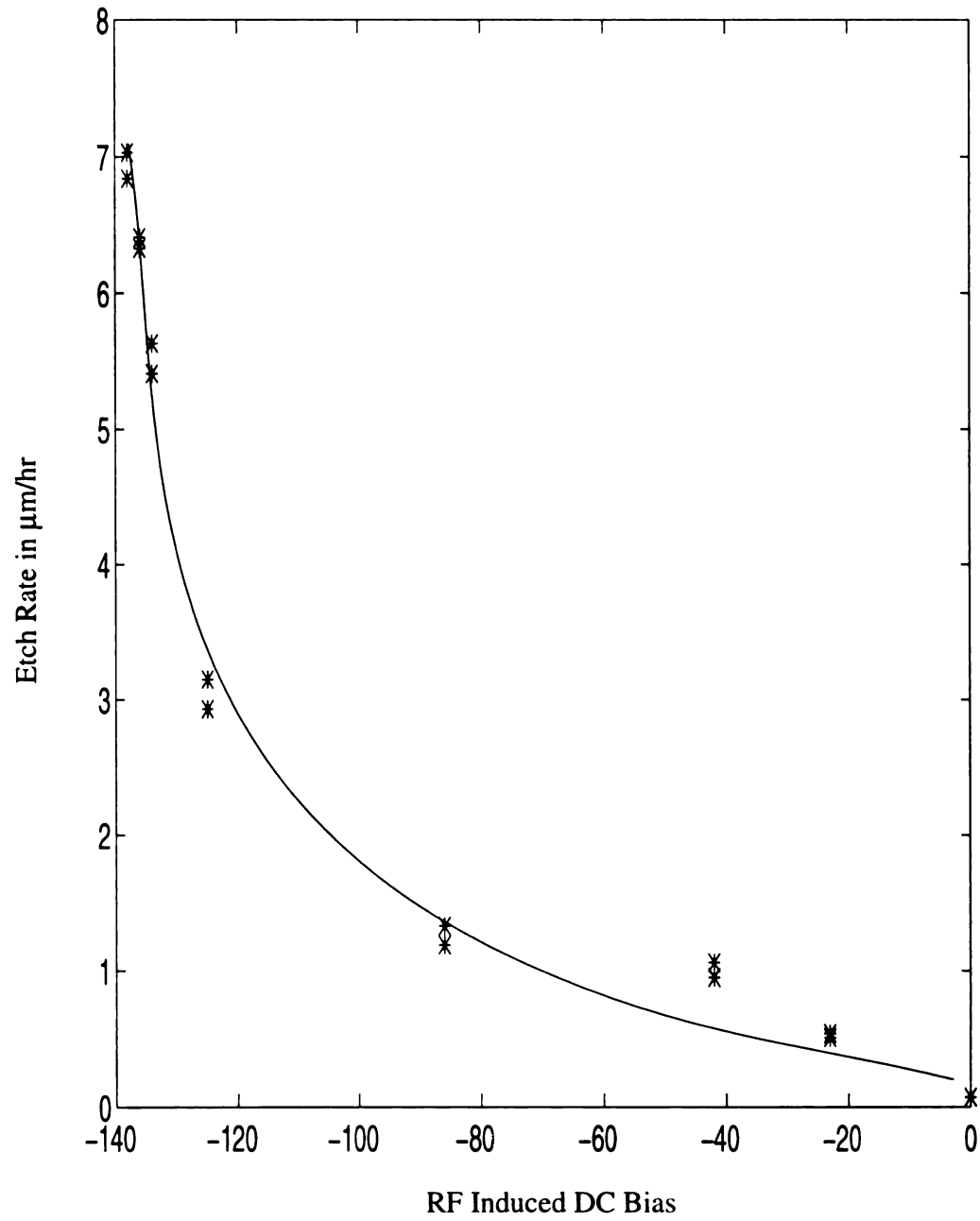


Figure 5.5: Etch rate vs. rf induced dc bias

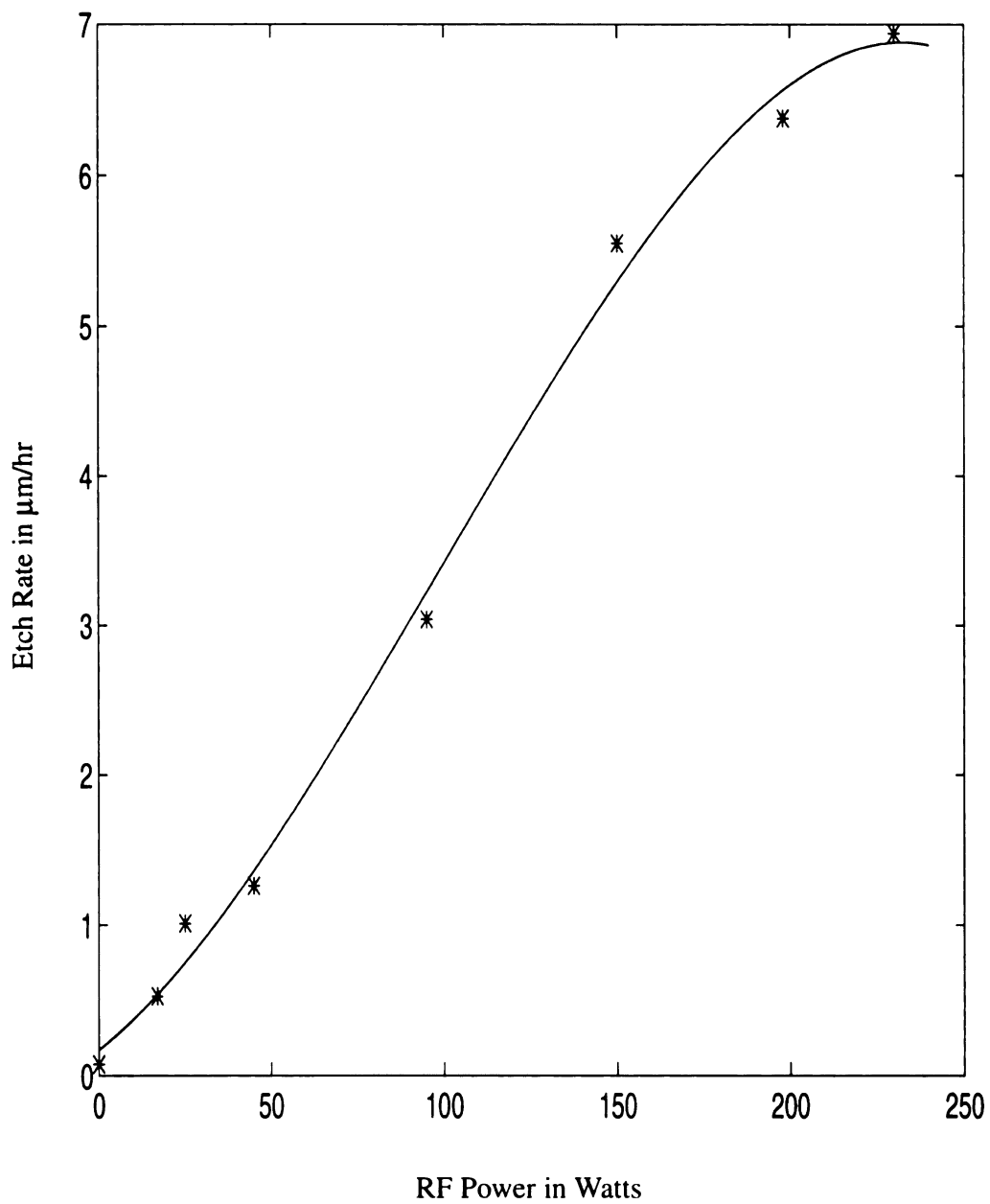


Figure 5.6: Etch rate vs. rf power

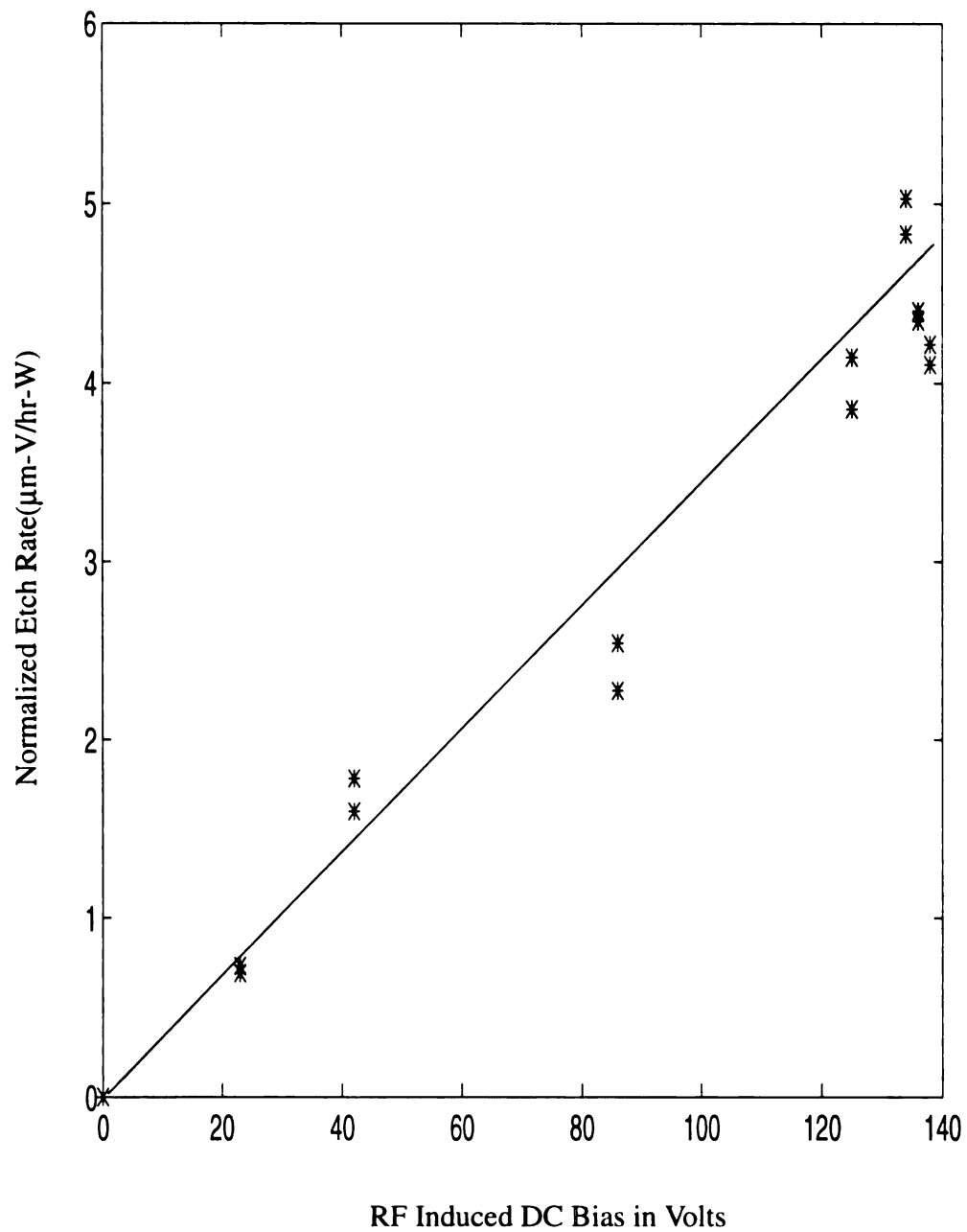


Figure 5.7: Normalized etch rate vs. rf induced dc bias

energy of incident ions. Evidence supports this assumption and confirms that the rate of formation of C:O was not exceeded by the ion-energy driven desorption process at least in the region of our experimental investigations.

5.4.2 Effect of Microwave Power on Etch Rate

We have discussed before that the microwave input power plays a determinant role in establishing the density of the ions inside a discharge. Although the species generation zone is mainly confined around the static ECR magnetic fields, the increased species density in this region is redistributed in the volume of the discharge by the diffusion process. Thus, at steady state, for higher microwave input power, the ion density at the sheath boundary is expected to increase with increased power causing the etch rate to go up. A set of experiments was carried out on a 92 mm wafer TF 271 to confirm the diamond etch rate dependence on microwave power, the results of which are presented in Table 5.12. Parameters other than the microwave power were kept at constant values. The absorbed rf power was kept at 95 watts with an induced dc bias of ~ -125 V, the flow rates of argon, oxygen and SF₆ were fixed at 6, 28, and 2 sccm respectively, the pressure and the mode were chosen at 4 mtorr and 248.08 mm of sliding short height, the downstream distance was fixed at 5.5 cm from the base-plate position. Table 5.12 shows that over this range of power, increasing the power by a factor of 2.5 increases the etch rate by a factor of 1.8. The variation of the etch rate with microwave input power is shown in Figure 5.8 with the solid line representing the best cubic polynomial fit to the data points.

A separate set of experiments was also conducted on a different sample at a different mode to explore the higher region of the microwave power. During these new experiments,

Table 5.12: The Effect of microwave power on etch rate

Microwave Power (Watts)	$\mu\text{m/hr}$ TF 271
200	2.14 ± 0.02
300	2.55 ± 0.05
400	2.99 ± 0.07
500	3.81 ± 0.18

the power was varied between 600 and 800 watts. Other variables, e.g, the rf induced dc bias to the substrate, the pressure, the downstream distance and the cavity mode were held constant at $\sim 120\text{V}$, 4 mtorr, 5.5 cm. and 236.54 mm cavity height respectively. The flows of Ar, O₂, and SF₆ were kept constant at 6, 25 and 2 sccm. The data obtained from these experiments are plotted in Figure 5.9 and the results show a very similar characteristic as obtained from the previously stated experiments conducted on lower microwave power region. Over this range of power, increasing the power by a factor of 1.33 increases the etch rate by a factor of 1.3. In short, for the overall range of power explored, increase in microwave power increases the etch rate of diamond at a more or less steady rate.

On a different context, the role of microwave input power was investigated by etching diamond with and without the input of microwave power. With only rf and no microwave power input, a plasma is generated inside the processing chamber. Etching experiments were carried out with the rf only plasma at two different levels of rf power, 100 watts and 200 watts which induced -156 V and -171 V respectively. The experiments were conducted in an argon, oxygen, SF₆ plasma with individual gas flow rates of 6, 28 and 2 sccm.

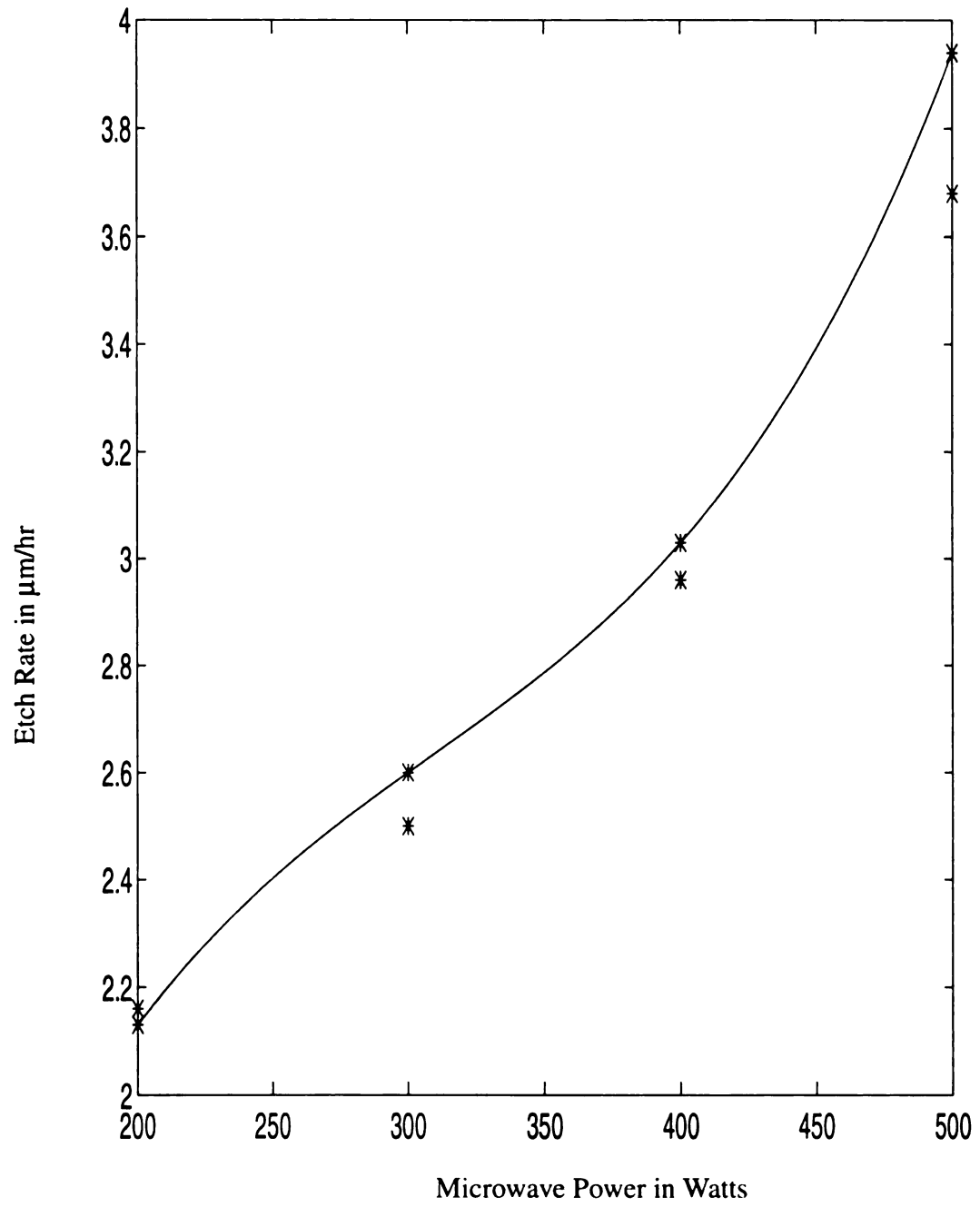


Figure 5.8: Etch rate vs. microwave power at low power level

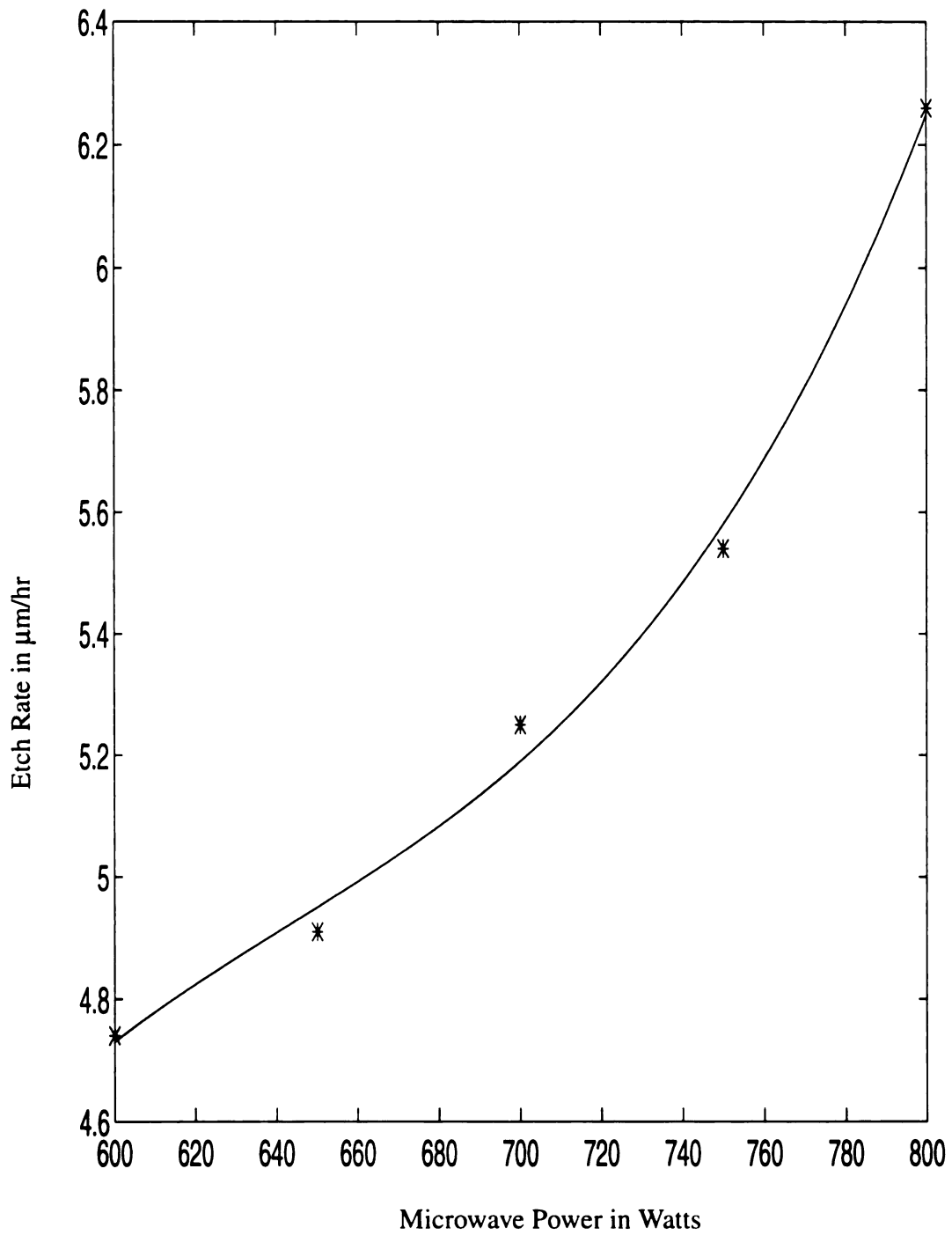


Figure 5.9: Etch rate vs. microwave power at high power level

The main chamber processing pressure was kept at 4 mtorr and the operating resonant mode corresponded to 248.08 mm of cavity height. The substrate height was fixed at 5.5 cm below the base plate.

Etching with 100 watts of absorbed rf power at the substrate in absence of any microwave input power produced an etch rate of $\sim 0.57 \mu\text{m/hr}$, which in the presence of 500 watts of microwave and 100 watts of rf power improved to $\sim 3.68 \mu\text{m/hr}$. This shows that the etch rate increases by more than a factor of 6.45 in presence of 500 watts of microwave power. Similarly with only 200 watts of rf input power in absence of any microwave power, the etch rate became $0.91 \mu\text{m/hr}$ which with an input of 500 watts of microwave power and 200 watts of Rf power increased to $\sim 6.33 \mu\text{m/hr}$. In this case, the ratio of etch rates with 500 watts of microwave power to zero microwave power becomes 6.94.

Two important observations can be made from these experiments. One, the presence of microwave power is important in producing a higher ion flux to the substrate and thus a higher etch rate of diamond. Two, the plasma generated from only rf input is capable of etching diamond, although at a very low rate. The poor rate is mainly attributed to the low species density generated by the rf only plasma in contrast to the ECR microwave generated plasma. Note that from Figure 5.4 the substrate bias and therefore incident ion energy was actually somewhat higher with rf only plasma.

5.4.3 Effect of Processing Pressure on Etch Rate

The processing pressure inside a fixed-volume main chamber determines many characteristics of the plasma, the most important being the species density and their temperature. Other characteristics such as the residence time of the species, the sheath voltage etc.,

are also influenced by the processing pressure.

Since the microwave energy is coupled to the electrons first which through collisions ionize the gas to ignite the plasma, the effect of the pressure can be easily seen during igniting a discharge. Often a discharge cannot be created at a very low pressure e.g., 1 mtorr, hence a common practice is to initiate a discharge at a higher pressure such as 7 mtorr and bring it down to the lower processing pressures. However, the effect of pressure on etch rate was experimentally explored on a 50 mm wafer NTA1-005 with an argon, oxygen and SF₆ plasma having corresponding flow rates of 12, 20 and 2 sccm. For all the experiments, the mode was fixed to 236.54 mm of sliding short height, the downstream distance was 5.5 cm and the microwave power was 600 watts. The rf induced dc bias was held constant about 120 V and the pressure was varied between 2 and 10 mtorr. The variation of etch rate with main chamber pressure is plotted in Figure 5.10.

The result shows a maximum etch rate around 4 mtorr. The reason for this is thought to be due to a counter-acting effect of pressure on sheath potential and the species density. For an ECR plasma, the plasma species density increases with increasing pressure [5.15] but sheath potential and hence the incident ion energy decreases with the increasing pressure [5.16]. Etch rate being a function of the ion energy and incident species concentration, a combination of these two effects are likely to produce the observed maximum in etch rate vs. pressure. Since 4 mtorr produces the maximum etch rate, most of the etching runs were conducted with pressure fixed at this value.

5.4.4. Effect of Oxygen, Sulfur Hexafluoride Ratio on Etch Rate

SF₆ became a part of the gas composition for diamond etching because a black film

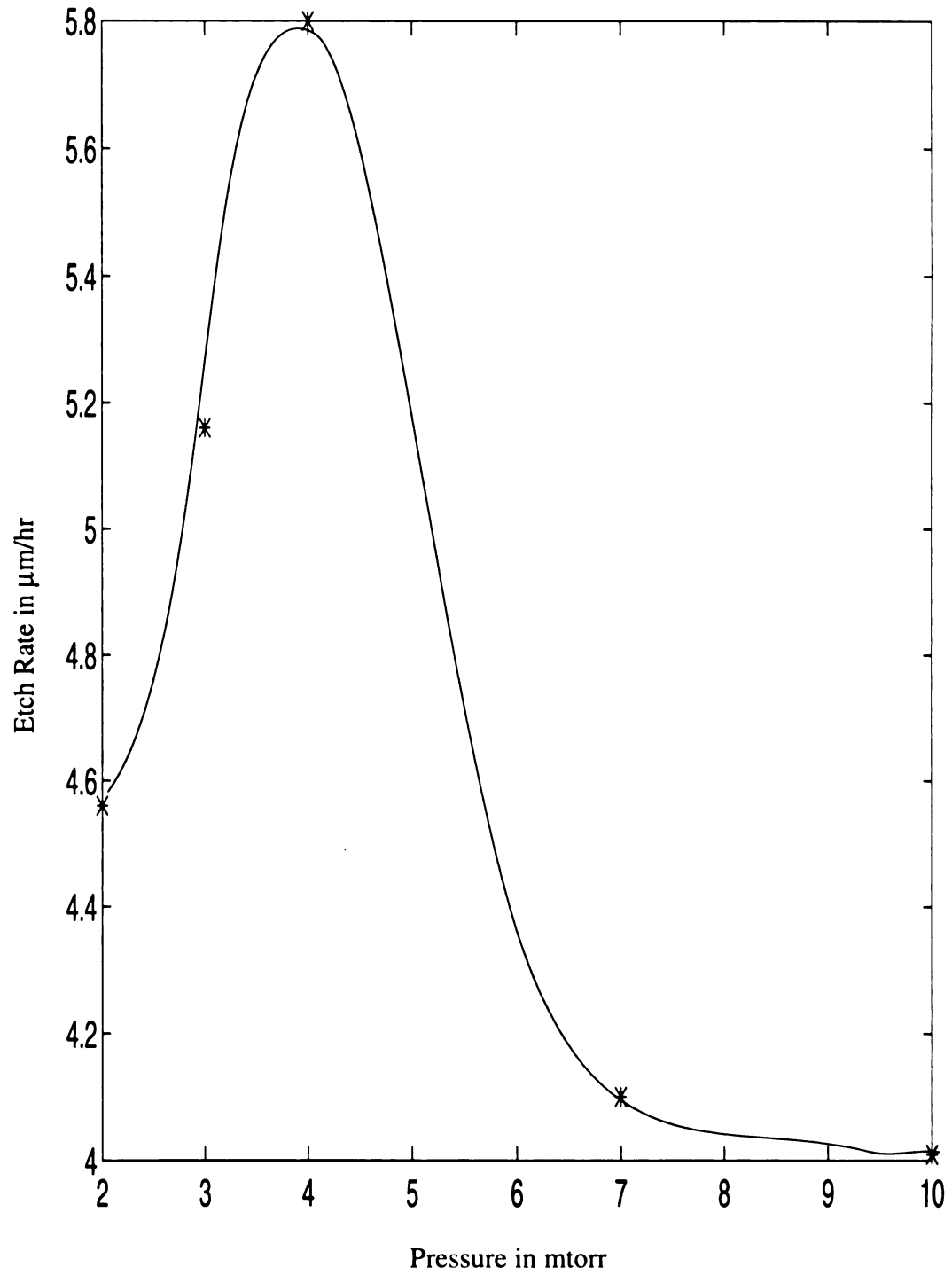


Figure 5.10: Etch rate vs. process pressure

was found to form on the etched surface when oxygen only plasma was used for etching. Later it was found that sputtering with argon only plasma also forms the black film. However, addition of a little amount of SF₆ in the plasma environment prevented the formation of the black layer.

It was noticed that SF₆ containing plasma can also clean an already formed black layer as well. Thus a fluorine containing plasma was chosen for etching diamond although the statistical analysis showed that SF₆ has a negative effect on diamond etch rate. To investigate the effect of SF₆ on the etch rate more carefully, a set of experiments was designed where the oxygen flow rate was kept fixed at 28 sccm and the SF₆ flow rate was changed from 0 to 8 sccm. Argon was not flown through the system. All experiments were repeated and the results obtained are presented in the Table 5.13. The plot in Figure 5.11 supports the negative effect SF₆ on etch rate. The etch rate was found to decrease as the SF₆ to oxygen ratio was increased. For these experiments pressure and the downstream distance were kept at 4 mtorr and 5.5 cm respectively.

Table 5.13: Effect on SF₆ to oxygen flow ratio on etch rate

SF ₆ Flow Rate	O ₂ Flow Rates	SF ₆ : O ₂ Ratio	μm/hr TF 271
8	28	0.28	0.76 ± 0.03
6	28	0.21	1.67 ± 0.05
4	28	0.14	2.85 ± 0.03
2	28	0.07	3.92 ± 0.22
0	28	0	5.51 ± 0.141

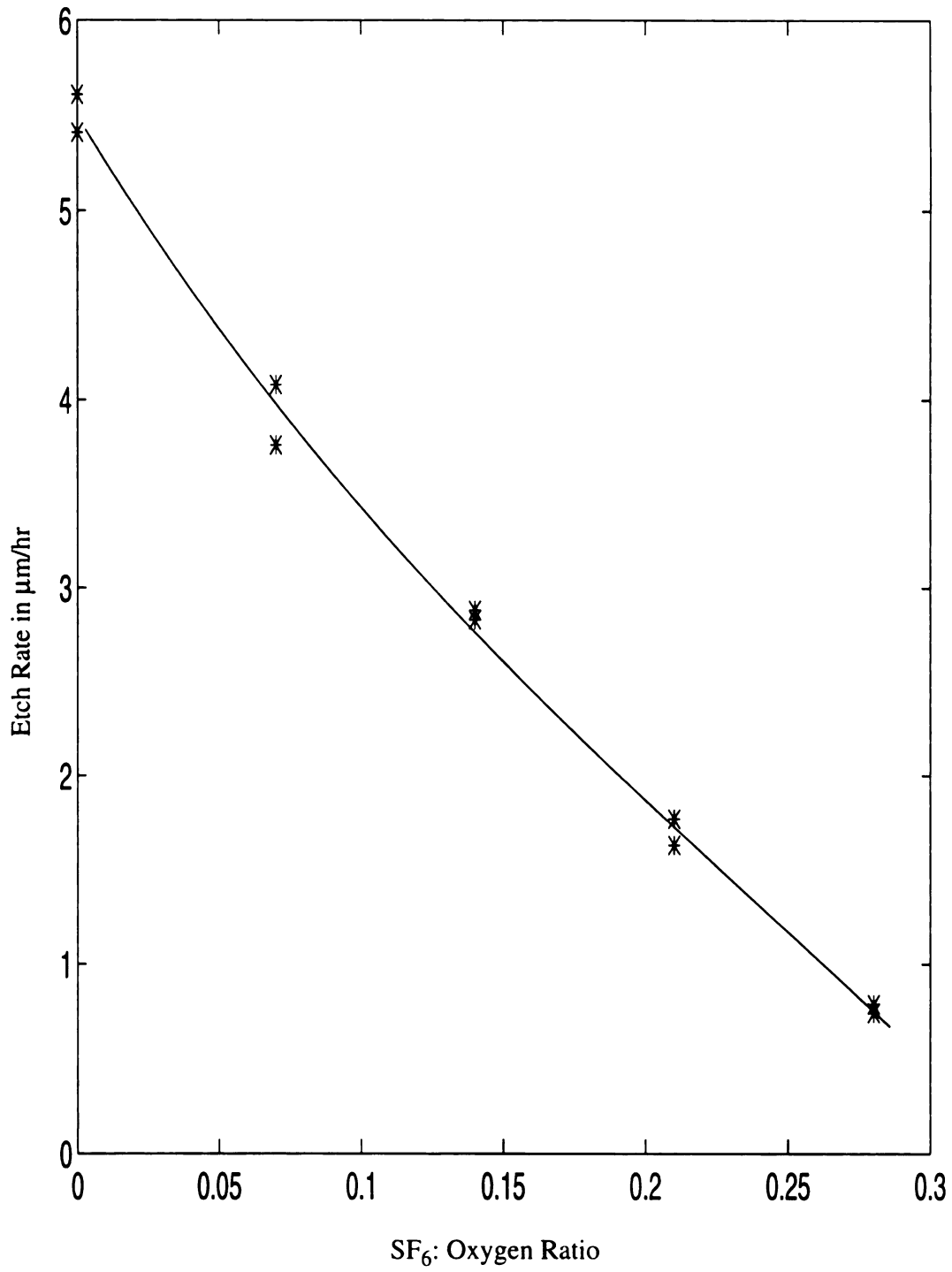


Figure 5.11: Etch rate vs. SF_6 to oxygen flow rate ratio

The microwave input power was 500 watts and the rf power was 100 watts which induced a dc bias of ~128 V. The reason for the negative effect of SF₆ is not clear. Addition of SF₆ may modify the internal plasma chemistry in a complex way. Also fluorine and oxygen may compete for the surface sites on the diamond substrate. The value of rate constants of carbon-oxygen and carbon-fluorine reactions differ in magnitude which would contribute to the change in etch rate.

However, an exception to the negative effect of SF₆ on etch rate was noticed while etching a diamond film with an already-formed black film on the surface. It was found that an addition of 2 sccm of SF₆ in a 6 sccm to 28 sccm of argon-oxygen plasma increases the etch rate by about 33%. This is apparently contradictory of the negative effect SF₆ as seen in Figure 5.11. But the experiment was repeated three times and etch rate of the black layered diamond was confirmed to increase with slight addition of SF₆. These preliminary results tend to imply that the black film etches at a slower rate in absence of SF₆, although diamond without any black film etches at a faster rate in absence of SF₆. However, a question about the possible role of argon remains because Figure 5.11 was generated for an oxygen:SF₆ plasma as opposed to the argon-oxygen-SF₆ plasma.

Hence a fresh set of experiments was conducted with argon-oxygen-SF₆ plasmas. For these experiments, the argon and oxygen flows were kept constant at 6 and 28 sccm, and the SF₆ flow rate was varied between 0 and 8 sccm at a fixed processing pressure of 4 mtorr. Thus the proportional content of fluorine atoms and ions were changed in the plasma as the flow rate of SF₆ varied from experiment to experiment. The microwave and rf input power were fixed at 500 watts and 100 watts respectively for all experiments.

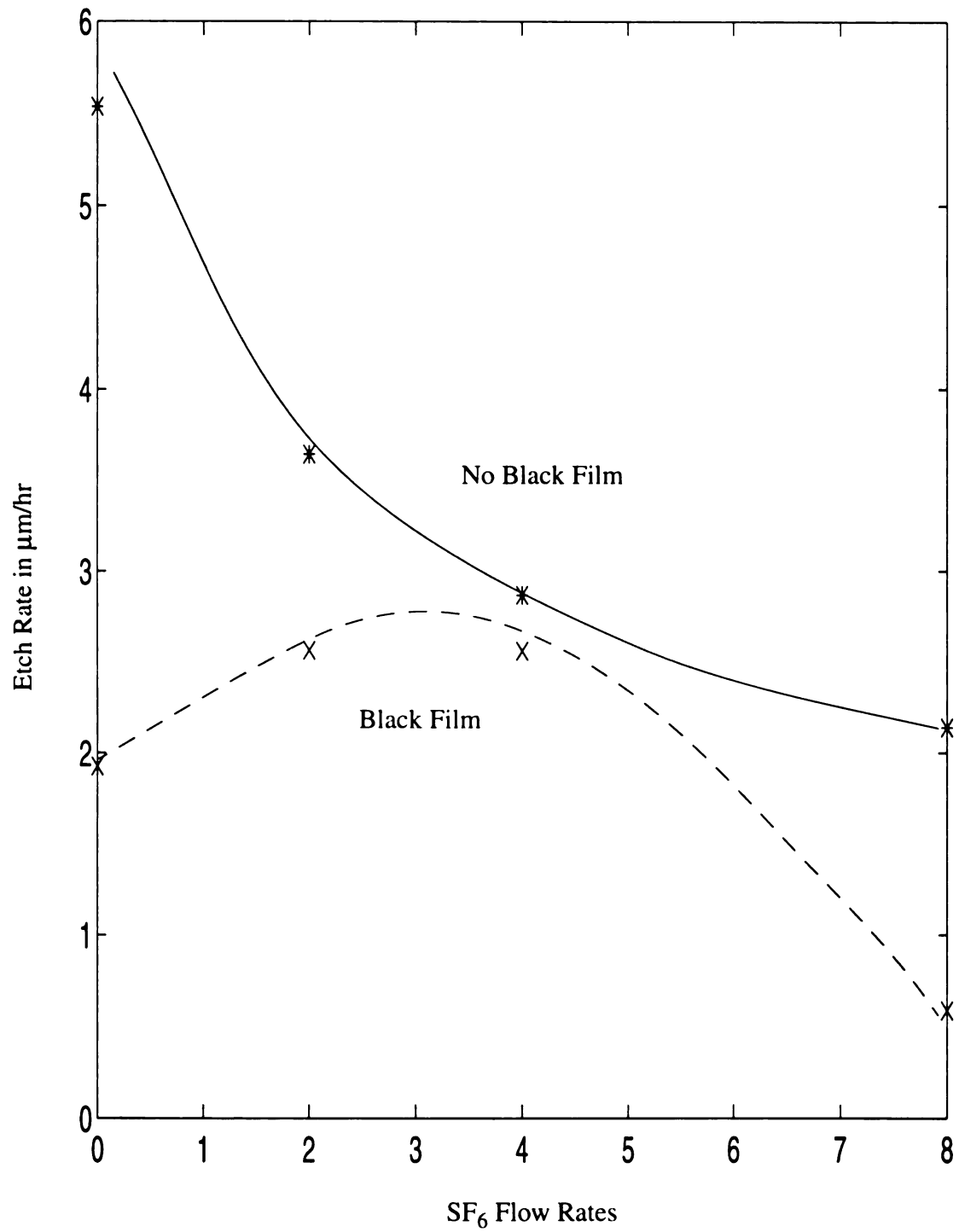


Figure 5.12: Etch rate of diamond with and without black film

The downstream distance was chosen to be 5.5 cm and the mode was fixed at 251.71 mm of cavity height. The 92 mm diameter sample TF 271 with no black film on the substrate side was etched in the argon-oxygen-SF₆ plasma and the etch rate was indeed found to decrease with increase in SF₆ flow rates supporting the similar observation obtained while etching in an only oxygen-SF₆ plasma. Thus argon was eliminated as the source of an anomaly seen with regard to the increase in etch rate with addition of SF₆ while a black-layered diamond was etched.

To study how the etch rate of the black film changes with the content of SF₆ in plasma, black film was grown on the substrate side by sputtering with an argon only plasma and then the sample etched in the same argon-oxygen-SF₆ plasma used to etch the sample without the black layer. Figure 5.12 shows that as the SF₆ flow ratio increased, the etch rate first increased and then decreased. This indicates that the presence of SF₆ is important to keep the etch rate up but beyond a certain point, a higher concentration of SF₆ does not aid the etching mechanism. An initial conclusion, that in absence of SF₆, a black film layer grows on the diamond which acts as a passivation layer and reduces the etch rate was drawn from these experiments. However, more experiments were required to confirm the hypothesis. These experiments were performed and are described in section 5.5.

5.4.5 Effect of Argon, Oxygen Ratio on Etch Rate

The mode corresponding to 248.08, which was used most often for Ar, O₂ and SF₆ plasmas did not seem to be an appropriate resonant mode for argon-oxygen plasma, especially for high argon content, because the returned microwave power was observed to be quite

high regardless of the probe length. The plasma was also found to flicker at times. The sliding short was therefore changed to 251.71 mm of cavity height which seemed to produce a steady, bright discharge with less microwave returned power.

Table 5.14: Effect on argon to oxygen flow ratio on etch rate

Argon Flow Rate	Oxygen Flow Rates	Oxygen to Argon Ratio	$\mu\text{m/hr}$ TF 271
6	0	0	0.14 ± 0.08
6	2	0.33	0.64 ± 0.18
6	6	1	1.22 ± 0.04
6	14	2.33	1.37 ± 0.02
6	28	4.66	1.49 ± 0.04

In order to investigate the effect of argon to oxygen ratio on the etch rate of diamond, the microwave absorbed power was kept constant at about 400 watts and argon gas flow was fixed at 6 sccm. The absorbed rf power was fixed around 95 watts with an induced dc bias of -125V. The downstream distance was chosen to be 5.5 cm and the pressure was kept constant at 4 mtorr.

The results of the experiments are shown in Table 5.14 which are plotted in Figure 5.13. The etch rate initially showed a drastic increase with oxygen flow ratio but as the oxygen content is increased beyond a certain ratio of the total gas flow, the etch rate showed a saturation behavior. The reason for this observation lies with the change in nature of etching from sputtering to RIE. Argon being a noble gas does not participate in reactive ion etching, hence in an argon only plasma, etching becomes purely sputtering

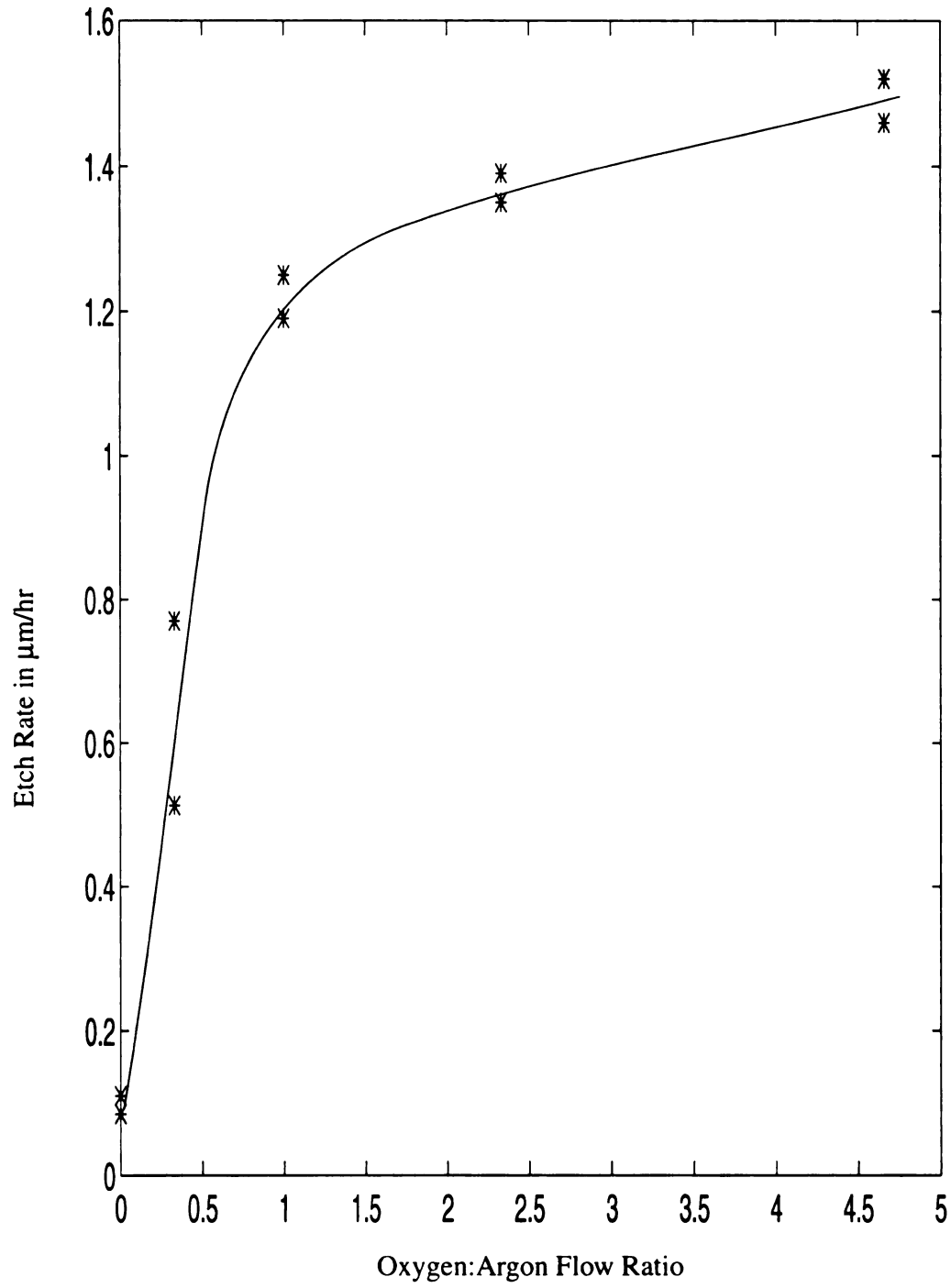


Figure 5.13: Etch rate vs. oxygen to argon ratio

and an extremely low etch rate is produced. As oxygen is introduced to the discharge, the etching changes from sputtering to RIE showing a drastic improvement in etch rate. With gradual increase of oxygen flow ratio to argon, the density of oxygen atoms and ions starts dominating the plasma and the rate of etching shows a continuous improvement. However, increase in oxygen flow beyond a point does not help in increasing the proportion of oxygen content in plasma significantly, therefore the etch rate shows a saturation phenomenon. It might be useful to indicate here that although the etch rate was found to increase with oxygen content ratio in the etching plasma, the etch rate of diamond film was unusually low, in an argon-oxygen plasma. In fact, with other parameters being constant, the plasma etching experiment with 6 sccm of argon and 28 sccm of oxygen shows that the etch rate obtained is less than a factor of 4 compared to the etch rate obtained in an argon-oxygen-SF₆ plasma with flow rates of 6, 28 and 2 sccm. It is believed that this happens because during each step of argon-oxygen etch experiments, a black film is formed due to the absence of SF₆ which etches at a lower rate than a non-black-layered diamond. The effect of changing the flow rate of argon in an oxygen rich plasma environment was not explored in detail. A few experiments were conducted, but the etch results were not found very conclusive. However, we believe that the presence of argon in an oxygen plasma seems to stabilize the plasma and reduce the return microwave power.

Argon-only sputtering experiments were also performed. Our previous experiments studying the effect of rf bias on the etch rate of diamond, successfully demonstrated that etching of diamond in argon-oxygen-SF₆ plasma was definitely ion assisted. The argon only etching experiments allow differentiating between sputtering and RIE. With argon sputtering experiments, 400 watts of absorbed microwave power at 4 mtorr pressure, and

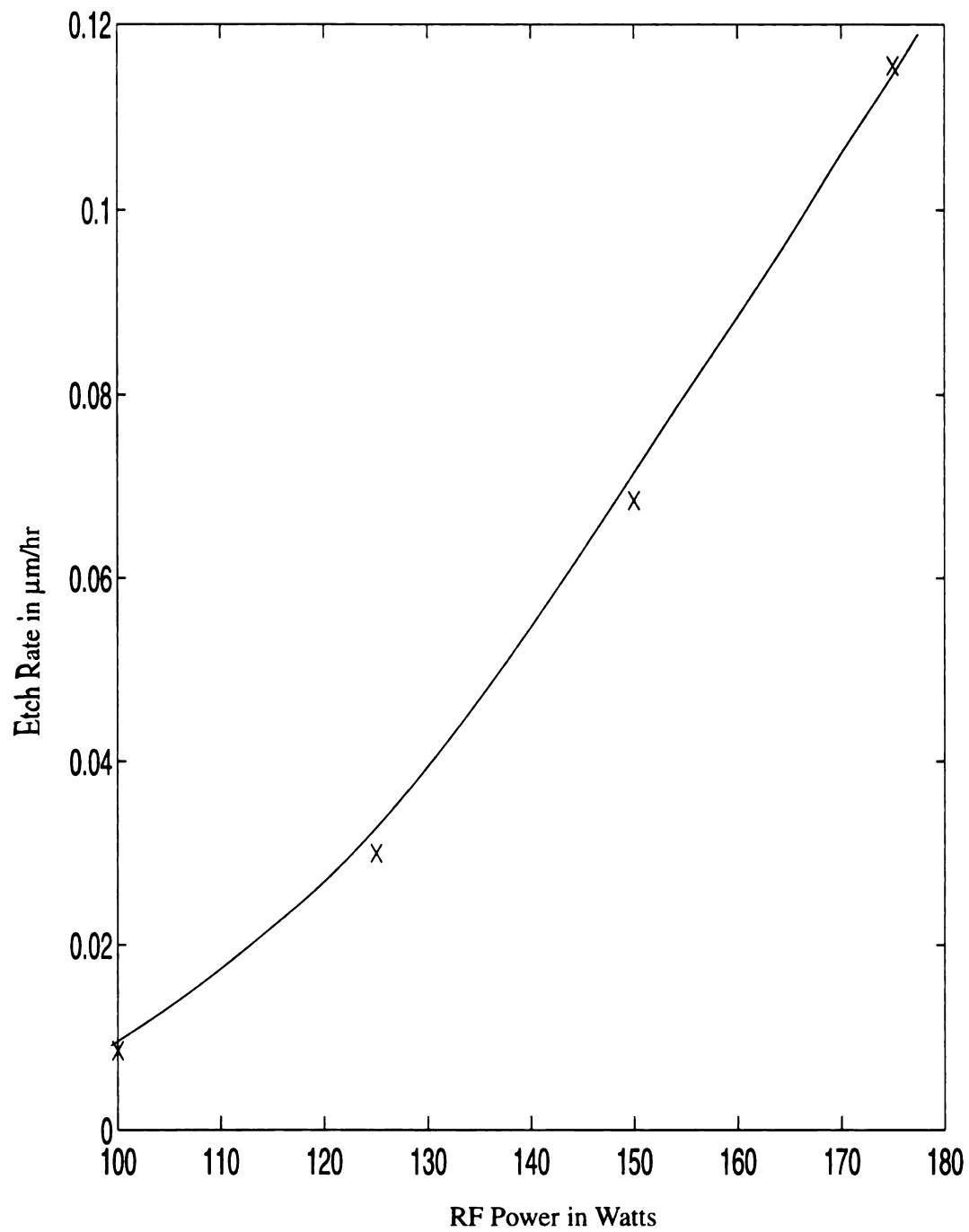


Figure 5.14: Sputter etch rate vs. rf power

an input of 100 watts of rf power produced a diamond removal which was only about 0.4% of the etch rate produced by an argon-oxygen-SF₆ plasma under similar parameter specifications. This clearly demonstrates that the etching mechanism in an argon-oxygen-SF₆ plasma is reactive ion etching dominated. As an extension of the sputtering experiments, the bias dependence of sputtering in an microwave ECR was explored and the results are shown in Figure 5.14. 500 watts of microwave input power, 4 mtorr pressure, 5.5 cm of downstream distance and the mode corresponding to 251.71 were chosen as the parameters for these sputter-experiments.

Figure 5.14 shows that rf power increases the sputtering rate although the rate always remained in the order of a tenth of a micrometer/hr even with at the highest value of rf power investigated.

5.4.6 Effect of Downstream Distance on Etch Rate

We have seen from the previous discussion in section 5.1, that the steady state spatial distribution of species density decreases along the downstream distance, which was experimentally verified by Gopinath et.al., for argon sputtering and theoretically derived using simplified assumptions by Hopwood et.al., [5.2, 5.3]. The effect of downstream distance on etch rate due to reactive ion etching is expected to be similar to the that of the sputtering. However, experiments were conducted to quantify this effect.

An argon, oxygen, SF₆ plasma at 4 mtorr was used for etching the wafer. The flow rates were 6, 28 and 2 sccm for argon, oxygen and SF₆ respectively. The input microwave and the rf power were fixed at 500 watts and 200 watts. The induced dc voltage from the rf power was about -140 V. The etch rate of a 92 mm diameter diamond disk TF 271 at

10.2 cm downstream distance was found to be $4.06 \mu\text{m/hr}$ as compared to $6.33 \mu\text{m/hr}$ at 5.5 cm downstream distance. The experiment showed an average increase in etch rate by a factor of 1.56 when the downstream distance is decreased from 10.2 cm to 5.5 cm. For the same change of downstream distance, the theoretical expression from Hopwood [5.3] predicts the average etch rate to improve by a factor of 1.58 which closely matches our experimental observation.

Since, the etch rate strongly depends on the downstream distance for obtaining higher etch rate, the etching must be performed as close to the plasma generation region as possible. However, that is not always done because of some other reasons. The uniformity of the etching may suffer over a larger area substrate at lesser downstream distance because the etching profiles may follow the spatial patterns of the resonant modes. At larger processing distances, the modal effects are washed away and similar etch profiles would be obtained from all modes independent of the individual modal patterns.

Another practical problem arises when processing is performed at shorter downstream distance. Since, the rf power flowing through the substrate for a given induced dc voltage is dependent on the species density, the rf power flow through the substrate for a given induced dc bias and given absorbed microwave power increases as the downstream distance becomes shorter. For a given maximum power handling capability of the rf power generator and the matching network, the applied dc bias or the setting value of the rf power and the absorbed microwave power together determines a cut-off distance between the substrate and the plasma. If the substrate is forcibly brought closer than this minimum downstream distance, the rf power tends to flow more than the power handling limit, which initiates a protective circuitry in the rf matching network and shuts the system. Thus

the substrate must not be brought too close to plasma in order to keep a high substrate bias.

5.4.7 Effect of Resonant Modes on Etch Rate

Not all electromagnetic resonating modes are suitable for ECR energy coupling [5.4] and the mode appears to shift with loading of the cavity. During the argon-oxygen experiments shown in Figure 5.13, the cavity height corresponding to 248.08 was not found appropriate for argon only and high argon/low oxygen containing experiments. The plasma was found to flicker although the 248.08 mode was consistently successful in creating argon-oxygen SF₆ plasma especially for high oxygen and low argon contents. The mode corresponding to 251.71 was found quite stable for argon-oxygen experiments as well as only oxygen experiments. The individual electromagnetic modes for MPDR 325i are difficult to uniquely identify because of its large discharge diameter. Therefore, in this work, the modes are described in terms of the cavity height. The scope of our research at this point was not to identify the operating modes and we assumed that a fixed cavity height represents a unique mode or a unique combination of modes which are repeatedly obtained when the cavity height was adjusted to that value. Such an assumption neglects hysteresis or mode related instability effects [5.17] that might occur in practice.

We know that the spatial distribution of the density of species is determined by the operating mode and that the ions that reside over a given area of the substrate mainly participate in etching. Therefore the average etch rate which is related to the total ions over the work-piece area, can certainly be expected to vary from mode to mode. However, large area processing with MPDR 325i does not appear to produce a very widely varying

average etch rate for different ECR resonating modes. An example of the etch rate variation is given in the Table 5.15. In this case, the plasma and the wafer conditions were more or less identical and two modes were chosen corresponding to 251.71 and 248.08 mm of cavity height respectively.

Table 5.15: Effect of resonant mode on etch rate

Plasma	Mode	$\mu\text{m/hr}$ TF 271
Ar:O ₂ :SF ₆ => 6:28:2	248.08	3.15
Ar:O ₂ :SF ₆ => 6:28:2	251.71	3.64
O ₂ => 28	248.08	5.51
O ₂ => 28	251.71	5.64

The etching runs were conducted with 400 watts of absorbed microwave power and 100 watts of rf power with the downstream distance fixed at 5.5 cm. The pressure was kept constant at 4 mtorr.

5.5 Black Film

In the last section, we noted that diamond etched in an only oxygen, only argon, or in argon-oxygen mixed plasma showed a black film on the etched surface. Also the diamond with a black film etched at a lower rate than diamond with no black film. Moreover, some initial results indicated that the presence of SF₆ was necessary to keep the diamond etch rate from falling from run to run due to the formation of the black film. To investigate this further, a diamond sample with no initial black film was etched successively in a plasma containing no SF₆. For this investigation, an oxygen only plasma was chosen with an input

microwave power of 500 watts. The rf power was set at 100 watts and the pressure was fixed at 4 mtorr. The wafer TF 271 was placed 5.5 cm below the base-plate. The etch rate dropped with successive runs. This is shown in Figure 5.15. The decreasing nature of the etch rate implies that at the end of each run the surface of the diamond was becoming more and more etch resistant to oxygen plasma causing the etch rate to go down. To the naked eye, the film appeared to grow as black dots on the surface which became more and more intense as the etch hours proceeded. This clearly suggested that the black film was acting as a passivation layer on the diamond surface and for unknown reasons, the presence of SF₆ prohibited the growth of this passivation layer. Also as noted earlier, SF₆ cleans the passivation layer in case it was already grown. To verify this hypothesis, a reverse experiment was conducted. The same wafer TF 271 with an already-grown black film was now etched in an argon-oxygen-SF₆ plasma successively. The gas flow rates were 6, 28 and 2 sccm for argon, oxygen and SF₆ respectively. Other parameters were fixed exactly at the same specifications as the above-mentioned only oxygen plasma experiment. As expected, the etch rate increased with successive runs which can be seen from Figure 5.16. In conclusion, the presence of SF₆ is found essential to keep a constant high etch rate of diamond although if the proportion of SF₆ is continually increased in the plasma, the etch rate starts falling beyond a certain SF₆ to oxygen ratio (approximately 8%). In all experiments, the etch rate of the black film coated diamond was always found lower than the etch rate for diamond with no black film under the same plasma specifications. It was also noted that the actual etch rate of the black film is dependent on how the film was grown. For example, visual inspection showed that argon sputtering produced a more blackish film than oxygen plasma etching for the semi-transparent black-film-less

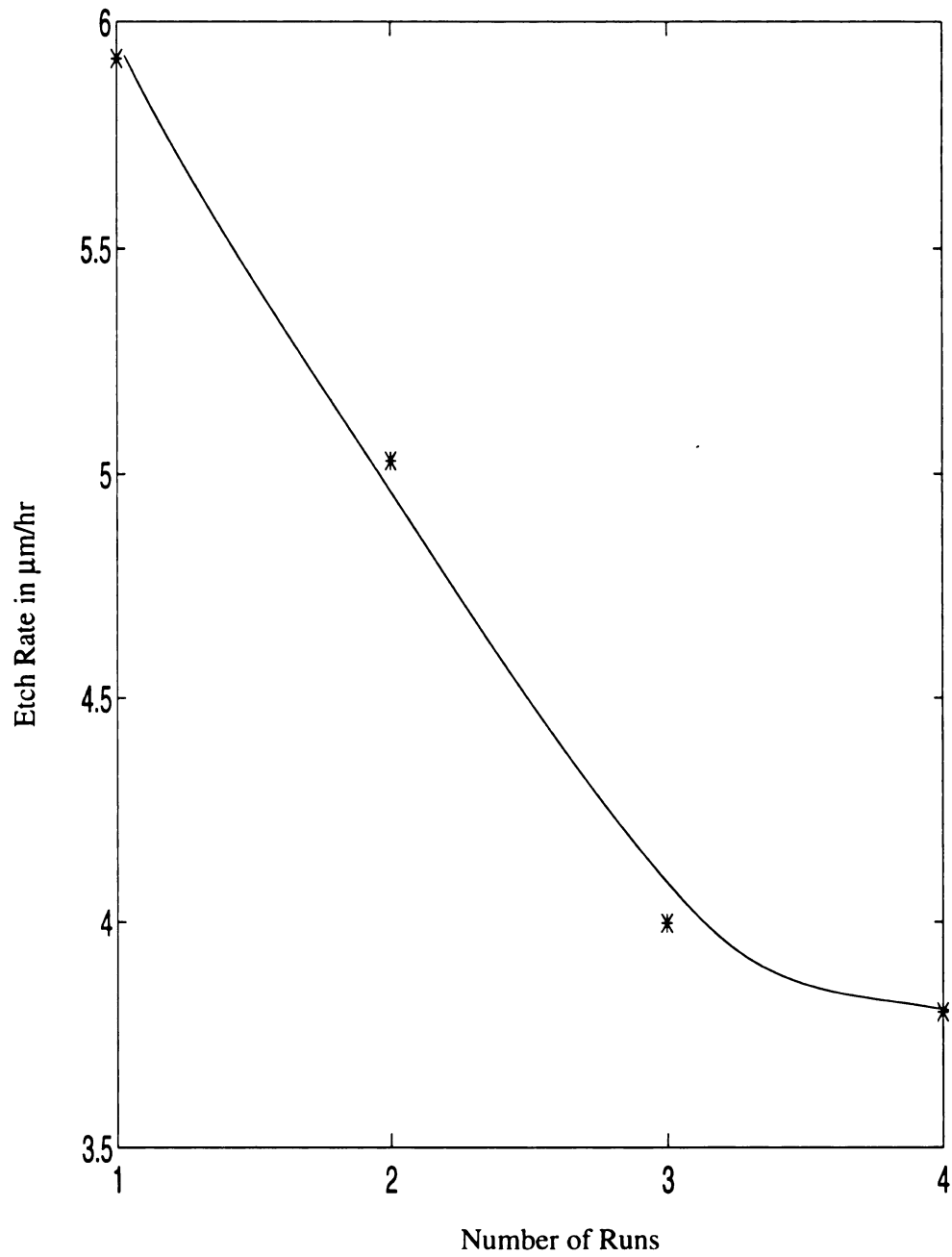


Figure 5.15: Subsequent etching of diamond in oxygen plasma

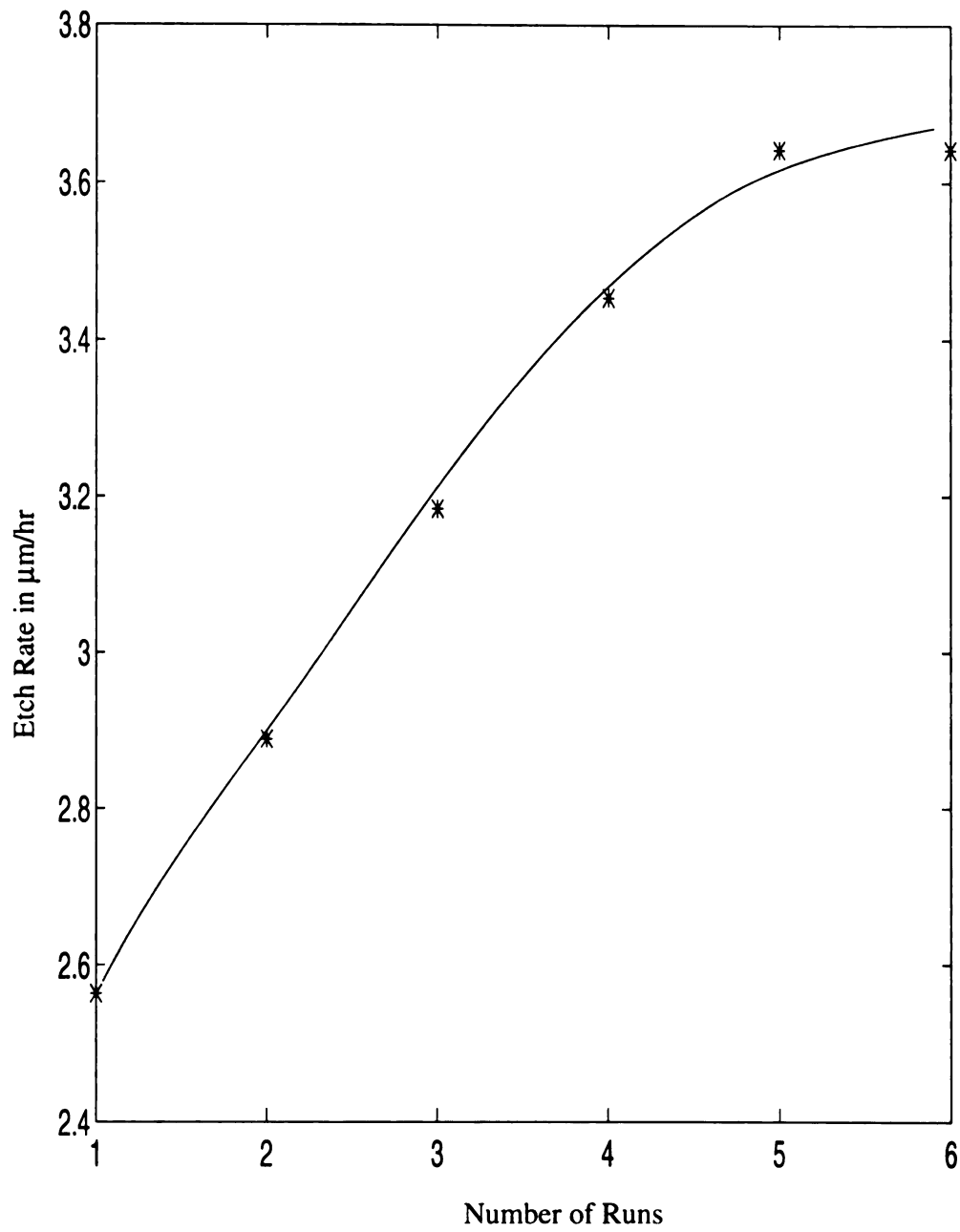


Figure 5.16: Etching of black film with Ar, O₂ and SF₆ plasma

sample TF 271. The black film visually appeared to become increasingly prominent as the total etching hours increased both for argon sputtering and oxygen etching. This observation led to some obvious questions, such as whether the black films produced by an oxygen only, argon only and argon-oxygen mixed plasma were identical and whether the nature of the black film produced at the end of one hour run was same as the film produced at the end of two hour runs. The answers to these questions are actually related to quantifying the black film and understanding the cause of its formation. We have not done an extensive study of the black film. However, some initial results and some possible hypothesis based on our initial work are presented next.

An independent study reported the use of SF_6 containing plasma to clean metal parts [5.18]. Using Ar, O_2 , SF_6 plasmas, it was found that SF_6 was necessary to remove graphite containing lubricant. This report together with our observation of cleaning the black film in SF_6 containing plasma, lead to a possibility that the black layer is possibly a graphitic layer. As a preliminary investigation, Raman spectrum was taken on an argon sputtered

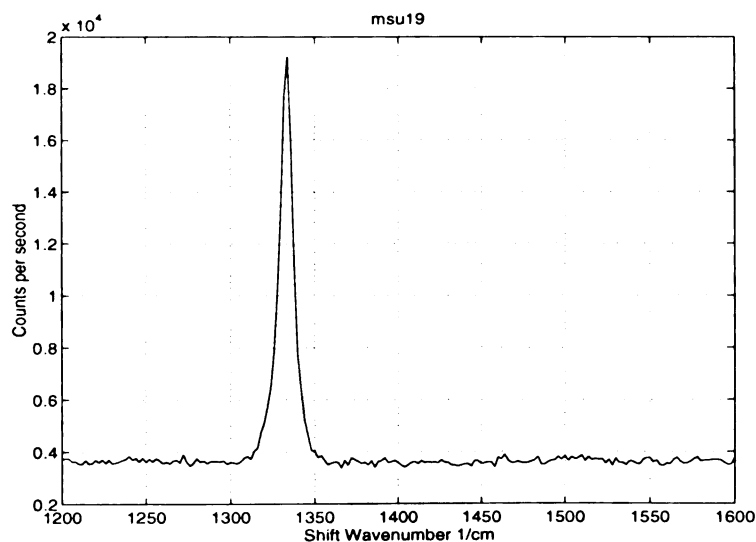


Figure 5.17: Raman spectrum

black layer coated diamond film. The result of this investigation, presented in Figure 5.17, did not show graphite sp^2 bonds. However, Raman analysis as used for Figure 5.17 is not specifically a surface analysis method.

An alternative explanation for black surfaces following plasma treatment is found in Chapman [5.19]. When surface treatment results in a surface morphology with a high scattering coefficient for visible light, a black velvet appearance may result. A specific example is the sputtering of copper substrates which under certain conditions can result in a surface covered with sub-micron cone-like structures. It was noted that the pictures of such surfaces in Chapman were reminiscent of SEM images obtained from Dr. Paul Goldman previously at Norton, on samples which had been etched in this study at Michigan State University. This prompted further SEM examination of the surface morphology of black film coated samples. Since our SEM facility cannot load 92 mm diameter sample, a dc arc-jet deposited 1cm X 1 cm diamond sample MSU-3, was micrographed after removing 50 μm from the substrate side in pure oxygen plasmas. The SEM shown in Figure 5.18, shows globules to appear on the etched surface at a magnification of 1000X.

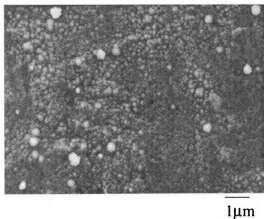


Figure 5.18: Globules on O_2 etched sample

When magnified at 10000X, the SEM shown in Figure 5.19, revealed numerous irregular structures on the etched side of the diamond surface.

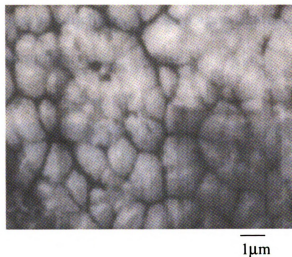


Figure 5.19: Magnified structures of globules

These structures were not seen in a pre-etched sample (Figure 5.20).

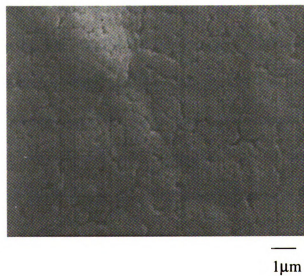


Figure 5.20: Pre-etched sample surface

As noted, SEMs of etched surfaces were also investigated by Dr. Goldman of Norton Diamond Film. One of such micrographs on an oxygen plasma etched semi-transparent 50 cm diameter sample is shown in Figure 5.21. This sample had 50 μm removed from the substrate side in a pure oxygen discharge. The SEM again showed roughly cone shaped formations on the etched surface.

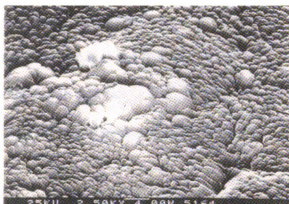


Figure 5.21: Conical structures on O_2 etched sample

Evidence in literature shows that these cones are usually formed from high anisotropic etching such as sputtering. Dorsch et.al., [2.39] postulated that the black film on diamond surface observed from their etching in an rf oxygen plasma, was an optical effect caused by the surface cones. They believed the reason for the formation of cones is micro-masking. According to them, tiny deposits from the wall-chamber fall on the sample and act as micro-masks which are finally responsible for the development of the conical structures seen after etching.

More surface analysis is required to determine for certain the nature of the black film. However, the explanation of cone formation and its optical effect is highly plausible. The nature of both argon sputtering and oxygen only etching are extremely anisotropic which

could result in the formation of the surface cones. However, addition of SF₆ may change the nature of etching to more chemical and less anisotropic. The lateral etching in presence of SF₆ would then be responsible for both cleaning the already-formed cones and preventing the new cones from formation. However, the reason for the initial cone formation, micromasking or other, is not established by our work.

The reduced etch rate of diamond-with-black-film in oxygen plasma could also be explained in the light of the cone formation. In RIE, sidewall etching is low. As the cones form, much of the diamond surface is in the form of angled walls, not receiving the RIE effect. Therefore, a gradual fall in etch rate is seen as the diamond surface grows more and more black during successive oxygen plasma etching runs.

5.6 Calculation of Approximate Diamond Etch Rate in Oxygen ECR Plasmas

In section 5.3, we concluded that the diamond etching in an argon-oxygen-SF₆ plasma with higher oxygen content is mainly RIE. The conclusion can surely be extended for etching in an oxygen only plasma. In this section, we try to relate the theory of reactive ion etching of diamond explained in section 4.4, with the experimental results obtained. This is done by theoretically calculating the diamond etch rate under certain typical plasma conditions for a pure oxygen plasma and comparing the same with the value obtained from the experiments performed in a similar oxygen discharge. The calculation is based on assumptions about the plasma density and species temperature which were not experimentally verified, hence the accuracy of this calculation may be questioned. However, the usefulness of this calculation is to gain an understanding in the reactive ion etching phenomenon for ECR etching.

A typical oxygen only plasma condition is assumed at 400 watts of absorbed microwave power at a fixed processing pressure of 4 mtorr. The absorbed rf power is assumed to induce a typical dc voltage of 120V. Using external cooling, the substrate temperature T_s is normally held at about 30° C or 300 K. ECR plasmas are known as cold plasmas, and from experience we know that the temperature of the cavity does not go very high even without cavity cooling for only 400 watts input. Therefore the temperature of the gas and the ions can be thought to be quite low, say 350 K.

The ions in a processing discharge contribute negligible proportion of the species, usually less than 0.1%, hence most of the species remain neutral the density of which can be calculated using the simple gas law relations shown as follows:

$$\frac{P_1}{n_1 T_1} = \frac{P_2}{n_2 T_2} \quad (56)$$

In expression (56), P_1 , T_1 , n_1 , represent the atmospheric pressure, ambient temperature (300 K) and gas particle density at STP and P_2 , T_2 , n_2 represent the processing pressure, gas temperature, and the oxygen molecule density inside the plasma. For 4 mtorr of processing pressure and 350 K of gas temperature the density of oxygen molecule is calculated as $4.11 \times 10^{19} \text{ m}^{-3}$. We further assume that 10% of the gas molecules, or $4.11 \times 10^{18} \text{ m}^{-3}$, are dissociated inside the discharge and remain in the form of neutral oxygen atoms. It is also assumed that the density of the oxygen atoms at the surface of the diamond substrate n_{OS} is same as anywhere else inside the discharge and is therefore equal to $4.11 \times 10^{18} \text{ m}^{-3}$.

The ions are assumed to be mostly singly charged and with an incident energy of 120

eV since the rf induced dc bias of 120 V comes across the chuck sheath. To be consistent with our previous assumptions made in connection with discussing the effect of rf power on etch rate, we keep the section 5.4.1 value for the electron temperature which was 6 eV. The values for the downstream ion density n_{i_s} is assumed to be and $4 \times 10^{16} \text{ m}^{-3}$.

The atomic volume-density of the diamond n_C is known as $1.79 \times 10^{29} \text{ m}^{-3}$. The activation energy for the diamond oxidation E_b is approximately calculated to be 230 kJ/mol or 2.39 eV per bond from [2.8]. Assuming $\eta \sim 0.2$ for equation (33) we get the ion-enhanced sputter desorption yield Y_i as 10.

Now, the thermal desorption rate constant K_d is related to binding energy of diamond through the following expression:

$$K_d = K_0 \exp\left(\frac{-E_b}{kT_s}\right) \quad (57)$$

where T_s is the substrate temperature and K_0 , the pre-exponential factor represents the number of attempted escapes per second and for chemisorption processes ranges from 10^{13} to 10^{15} . Considering a mean value of K_0 to be 10^{14} , K_d is calculated to $8.4 \times 10^{-27} \text{ s}^{-1}$.

Taking the surface state density n_o' for diamond to be $1.58 \times 10^{19} \text{ m}^{-2}$ for the (111) surface, K_a is determined from equation (46). The value of K_a is $1.08 \times 10^{-11} \text{ cm}^3 \text{ s}^{-1}$.

For an electron temperature of 6eV, the Bohm velocity of oxygen ions $u_B = \sqrt{\frac{k_B T_e}{M_i}}$ is

5993 m/s, so from equation (47), K_i becomes $3.82 \times 10^{-10} \text{ cm}^3 \text{ s}^{-1}$.

With all these assumptions, we turn our attention to equation (44) for calculating the etch rate of diamond in a pure oxygen plasma. Based on our argon sputtering experiences and information given by Chapman [5.19] the sputter rate related term of the equation (44) can be neglected for all practical purposes. Usually the sputter yield factor γ_i for carbon is negligibly small producing a carbon sputter rate in the order of 3% of the RIE rate or lower. Therefore, the equation (44) is modified to:

$$E_V = \left[\frac{n_o'}{n_C} \right] \left[\frac{1}{\frac{1}{K_d + Y_i K_i n_{iS}} + \frac{1}{K_d n_{OS}}} \right] \quad (58)$$

Using equation (57), the etch rate of diamond in an oxygen plasma can be finally calculated as $\sim 10.8 \mu\text{m/hr}$.

Experimentally an etch rate of 6-8 $\mu\text{m/hr}$ on a black-film-less 100 mm diameter wafer is achieved under the similar plasma conditions for which the etch rate is calculated. It is important to remember that the etch rate varies from sample to sample. Also the diamond wafers are polycrystalline and since the number of the surface atoms per m^2 varies with the crystal plane. Hence, considering the various assumptions, an average etch rate of 6-8 $\mu\text{m/hr}$ over a 100 mm wafer is actually quite a close agreement to the predicted value.

Chapter VI. Uniformity of Etching and Control of Etch Profile

In chapter 5, based on micrometer measurements we noticed that etching with mixing modes yielded better uniformity than etching in any single mode on a 100 mm diameter diamond wafer. This chapter attempts to explain this interesting experimental observation with theoretical reasoning and simulation. Since our reactor MPDR 325i, is a microwave resonant cavity, the spatial distribution of electric and magnetic fields, also called modal patterns, influences the spatial distribution of the charged species in the generation region. In section 6.1, mathematical expressions relating different possible spatial patterns for different microwave resonant modes for a free-space cylindrical cavity are derived.

The profile of the diffused charged species distribution in the downstream distance follows from the solution of the ambipolar diffusion equations. The ambipolar diffusion equations model the simultaneous motion of the ions and electrons in the discharge and this is reviewed in section 6.2. If the species in the generation zone are assumed to have a spatially uniform species density distribution, then the downstream species density distribution can be obtained by analytically solving the ambipolar diffusion equation. This analytical solution given in equation (50), shows that the species density takes a Bessel function variation along the radial distance and an exponential decay along the downstream distance. The assumption of spatially uniform species density in the generation zone is simple and useful in terms of getting an initial understanding of the species distribution, but it needs to be modified to model the real discharge more accurately. In section 6.3, a radially varying species density is assumed in the generation region. To solve for the downstream species density the differential equation describing the diffusion phenomenon are translated into appropriate difference equations. The numerical technique to solve

these difference equations is also discussed in this section.

In section 6.4, the MATLAB generated plots are presented and discussed. These plots show that sequential etching using different modes can indeed achieve higher etch uniformity. The actual MATLAB programs are attached in Appendix C. At the end of this section, the idea of mixing modes is briefly extended to explore the possibility of controlling the etch rate profile in order to achieve a desired final surface specification for a given sample.

6.1 Derivation of the Modal Patterns

The species generation in an ECR reactor is mainly confined to a three dimensional volume with cusps which for a 2.45 GHz microwave etching system, is determined by the location of 875 Gauss lines generated by the externally impressed static magnetic fields. This zone is also known as the ECR zone and for the MPDR 325i exists about 1 cm inside the discharge [3.4] from the circumference of the confining bell-jar.

To study the uniformity in etching with an ECR reactor, the distribution of the species in the bell jar would ideally be experimentally measured. However, in this work, we have not measured the spatially varying ion densities for different modes. In a microwave ECR cylindrical reactor like ours, the generation of species at the ECR regions depends on the strength of the cavity \vec{E} field and its orientation relative to the external magnetic field. The cavity fields are dependent on the selection of the individual mode by the choice of appropriate cavity height. The spatial variation of the \vec{E} and \vec{H} field structures inside a free-space cylindrical cavity can be theoretically derived by solving the Helmholtz's wave equation. Although these solutions for an empty cavity will change in presence of the

dielectric materials, or plasma, the solutions are still useful as a guideline. Solving the Helmholtz's equation in a plasma-filled cavity is a much more complicated task.

Figure 6.1 shows a free-space cylindrical cavity of radius a and length c for which the modal patterns for TE and TM modes are derived in the following subsection. The details of this derivation may be obtained from [6.1, 6.2].

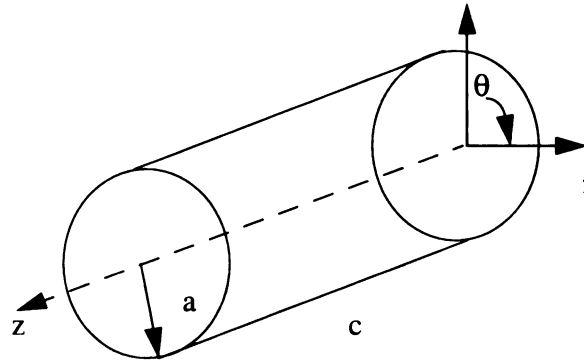


Figure 6.1: Cylindrical cavity of length c and radius a

6.1.1 TE modes

For the derivation of the modal patterns for TE modes, we first consider an electromagnetic vector quantity called the magnetic Hertz potential. The definition of the magnetic Hertz potential may be obtained from [6.3]. The magnetic Hertz potential $\vec{\pi}_h$ satisfies the Helmholtz's wave equation. To find the expressions describing \vec{E} and \vec{H} fields for a certain TE mode in a cylindrical cavity configuration, Helmholtz's wave equation is first solved for magnetic Hertz potential. The Hertz potential is then manipulated to obtain expressions for the \vec{E} and \vec{H} fields in an empty cylindrical cavity.

We assume that the axis of the cylinder shown in Figure 6.1, is aligned along the z-axis and that the magnetic Hertz potential exists only along this direction. Then $\vec{\pi}_h$ can be written as $\vec{\pi}_h = \hat{z}\pi_h$, where $\pi_h(r, \theta, z)$ is a spatially varying scalar quantity representing the magnitude of the magnetic Hertz potential.

The Helmholtz's wave equation can be expressed in terms of the magnitude of the magnetic Hertz potential, as equation (59).

$$\nabla^2\pi_h + k^2\pi_h = 0 \quad (59)$$

In the cylindrical co-ordinate system, equation (59) modifies to equation (60):

$$\frac{1}{r}\frac{\partial}{\partial r}\left(r\frac{\partial\pi_h}{\partial r}\right) + \frac{1}{r^2}\frac{\partial^2\pi_h}{\partial\theta^2} + \frac{\partial^2\pi_h}{\partial z^2} + k^2\pi_h = 0 \quad (60)$$

Solution of equation (60) provides the spatial variation of π_h . Once equation (60) is solved, the expression for π_h is used to find the expressions for \vec{E} and \vec{H} fields. The relation between π_h and the \vec{E} , and \vec{H} fields can be obtained from equation (61) and (62).

These relations are directly derived from the definition of the magnetic Hertz potential

$$\vec{E} = j\omega\mu\nabla\times\vec{\pi}_h = j\omega\mu\left(-\hat{r}\frac{1}{r}\frac{\partial\pi_h}{\partial\theta} + \hat{\theta}\frac{\partial\pi_h}{\partial r}\right) = \hat{r}E_r + \hat{\theta}E_\theta \quad (61)$$

$$\vec{H} = k^2\vec{\pi}_h + \nabla(\nabla\bullet\vec{\pi}_h) = \hat{r}\frac{\partial^2\pi_h}{\partial r\partial z} + \hat{\theta}\frac{1}{r}\frac{\partial^2\pi_h}{\partial\theta\partial z} + \hat{z}\left(k^2\pi_h + \frac{\partial^2\pi_h}{\partial z^2}\right) = \hat{r}H_r + \hat{\theta}H_\theta + \hat{z}H_z \quad (62)$$

where ω and μ in equation (61) and (62), represent the excitation frequency and the permeability of the cavity. To obtain the expression for $\vec{\pi}_h$ by solving equation (60), we

further assume that no mutual interactions exist between the directional components of π_h . Therefore the method of separation of variables is applied and π_h is written as:

$$\pi_h = R(r)\Theta(\theta)Z(z) \quad (63)$$

where R , Θ and Z are only dependent on radial distance r , angular measure θ , and axial distance z . Combining the equation (60) and (63) we get the following equation,

$$\frac{1}{rR}\frac{\partial}{\partial r}\left(r\frac{\partial R}{\partial r}\right) + \frac{1}{r^2\Theta}\frac{\partial^2\Theta}{\partial\theta^2} + \frac{1}{Z}\frac{\partial^2\pi_h}{\partial z^2} + k^2 = 0 \quad (64)$$

An introduction of a new constant k_z simplifies the equation (64) by splitting it into two simple differential equations of known forms.

$$\frac{1}{rR}\frac{\partial}{\partial r}\left(r\frac{\partial R}{\partial r}\right) + \frac{1}{r^2\Theta}\frac{\partial^2\Theta}{\partial\theta^2} + k^2 = \frac{-1}{Z}\frac{\partial^2\pi_h}{\partial z^2} = k_z^2 \quad (65)$$

The right part of equation (65) describes the simple harmonic oscillator which is rewritten below as

$$\frac{\partial^2\pi_h}{\partial z^2} + k_z^2 z = 0 \quad (66)$$

The solution of equation (66) is well known and takes a form:

$$Z(z) = A_0 \cos k_z z + B_0 \sin k_z z \quad (67)$$

where A_0 , and B_0 are two z -independent quantities. The remaining part of the equation (65) is written as equation (68) which can be further simplified by defining a new constant k_θ .

$$\frac{1}{rR}\frac{\partial}{\partial r}\left(r\frac{\partial R}{\partial r}\right) + \left(\frac{1}{r^2\Theta}\frac{\partial^2\Theta}{\partial\theta^2}\right) + (k^2 - k_z^2) = 0 \quad (68)$$

Introducing k_θ and grouping the terms properly we again obtain a solution which has two parts.

$$\frac{r}{R}\frac{\partial}{\partial r}\left(r\frac{\partial R}{\partial r}\right) + (k^2 - k_z^2)r^2 = -\frac{1}{\Theta}\frac{\partial^2\Theta}{\partial\theta^2} = k_\theta^2 \quad (69)$$

The right part describes the angular dependence and the left part describes the radial dependence of π_n . The right part takes the simple harmonic oscillator form as described before in equation (66) giving

$$\frac{\partial^2\Theta}{\partial\theta^2} + k_\theta^2\Theta = 0 \quad (70)$$

Equation (70) has the solution as:

$$\Theta(\theta) = A_1 \cos k_\theta\theta + B_1 \sin k_\theta\theta \quad (71)$$

where A_1 and B_1 are constants with respect to θ . Since rotational symmetry exists in cylindrical cavity, a condition $\Theta(\theta) = \Theta(\theta + 2n\pi)$ has to be satisfied by equation (71) which produces $k_\theta = n$. Therefore, the remaining part of the differential equation in equation (69) becomes:

$$\frac{r}{R}\frac{\partial}{\partial r}\left(r\frac{\partial R}{\partial r}\right) + (k^2 - k_z^2)r^2 = n^2 \quad (72)$$

Equation (72) is rearranged and equation (73) is obtained.

$$\frac{\partial^2 R}{\partial r^2} + \frac{1}{r}\frac{\partial R}{\partial r} + \left[(k^2 - k_z^2) - \frac{n^2}{r^2}\right]R = 0 \quad (73)$$

The form of equation (73) has a well known solution which is expressed as a combination of Bessel and Hankel function of order n given by

$$R(r) = A_2 J_n(k_r r) + B_2 Y_n(k_r r) \quad (74)$$

where

$$k_r = \sqrt{(k^2 - k_z^2)} \quad (75)$$

Equation (74) is now simplified again using the property of Hankel functions. Since the value of zero order Hankel function $Y_0(0)$ is infinite at $r=0$, B_2 in equation (74) has to be zero. Thus the final radial dependence of magnetic Hertz potential becomes:

$$R(r) = A_2 J_n(k_r r) \quad (76)$$

Combining Z , Θ and R from equation (67), (71) and (76) we construct the full expression for the magnetic Hertz potential using equation (63) which is given below.

$$\pi_h(r, \theta, z) = R\Theta Z = A_2 J_n(k_r r) (A_1 \cos n\theta + B_1 \sin n\theta) (A_o \cos k_z z + B_o \sin k_z z) \quad (77)$$

Equation (77) can be further simplified using boundary conditions. The tangential component of the \vec{E} goes to zero at the metallic cavity boundary which is expressed in the following equation

$$\hat{n} \times \vec{E}|_{metal} = 0 \quad (78)$$

where \hat{n} is the unit normal vector to the surface. If equation (78) is applied to equation

(61) at $r=a$, we get, $k_r = \frac{x_{nm}'}{a}$ where, x_{nm}' is the m^{th} zero of the first derivative of the n^{th}

order Bessel function, shown as $J_n'(x_m) = \frac{\partial}{\partial x} [J_n(x_m)] = 0$. Similarly, if equation (78)

is applied to equation (61) at $z=0$ and $z=C$, we get $Z(z) = B_o \sin(k_z z)$ and $k_z = \frac{l\pi}{c}$ where

l is any positive integer. Finally, the simplified expression for the magnetic Hertz potential becomes:

$$\pi_h(r, \theta, z) = AJ_n\left(\frac{x_{nm}'}{a}r\right)(A_1 \cos n\theta + B_1 \sin n\theta)\left(\sin \frac{l\pi}{c}z\right) \quad (79)$$

The above expression is true for any arbitrary mode TE_{nml} where, the subscripts n , m , and l , denote the θ , r , and z variation respectively. The arbitrary constants A , A_1 , B_1 are the related to the microwave power input and the reactor characteristics.

However, for a given cavity dimension, not all operating frequencies can excite a TE mode and the expression for an appropriate resonant frequency is obtained from equation (75). Since $k = \omega\sqrt{\mu\epsilon}$ is always true for a wave of frequency ω that travels through a medium with permeability μ and permittivity ϵ , equation (75) is rewritten as equation (80).

$$k^2 = k_r^2 + k_z^2 = \left(\frac{x_{nm}'}{a}\right)^2 + \left(\frac{l\pi}{c}\right)^2 = \omega^2 \mu\epsilon \quad (80)$$

Rearranging equation (80) we get,

$$f_{TE_{nml}} = \frac{v_c}{2\pi} \sqrt{\left(\frac{x_{nm}'}{a}\right)^2 + \left(\frac{l\pi}{c}\right)^2} \quad (81)$$

where v_c is the velocity of light in free space and $f_{TE_{nml}}$ is the resonant frequency. It is important to note here that for a given input frequency, different TE modes can be excited in the cavity by changing either the length c or the radius a . For our cavity, the length c is flexible and can be adjusted by changing the sliding short position.

Finally, the expressions for the \vec{E} and \vec{H} fields for TE_{nml} modes are developed using

equation (79), (61), and (62). The derivation is straight forward and hence is not shown here. However, the final expressions for the r and θ component of \vec{E} field e.g, E_r , E_θ and r, θ , z components of \vec{H} fields, e.g, H_r , H_θ and H_z are listed below.

$$E_r = -j\omega\mu n \left(\frac{1}{r}\right) A J_n \left(\frac{x_{nm}'}{a} r\right) (A_1 \sin n\theta - B_1 \cos n\theta) \left(\sin \frac{l\pi}{c} z\right) \quad (82)$$

$$E_\theta = j\omega\mu \left(\frac{x_{nm}'}{a}\right) A J_n' \left(\frac{x_{nm}'}{a} r\right) (A_1 \cos n\theta + B_1 \sin n\theta) \left(\sin \frac{l\pi}{c} z\right) \quad (83)$$

$$H_r = \left(\frac{l\pi}{c}\right) \left(\frac{x_{nm}'}{a}\right) A J_n' \left(\frac{x_{nm}'}{a} r\right) (A_1 \cos n\theta + B_1 \sin n\theta) \left(\cos \frac{l\pi}{c} z\right) \quad (84)$$

$$H_\theta = -\left(\frac{l\pi}{c}\right) \left(\frac{1}{r}\right) A n J_n \left(\frac{x_{nm}'}{a} r\right) (A_1 \sin n\theta - B_1 \cos n\theta) \left(\cos \frac{l\pi}{c} z\right) \quad (85)$$

$$H_z = \left(k^2 - \left(\frac{l\pi}{c}\right)^2\right) A J_n \left(\frac{x_{nm}'}{a} r\right) (A_1 \cos n\theta + B_1 \sin n\theta) \left(\sin \frac{l\pi}{c} z\right) \quad (86)$$

Note that for TE modes, \vec{E} field does not have an axial or z component. Similarly, for transverse magnetic fields or TM modes, we expect to find no component of the magnetic field along the z-direction and expect the \vec{E} field to have components in all directions. In the next part, we discuss how the above approach is extended for solving the TM modes.

6.1.2 TM modes

For TM modes, the same Helmholtz's wave equation is solved in cylindrical co-ordinate but for the electric Hertz potential $\vec{\pi}_e$. Similar to magnetic Hertz potential, electric Hertz potential is also an electromagnetic vector quantity. We again consider that the direction of electric Hertz potential is aligned to the z-axis, or the axis of the cylindrical

cavity and $\vec{\pi}_e = \lambda \pi_e$.

With mathematical manipulation as carried out in the last section and with proper application of boundary conditions, an expression for the electric Hertz potential is obtained which is given in equation (87).

$$\pi_e(r, \theta, z) = BJ_n\left(\frac{x_{nm}}{a}r\right)(A_1 \cos n\theta + B_1 \sin n\theta)\left(\cos \frac{l\pi}{c}z\right) \quad (87)$$

Again B, A_1 and B_1 in equation (87) are constants and are related to the input microwave power and the reactor characteristics. As before, the expression for the resonant frequency for the TM modes is developed. Surprisingly this expression, as given in the earlier equation (81), remains the same for both TE and TM modes. The \vec{E} and \vec{H} field components for the TM_{nml} modes are finally expressed in the following five equations.

$$E_r = -\left(\frac{l\pi}{c}\right)\left(\frac{x_{nm}}{a}\right)BJ_n'\left(\frac{x_{nm}}{a}r\right)(A_1 \cos n\theta + B_1 \sin n\theta)\left(\sin \frac{l\pi}{c}z\right) \quad (88)$$

$$E_\theta = -\left(\frac{l\pi}{c}\right)\left(\frac{1}{r}\right)BnJ_n\left(\frac{x_{nm}}{a}r\right)(A_1 \sin n\theta - B_1 \cos n\theta)\left(\sin \frac{l\pi}{c}z\right) \quad (89)$$

$$E_z = \left(k^2 - \left(\frac{l\pi}{c}\right)^2\right)BJ_n\left(\frac{x_{nm}}{a}r\right)(A_1 \cos n\theta + B_1 \sin n\theta)\left(\cos \frac{l\pi}{c}z\right) \quad (90)$$

$$H_r = -j\omega\epsilon n\left(\frac{1}{r}\right)BJ_n\left(\frac{x_{nm}}{a}r\right)(A_1 \sin n\theta - B_1 \cos n\theta)\left(\cos \frac{l\pi}{c}z\right) \quad (91)$$

$$H_\theta = -j\omega\epsilon\left(\frac{x_{nm}}{a}\right)BJ_n'\left(\frac{x_{nm}}{a}r\right)(A_1 \cos n\theta + B_1 \sin n\theta)\left(\cos \frac{l\pi}{c}z\right) \quad (92)$$

Here, x_{nm} represents the m^{th} zero of the n^{th} order bessel function, $J_n(x)$.

Equations (82) through (86) for TE_{nml} and equation (88) through (92) for TM_{nml} can

be used to plot the variation of \vec{E} and \vec{H} fields in a cavity as a function of r and θ . Usually the z component variation is not plotted since the z -dependence is periodic (sinusoidal). Plots of various modal patterns are available in references [6.4], and several of them are shown in Figure 6.2. Obviously some modal patterns seen at $z=0$, show a great deal of radial variations.

At relatively low pressures, where the ECR mechanism is primarily responsible for species generation, the plasma density variation from mode to mode will be mainly due to the different generation rates at the ECR zones. As described earlier, the ECR mechanism is due to the interaction of the external magnetic field with the perpendicular component of the microwave electric field. This will clearly be different from mode to mode, resulting in different modes having different numbers of ECR excitation zones and different generation rates. The generated species will diffuse away from the excitation zones creating different species density distribution in space for different modes. This is described in the following sections.

At higher pressures, on the order of 100 mtorr and above, species generation due to Joule heating becomes appreciable. For such cases, the plasma tends to visually represent the field patterns shown in Figure 6.2. For example, at higher pressures the TE_{211} mode shows four bright plasma regions corresponding to the four electric field lobe patterns for that mode. The TM_{011} mode shows a bright plasma located in the center. In this work, however, our attention was limited to low pressures and ECR plasmas.

6.2 Ambipolar Diffusion

Ambipolar diffusion, or Schottky diffusion, assumes that the mean free path for the

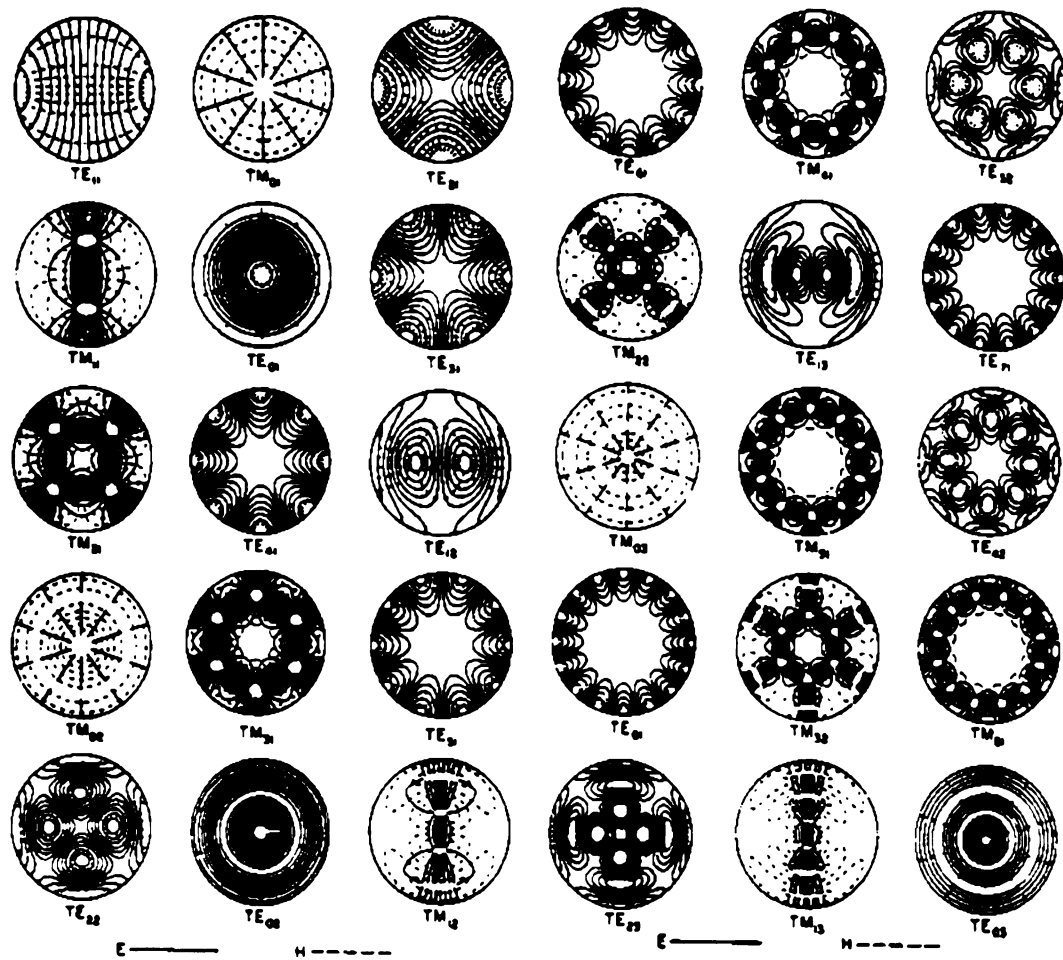


Figure 6.2: Modal patterns for TE and TM modes

carriers is much smaller than the discharge volume. Since electrons move much faster than the ions, a space charge electric field is established which accelerates the ions but slows down the electrons. As a result, under steady state conditions, both electrons and ions diffuse with the same diffusion coefficient D_a , which is known as ambipolar or Schottky diffusion coefficient.

Considering an infinitesimal volume of discharge with a non-zero space-charge electric field \vec{E} , the flux of ions Γ_i and electrons Γ_e going out of the discharge boundary can be written as:

$$\Gamma_i = -n_i\mu_i\vec{E} - D_i\nabla n_i \quad (93)$$

$$\Gamma_e = n_e\mu_e\vec{E} - D_e\nabla n_e \quad (94)$$

where n , μ and D in the above equations denote the charged species density, mobility and the diffusion constants for the species. The subscript i , and e refer to ions and electrons respectively. The mobility and the diffusion constants for both ions and electrons are related to plasma characteristics e.g, the temperature of electrons and ions, T_e , T_i and the collisional frequency for momentum transfer, ν_{im} , and ν_{em} . These relations are shown in equation (95) through (98).

$$\mu_i = \frac{e}{M_i\nu_{im}} \quad (95)$$

$$\mu_e = \frac{e}{m_e\nu_{em}} \quad (96)$$

$$D_i = \frac{kT_i}{M_i\nu_{im}} \quad (97)$$

$$D_e = \frac{kT_e}{m_e v_{em}} \quad (98)$$

where m_e and M_i in the above equations represent the mass of electrons and ions respectively.

Because, the plasma is quasi-neutral, we can assume $n_e = n_i = n$. Further, under steady state conditions, the macroscopic densities of the ions and electrons in a small volume remain constant which implies that the flux of ions equals the flux of electrons across the boundary of the small volume considered. Therefore, we can also assume

$\Gamma_i = \Gamma_e = \Gamma$. Applying these two conditions to equations (93) and (94), one can show that

$$\Gamma = -D_a \nabla n \quad (99)$$

where

$$D_a = \frac{\mu_i D_e + \mu_e D_i}{\mu_i + \mu_e} \quad (100)$$

This simply indicates that under steady state conditions, the electrons and ions diffuse together and the effective ambipolar diffusion constant is D_a . Moreover, the transient condition for the charge flow through a small volume has to satisfy the continuity equation which is given as:

$$\frac{\partial n}{\partial t} - \nu_i n + \nabla \cdot \Gamma = 0 \quad (101)$$

where ν_i is the ionization frequency. Combining equation (99) and (101) we get:

$$\frac{\partial n}{\partial t} - \nu_i n + D_a \nabla^2 n = 0 \quad (102)$$

Under steady state condition, equation (102) can be rearranged as:

$$\nabla^2 n - \frac{v_i}{D_a} n = 0 \quad (103)$$

Equation (103) is the key equation for modelling the transport of the species inside the discharge. Note that the density of the species n is a function of spatial co-ordinates and is assumed to be spatially non-uniform at the edge of the generation region corresponding to $z=0$. For a cylindrical co-ordinate system, the equation (103) can be written as:

$$\frac{1}{r} \frac{\partial}{\partial r} \left(r \frac{\partial n}{\partial r} \right) + \frac{1}{r^2} \frac{\partial^2 n}{\partial \theta^2} + \frac{\partial^2 n}{\partial z^2} + \left(\frac{v_i}{D_a} \right) n = 0 \quad (104)$$

To make the problem less complicated we assume that the species density does not vary with θ . Therefore, equation (105) changes to:

$$\frac{\partial^2 n}{\partial r^2} + \frac{1}{r} \frac{\partial n}{\partial r} + \frac{\partial^2 n}{\partial z^2} + \left(\frac{v_i}{D_a} \right) n = 0 \quad (105)$$

The term $\left(\frac{v_i}{D_a} \right) n$ in the above equation, represents the effective generation of carriers per unit volume in the bulk plasma. Usually this term is very small for the low pressure discharge, and may be neglected to a first approximation.

6.3 Formulation of the Numerical Problem

Since angular symmetry is assumed in the model, the actual three-dimensional discharge is simplified to a two-dimensional cross section taken along the r - z plane. Moreover, the radial variation of the species density from the center to the discharge circumference is symmetrical about its axis, hence, it is sufficient to consider only half the

discharge, extended from the center to the periphery. Figure 6.3 represents the modeled structure of the discharge.

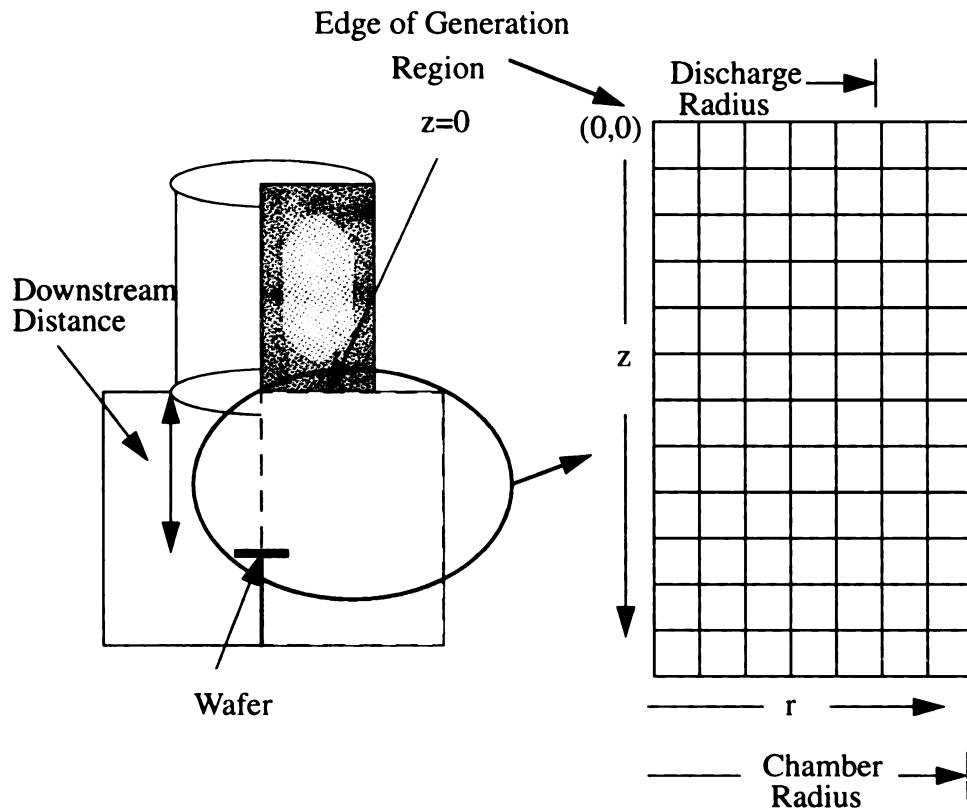


Figure 6.3: The cross-section of plasma discharge

A uniform numerical grid is established for the entire diffusion region, in which the species densities at discrete locations are represented by individual grid points.

A part of the grid is enlarged and shown in Figure 6.4. The numerical solution is carried out using the finite difference method [6.5] and MATLAB software [6.6]. $n(i,j)$ in Figure 6.4 represents the species density at the grid location (i,j) . The ambipolar diffusion equation shown in (105) is translated into a difference equation using the notation described in Figure 6.4.

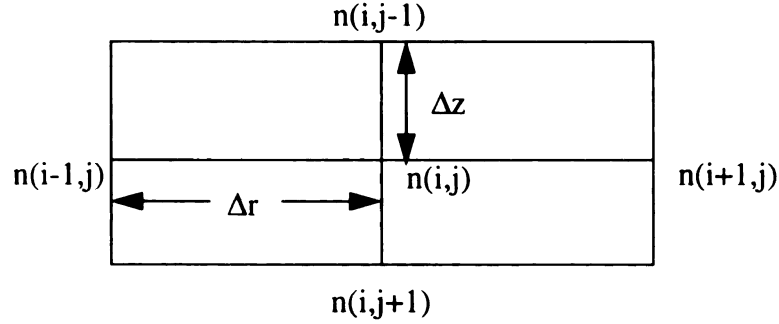


Figure 6.4: The numerical grid

The important steps showing the trend of the derivations are shown below.

$$\frac{\partial^2 n}{\partial r^2} = \frac{\partial}{\partial r} \left(\frac{\partial n}{\partial r} \right) = \frac{\frac{n(i+1, j) - n(i, j)}{\Delta r} - \frac{n(i, j) - n(i-1, j)}{\Delta r}}{\Delta r} \quad (106)$$

$$\frac{\partial^2 n}{\partial z^2} = \frac{\partial}{\partial z} \left(\frac{\partial n}{\partial z} \right) = \frac{\frac{n(i, j+1) - n(i, j)}{\Delta z} - \frac{n(i, j) - n(i, j-1)}{\Delta z}}{\Delta z} \quad (107)$$

$$\frac{1}{r} \frac{\partial n}{\partial r} = \frac{1}{i(\Delta r)} \left[\frac{n(i+1, j) - n(i-1, j)}{2\Delta r} \right] \quad (108)$$

The above equations, combined with equation (105) gives the final expression for the species density at the location (i,j) in terms of its neighbor locations:

$$n(i, j) = \frac{\left(\frac{n(i+1, j) + n(i-1, j)}{(\Delta r)^2} + \frac{n(i, j+1) + n(i, j-1)}{(\Delta z)^2} \right)}{\left[\frac{2}{(\Delta r)^2} + \frac{2}{(\Delta z)^2} + \frac{v_i}{D_a} \right]} \quad (109)$$

Equation (109) is the difference equation which has been numerically solved for the appropriate boundary conditions. The discharge has four boundaries, hence four boundary conditions are needed to solve the set of equations shown in equation (109). The cavity periphery is metallic, hence the density of ions and electrons becomes zero along the boundaries. Therefore n at $r=a$, and $z=c$ are assumed to be zero. At $z=0$, the spatially

varying density of the generated species serves as one boundary condition. Since the chamber radius is much bigger than the discharge radius, only a part of this boundary has non-zero species density. This is shown in Figure 6.5. The species density goes to zero for the portion of grid that is outside the bell -jar since that corresponds to the top metallic surface of the vacuum chamber. Also by symmetry $\left. \frac{\partial n}{\partial r} \right|_{r=0}$ may be assumed. The Figure 6.5 shows two regions.

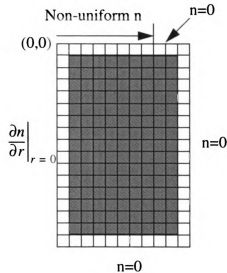


Figure 6.5: Region of solution and boundary conditions

The shaded region is where the iterative search for the correct solution continues and the clear region represents the fixed valued boundaries. After every iteration the new density at each physical location namely, each matrix element is compared with its old value. The maximum and the total difference between the old and the new density in the whole shaded matrix is calculated after each iteration. When both these differences reach below a pre-determined value, an acceptable accuracy level is ensured and the iteration is stopped.

6.4 Discussion of the Numerical Solution

For testing purpose, the numerical solution was first carried out with an uniform species density at $z=0$. The plot of the downstream species density obtained from the numerical solution matched well with the plot obtained from the analytical solution given by equation (50). Then the simulation was carried out for two different non-uniform hypothetical species distribution at the source region. The results of the simulations are shown in Figure 6.6 and 6.7. Usually the species density in the ECR reactor increases from the center to the periphery since the actual ECR zone, i.e, the 875 Gauss line region exists closer to the periphery. Therefore two species distributions are chosen both of which show an increase in species density along the radial distance but distribution 1 shows a larger radial variation than distribution 2. For the purpose of this discussion, the two different distributions are referred to as different modes. Although they do not necessarily correspond to any two specific modes discussed in section 6.2, they represent in a qualitative way how species variations may change as modes and pressures are changed.

The species densities at various locations are normalized and plotted in Figure 6.6 and 6.7. The downstream distance for mode 1 and mode 2 were chosen to be 2.5 cm and 10 cm respectively. Since the profile at the downstream distance for mode 1 shows a radial increase in species density, etching in mode 1 will result in removal of more material from the periphery than from the center. However, mode 2 will show an opposite effect. Hence, if appropriate amount of etching is performed with mode 1 and mode 2 sequentially, the total removal at the end of combined etching may be very uniform along the radius. This is shown in figure 6.8. The percent variation in etch rate for mode 1 is 23.6%, for mode 2

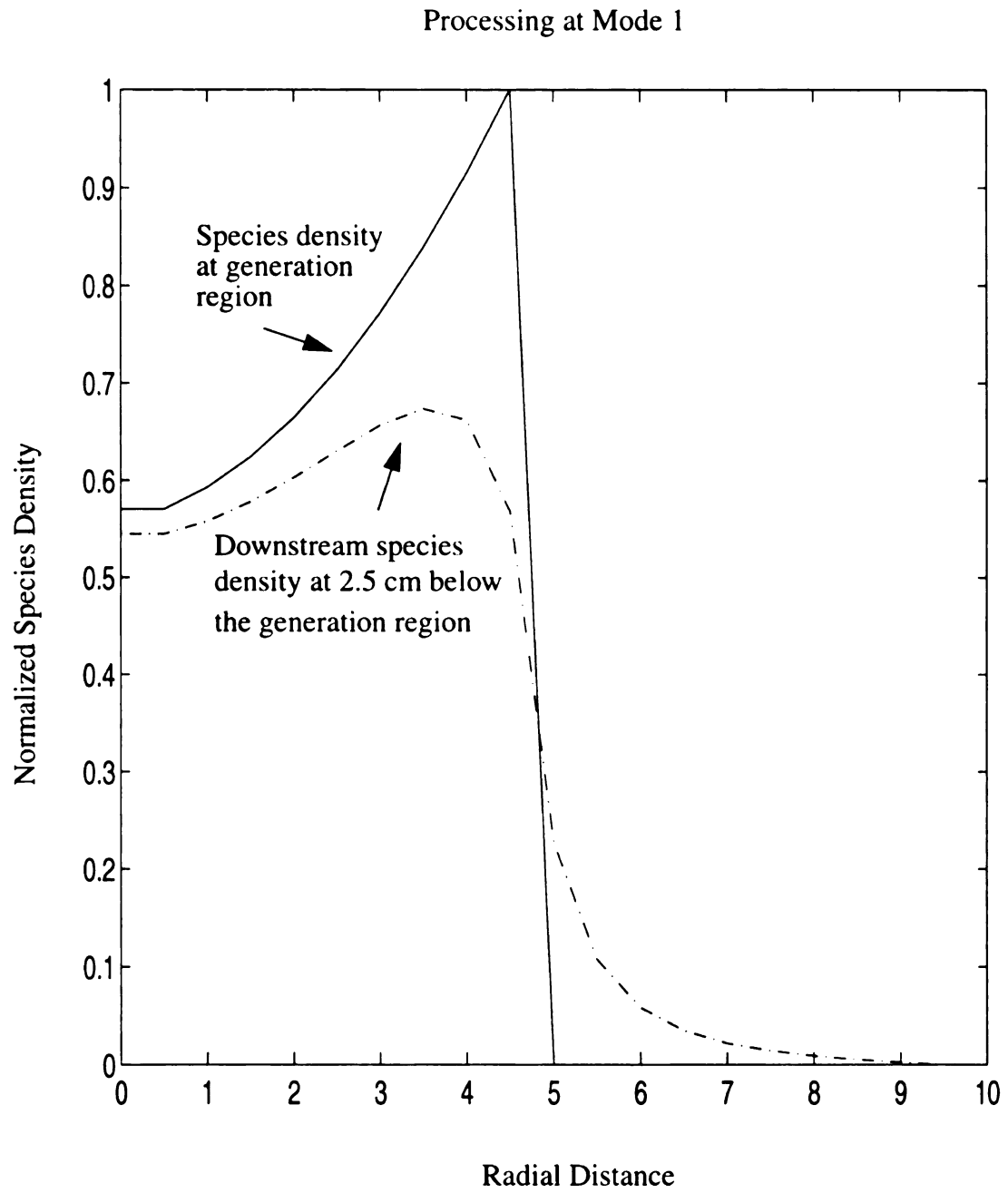


Figure 6.6: Normalized downstream species density variation for mode 1

Processing at Mode 2

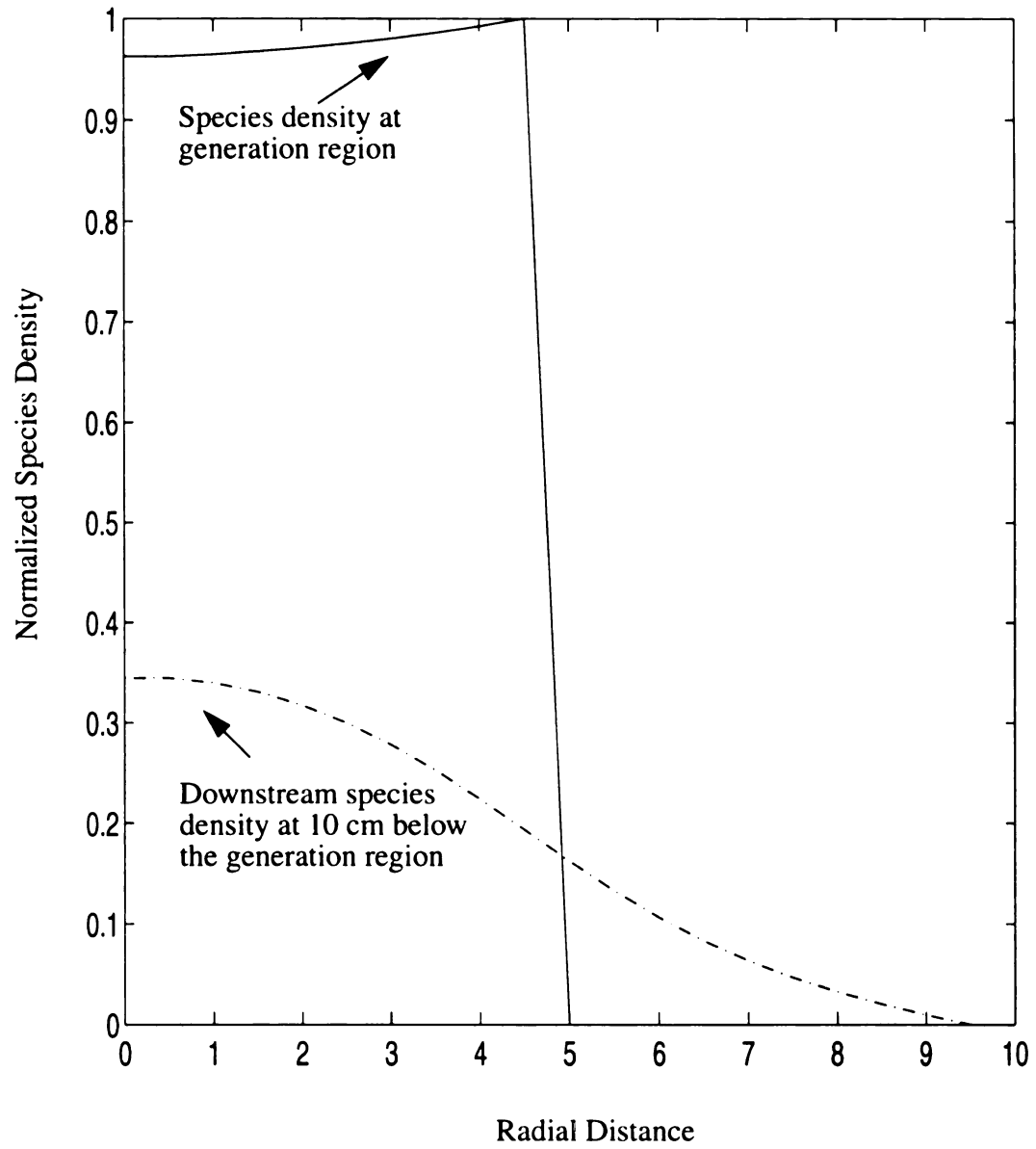


Figure 6.7: Normalized downstream species density variation for mode 2

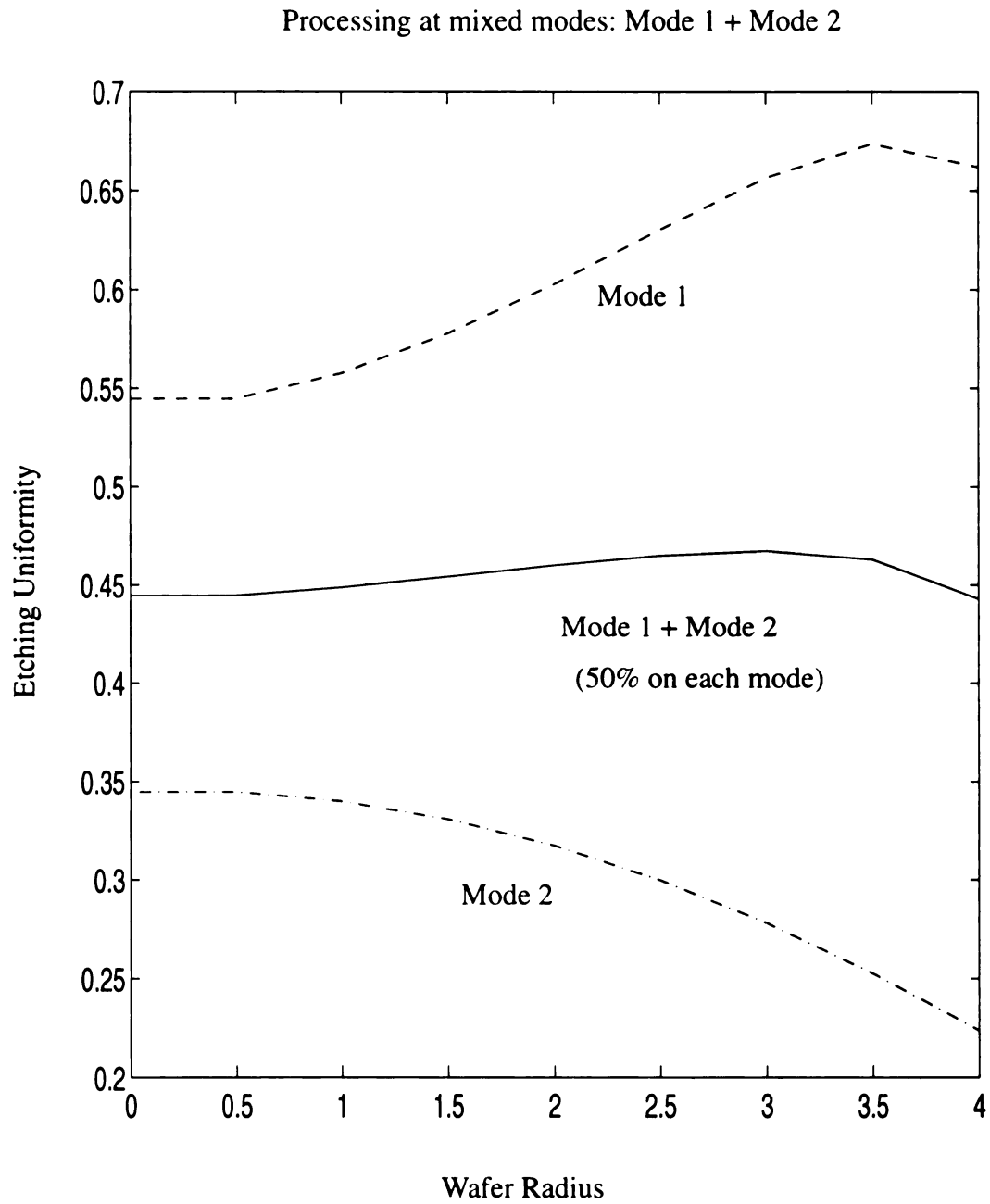


Figure 6.8: Etching uniformity comparison for mode 1, mode 2 and mixed modes

is 34.7%, and the mixed modes is 2.9%. For this example, the etching was assumed to be done for equal amount of time in each mode. These calculations are done over a 100 mm radius wafer. For achieving even higher uniformity, relative run times may be optimized. Also more modes may be introduced for etching. However, from this discussion it is seen, that the etching in mixed modes can result in higher uniformity than etching in any one mode. It may be noted that initial experiments in chapter 5 supported this hypothesis.

As an extension of this concept, the method of mixing modes may be found useful for further controlling the etch profiles as desired. For examples, the wafers may be preferentially etched with intention to make a non-uniform wafer, uniform or to achieve a final desired thickness variation for a wafer. In fact, for the CVD grown free-standing polycrystalline diamond wafers, the as-grown wafers are often of non-uniform thickness and therefore require non-uniform removal of material to create a final structure of uniform thickness.

Chapter VII. Planarization and Masking Of Diamond Films

7.1 Planarization

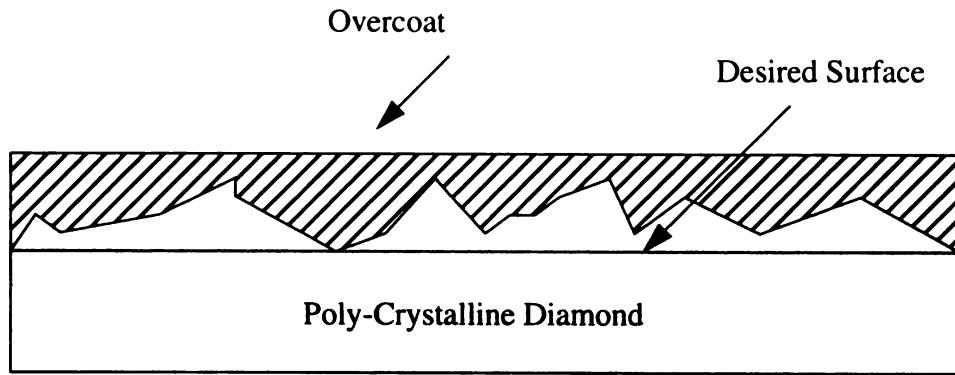
Reduction of surface roughness on an as-grown polycrystalline diamond film is a well-known problem in diamond research. Many different methods are proposed in the literature for planarizing rough films, some of which are already reviewed in detail in chapter 2. However, before going into the description of the polishing techniques, it is useful to briefly introduce different measures of surface roughness that are commonly used in characterizing a rough diamond surface [7.1]. R_a , R_{max} , and R_z are three of such measures. R_a is known as the mean roughness of a surface and is defined by equation 110.

$$R_a = \frac{1}{L_x L_y} \int_0^{L_x} \int_0^{L_y} |f(x, y)| dx dy \quad (110)$$

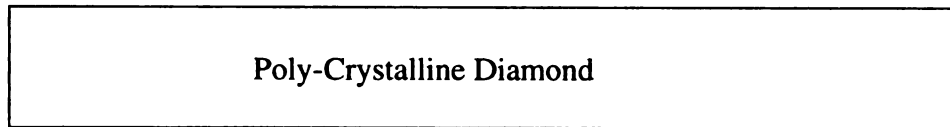
$f(x,y)$ in the above equation is the surface height relative to the center plane and L_x and L_y are the dimensions of the surface. R_{max} is defined as the difference in the height between the highest and lowest points on the surface relative to the mean plane, and R_z is the average difference in the five highest peaks and five lowest valleys relative to the mean plane.

In general, different diamond polishing methods vary in their efficiency and often the initial roughness of the film plays a critical role in determining the success of a method. Some polishing techniques work better for the gross reduction of roughness, say for films with beginning $R_a \sim 10 \mu\text{m}$, and some others work better for finer polishing, say for $\sim 0.5 \mu\text{m}$ of beginning R_a .

In this section, we focus on results from the planarization technique using a sacrificial planar coating. This process is described in Figure 7.1. The idea of first coating the rough



1. After spinning on the sacrificial layer



2. After etch back using ECR plasma

Figure 7.1: Method of polishing diamond

diamond surface with a planarized layer, and then etching both the diamond and the coated layer at the same rate to obtain a flat diamond surface at the end, has been investigated by several researchers [7.2, 7.3, 7.4, 7.5]. However, the methods differed in the planarizing material and the technique used to coat the diamond surface. Also different etching mechanisms and etching apparatus have been reported by different researchers. Our planarization technique was restricted mainly to the investigation of different spin-on-materials as the sacrificial layer.

A Wavemat 325i ECR plasma reactor was used as the etching apparatus for all planarizing experiments. Finding a proper spin-on-material that forms a crack-free, continuous, uniform, and smooth surface on a rough diamond surface and which etches at a low comparable rate as diamond was the first main challenge to face. Once a material was found, the next task was to find the correct plasma etching condition and the time of etching. The etching condition was mainly controlled by changing the gas chemistry. This was similar in concept to controlling the selectivity of etching in conventional semiconductor processing, except that in diamond planarization, a non-selective plasma was generated intentionally to etch both the diamond and the sacrificial layer at the same rate. Since, sputtering by nature is a relatively non-selective etching process, both sputtering and RIE with proper gas mixtures was applied for this purpose.

We have seen in the previous chapter that even plain etching on an uncoated diamond sample increases the surface roughness, hence no over-etching was desired in order to make the method effective. Deciding the etch time was not easy as the surface roughness varied spatially and the height of the over-coat filling the surface peaks and valleys, was necessarily different at different places. For best success, the etch time had to be just

appropriate to etch the maximum height of the spin-on-material without over-etching.

The following sections discuss various planarization results obtained from using different overcoats and ECR plasmas consisting of various mixtures of Ar, O₂, and SF₆.

7.1.1 Planarization with Photoresist on Thick Film Samples

It is well known that photoresist can smooth rough surfaces and Pearton et.al., reported that UV hardened photoresist, Hunt 5209E [7.6] can be used as a masking material for diamond in an oxygen containing plasma [2.41]. Since, a material used as mask has a much lower etch ratio than the masked material, Hunt AZ 5209E was thought to be a potential overcoat for yielding an etch rate at least comparable to that of diamond. The samples treated for polishing experiments with a photoresist overcoat, had an initial R_a between 0.4 and 0.8 microns. These 1 cm X 1cm square shaped samples were arc jet deposited and had a blackish appearance. Initially two samples MSU-1 and MSU-7 affixed in the middle of a 50 mm silicon wafer by graphitic paint, were spin-coated with AZ 5209-E at 4000 rpm for 30 seconds. Then the samples were soft-baked for 30 minutes at 85 °C and UV hardened at 300 watts for 15 minutes using the SUSS MJB 3 mask aligner as the UV source. The thickness of the photoresist layer was measured to be ~ 0.9 μm by an ellipsometer. The samples were then sputtered for half-hour in Argon only plasma. The pre-processing, post-coating and the post-etching dektak profilometer scans showed that some degree of surface planarization was achieved after the photoresist coating, but the roughness after the plasma etching went back to a value close to the pre-processing R_a . These results are given below in Table 7.1.

Table 7.1: Dektak result of photoresist experiments

Sample	Initial R_a Scan (Dektak)	R_a after 6 layer overcoat (Dektak)	50 min Post etching R_a (Dektak)
MSU-7	6213 ± 1412	4718 ± 1034	5812 ± 1405

Another sample, MSU-5 was coated similarly with 5209 E photoresist but was etched with an argon/oxygen plasma for 96 minutes. This caused the post-etch processing R_a to actually increase beyond the initial R_a . Next, experiments were performed that showed that UV hardened photoresist AZ 5209E actually etches much faster (about 8 times) in our system than diamond with an argon & oxygen plasma ECR plasma. The adjustment of the plasma parameters did not seem to affect this etch ratio to a great extent, so it became clear that photoresist was not a good choice for the diamond planarization at least for the plasma chemistry and the photoresist investigated. Therefore the research turned to the investigations of other spin-on-materials.

7.1.2 Planarization with Spin-On-Glass on Thick Film Samples

First, in order to establish the etch rate of SOG, a 3 inch Si wafer was coated with 511 F spin-on-glass [7.7] at 3000 rpm for 30 s, followed by a 30 s bake at 150 °C and 1 hour bake at 420 °C in N₂ atmosphere. The thickness of one SOG layer ranged between 1800 - 3500 angstrom, depending upon the spinning speed. Typically the thickness was found to be around 2000 angstrom from ellipsometer measurements, when spun at 3000 rpm. The etch rate of SOG in an argon only plasma was appreciably lower than photoresist, and was

found closer to diamond. However, as the thickness of the SOG film was grown to more than 4000 Angstroms with multiple layers, the film showed surface scaling at the end of 1 hour heating in 420°C.

However, arc jet deposited samples were coated with SOG and treated in ECR plasmas. MSU-2, received two layers of SOG coating following the technique discussed above and was sputtered in an argon only (20 sccm) plasma. Dektak measurements did not show much improvement in R_a with two layers of SOG coating or at the end of sputter etching. The standard deviation showing the variation of surface roughness from one spatial location to other, increased after the sample was coated with SOG and the higher standard deviation was maintained after etching. Table 7.2 shows the results obtained from Dektak measurements.

Table 7.2: Dektak result of SOG experiments

Sample	Initial R_a Scan (Dektak)	R_a after 6 layer overcoat (Dektak)	50 min Post etching R_a (Dektak)
MSU-2	3287 ± 253	3054 ± 721	2882 ± 667

Since, SOG results did not show much encouraging results with argon sputtering we decided to use titanium silicate-photoresist emulsion for our next set of experiments.

7.1.3 Planarization with Titanium-Silicate on Thick Film Samples

Earlier work on diamond planarization using an argon/oxygen ECR ion beam irradiation with no sacrificial coating was reported to reduce the surface roughness from 3 μm R_{max} to 0.5 μm R_{max} [2.33]. Zhao, Grogan *et al.*, [2.32, 2.34, 2.35] from the University of

Arizona reported to improve the method of ion beam smoothing by coating the rough diamond surface with a layer of titanium silicate mixed in an appropriate proportion of photoresist. Depending upon the initial roughness of the diamond film, often several layers of coatings were applied to make the coated surface smooth to the desired scale. According to the report, the coating was hardened by baking, and etched with an oxygen ion beam of various energy and various incidence angle of the ion beam. The etching was reported to result into a smooth diamond surface with appropriate energy and incident angle.

The ion-beam in their case was derived from a Kaufman ion source and the use of a Faraday cup allowed them to monitor and maintain a constant beam flux. The ability to adjust the incident angle of the beam with respect to the macroscopic surface of the diamond substrate was claimed to be very important in achieving a polished surface and an incident angle of 47° was reported to produce the best polishing result.

We attempted to planarize diamond using the same concept of adding a titanium silicate-photoresist layer on the rough surface of diamond but etching in an ECR plasma reactor MPDR 325i instead of an ECR ion beam apparatus or Kaufman source. The main difference between the MPDR 325i and an ion beam source is that the ion flux from an ECR plasma reactor strikes the surface of the substrate perpendicularly and the incidence angle of the ion flux can not be controlled. Therefore, etching in an ECR plasma reactor is expected to produce different results than what was obtained from ion beam etching at a non-perpendicular angle of incidence.

To carry out the experiments, titanium-silicate was mixed in a 1:1 proportion with both SC1400-17 and SC1400-28 [7.8] photoresists and agitated using ultra-sound waves for 15 minutes following the technique described by Zhao et. al. This mixture was then spun on

different samples which produced an effectively plane surface, supported by the Dektak measurements but the post-etching Dektak measurements for R_a in almost all cases were comparable to the beginning R_a implying no significant final planarization.

Many attempts were successively made for months to equalize the etch rate of titanium silicate with diamond under different plasma conditions but no condition was found to produce a satisfactory result. During one set of Dektak measurements, the short range (0.1 mm) Dektak scans of etched samples were noticed to be less than the R_a from a long range (1 mm) Dektak scans for the coated sample, whereas the R_a measurements for the uncoated sample did not differ much from short range to long range measurements. The results of these scans are presented in Table 7.3 and are thought to be key observations in terms of understanding our post-etching results. From the scans, it seemed to us that the overcoat layer planarizes the samples over short ranges but fails over long ranges.

Table 7.3: Long range Vs. short range dektak results

Sample	Sample Condition	0.1 mm Scan	1 mm scan
MSU-16	Uncoated	3281±521	3944 ± 444
MSU-11	Coated with 6 layers	599±382	1830 ± 820

In other words, the uncoated surface appears to have two kinds of roughness, one results from rapidly changing peaks and valleys and the other is produced from variation of surface topography over several hundreds of micrometers. The Dektak profilometer picked up both these types of roughness while tracing the surface. We think that the planarization coating successfully reduces the short-range roughness, although it follows the

long range topography variation of the surface. This is better explained in Figure 7.2.

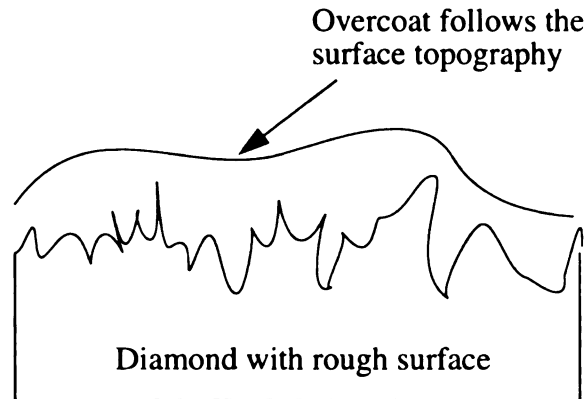


Figure 7.2: Short and long range surface fluctuations

Since the planarization occurs only in short ranges upon coating, it is believed that at the end of etching the surface roughness for small regions are reduced although the long range roughness remains unaffected. A typical result based on 0.1 mm Dektak scan is shown in the Table 7.4 below.

Table 7.4: Dektak result of titanium silicate experiments

Sample	Initial R_a Scan (Dektak)	R_a after 6 layer overcoat (Dektak)	50 min Post etching R_a (Dektak)
MSU-14	3406 ± 442	432 ± 231	2135 ± 821

Another interesting phenomenon was observed which was not reported by Zhao et.al., [2.32, 2.34, 2.35]. Titanium silicate appeared to exhibit a two-phase etching process. In all cases the photoresist was etched away at a very high rate leaving behind numerous small dot-like particles on the diamond surface. This remaining material appeared to be

relatively etch-resistant. We believe that the photoresist served as the carrier for the suspended titanium silicate particles which deposit on the surface of the diamond as the photoresist is etched away by the oxygen plasma.

At this point a new set of planarizing experiments were planned with spin-on-glass (SOG). This was motivated by an observation made on an SEM of SOG coated sample used in the masking work reported later in section 7.2. Since the arc-jet deposited diamond thick films appeared to have prominent long range surface variations compared to the microwave grown thin film samples, we chose to carry out our experiments with the microwave CVD grown diamond films. These are thin films grown on silicon substrate which have grain sizes not more than about 1-2 μm .

Since this time our interests were more concentrated in seeing the effect of our planarizing technique on small areas (say $\sim 50 \mu\text{m} \times 50 \mu\text{m}$), the SEM was thought useful to document the surface features as opposed to Dektak profilometer. The result of these experiments are described in the next section.

7.1.4 Planarization with SOG on Thin Film Diamond

Although SOG experiments performed earlier did not show much improvement in R_a , we still chose SOG as the planarizing layer due to several reasons. First of all, it is a spin-on-material which acts as a planarizing layer. It is regularly used for planarizing the multi-level interconnects in IC manufacturing due to the flowability of glass at high temperature. Secondly, SOG is a homogeneous material unlike the suspension of titanium-silicate in photoresist, which is not expected to show a two-phase etching. Thirdly, SOG is an already oxidized inorganic compound, and therefore does not etch at a very high rate in an

oxygen plasma. Also it is known that a fluorine containing plasma etches SiO_2 . Thus the etch ratio of diamond to SOG in an RIE process may be expected to be controlled by changing the ratio of oxygen content to the fluorine content in the etching discharge.

From some initial experiences of coating arc-jet samples with SOG as reported in section 7.1.2, we knew that the SOG coated surface shows cracks for multiple layers, in most cases when the number of layers is more than two, and in some cases when it is even more than one. The cracks seen on surface are thought to be mainly due to mismatching of thermal expansion between diamond and SOG. Since two layers of SOG at spinning speed of 3000 rpm refer to a total of $0.4 \mu\text{m}$ thick film, the SOG technique appeared to be limited to samples with surface roughness less than 0.4 micrometers.

However, in order to study the planarization experimentally, a microwave grown diamond-on-silicon sample was SOG spun at 3000 rpm for 30 seconds followed by a soft bake for 60 s at 150°C and hard bake for 1 hour at 400°C . The process was repeated to add another layer of SOG and the total thickness of the masking material was determined about 4000 Angstroms from the ellipsometer. Then the sample was broken into two pieces and each piece was etched under different plasma conditions. For both the discharges, the input microwave power, rf power, process pressure, downstream distance and the duration of the runs were same and were fixed at 500 watts, 100 watts, 4 mtorr and 45 minutes respectively. The oxygen to SF_6 gas flow ratio was changed intentionally to exploit the freedom of balancing the etch rate of SOG to diamond. One piece was etched in an argon-oxygen- SF_6 plasma with 12, 6, 2 sccm of gas flows and the other piece was etched with argon-oxygen- SF_6 plasma at flow rates of 12, 12, 2 sccms. Then the samples were cleaned with 50% hydrofluoric acid to wash away any remaining SOG.

SEMs were taken to document the uncoated, spun-on and post-etched surfaces of the sample. Figure 7.3 shows the uncoated microwave grown diamond sample at a magnification of 9000X. Typical grain sizes of this sample appear to be about $\sim 1 \mu\text{m}$ which is likely to produce a “short range” type of surface roughness which is needed to verify our hypothesis.

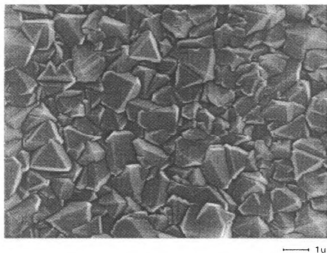


Figure 7.3: Uncoated sample surface

Figure 7.4 at 7500X, shows the result after etching with lower oxygen containing plasma, and Figure 7.5 at 7500X, shows the surface after etching in higher oxygen containing plasma. It is obvious from the SEMs that peaks of the diamond surface are indeed affected by the etching and some degree of planarization is achieved. The SEMs show that the planarization result improves when the oxygen flow rate was changed from 6 to 12 sccm. Figure 7.4 shows some planarization but Figure 7.5 shows an improvement. This indicates that the oxygen content in the 12:6:2 sccm of argon oxygen SF_6 plasma was not adequate.



Figure 7.4: Planarized surface after processing with low O_2 containing plasmas

The comparison of Figure 7.4 with 7.5 seems to give an idea of the process evolution indicating how the peaks of the polycrystalline diamond have somewhat been “melted away” due to etching and a relatively planar surface have slowly evolved.



Figure 7.5: Planarized surface after processing with high O_2 containing plasmas

However, the surface morphology after planarization is still far away from what would be an ideal plane surface. There are several reasons behind it. A look at the two-layer of SOG coated sample in Figure 7.6 is informative in this regard.

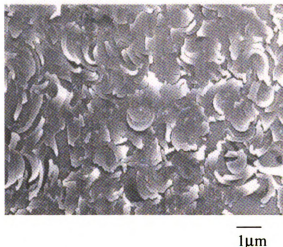


Figure 7.6: SOG coated diamond sample

The SEM of the SOG coated sample in Figure 7.6, reveals that although SOG has been successful in covering almost all the peaks on the surface, it could not really produce a perfect planarized layer. The scales seem to come off from the surface. Since the etch back method even under the perfect matched etch rate condition, can only retain the same degree of surface smoothness as achieved from the planarizing coating, a very smooth surface at the end of spin-on is desired. But in case of SOG, we do not find a very smooth post-spun-on surface to begin with, hence the final etched result was not very satisfactory.

Also after the etching runs were completed, pin-holes and voids are noticed to appear on the surface. Presently these are thought to be caused by the lack of film continuity for these very thin films (< 100 micrometers).

Our initial attempt has been helpful in gaining a better insight on the principle of the

etch-back method and its use for diamond planarization. The results support our hypothesis of short range planarization. However, a search for a better sacrificial coating needs to continue for a higher surface planarization outcome and to achieve planarization on a wide variety of samples irrespective of how they are produced.

7.2 Masking

One of the motivations for exploring the new diamond technology is to utilize its incomparably high thermal conductivity. Diamond used as a coating on silicon chips could mean a larger integration and smaller device spacings. This is because the heat produced by the chip which becomes a larger and larger concern with increased chip integration is carried away by the diamond layer. For producing this heat managing diamond layer, diamond needs to be first grown on the top of the IC and then patterned.

Masking polycrystalline diamond is a known technique although the problem becomes more difficult when the pattern needs to be transferred on a diamond-coated IC rather than a plain diamond surface. The complications mainly arise from the IC metallization layer that is underneath the diamond surface. Our research mainly concentrated on finding a masking material that could be easily patterned and removed without etching the underlying aluminum contact layer. Patterning diamond films can involve selective growing of the diamond seeds [7.9] as well as selective etching of a continuous thin film. Many studies on selective growth phenomenon of diamond and microstructural control of nucleation can be found [7.10, 7.11, 7.12] in literature. Selective etching of diamond has also been reported. The conventional method of transferring a pattern on the surface of a diamond-coated IC was successfully tried and reported [7.13] in 1990. The selective etching work in [7.13]

used an aluminum metal mask to pattern the diamond film grown on the top of an amplifier IC, which showed perfect functioning before the diamond growth and after the diamond etching. However the metal contact layer for the IC in this case was not aluminum.

For our research, a diamond layer was grown by Ulczynski et al., [7.14, 7.15] on the top of a 50 mm silicon wafer containing ICs of resistors, BJTs, FETs, and MOS capacitors. The metal layer was aluminum and our aim was to etch the diamond layer only from the metal contacts of the ICs in order to test the functioning of the devices. The diamond covered wafer had approximately 0.65 micrometer of diamond grown over the devices. This wafer was micrographically characterized at many different phases of operations. For this initial attempt, Spin-On-Glass was chosen as the masking material. It was known from the previous experiences that SOG can produce a thin ($\sim 4000 \text{ \AA}$) film which can exhibit an etch rate lower than that of diamond under certain plasma conditions. SOG was spun at 3000 rpm for 30 seconds over the diamond surface followed by a soft bake for 60 s at 150°C and hard bake for 1 hour at 400°C . The same process was repeated to add another layer of SOG such that the total thickness of the masking material was determined to be about 4000 Angstroms by the ellipsometer. Then a photoresist layer was spun, baked and patterned to in a standard way to make the wafer ready for the plasma etching. The SOG was etched with a 50:1 buffer oxide etch. From the plasma etch data established before, SOG and the diamond etch rates were found to be $\sim 325 \text{ \AA}/\text{min}$ and $\sim 475 \text{ \AA}/\text{min}$ in a 800 W, 110 V rf bias, 7 mtorr, Ar, Oxygen and SF_6 plasma. The gas flow rates in this case for Argon, Oxygen and SF_6 were 12, 6, and 2 sccm respectively. A total of 25 minutes of plasma etch was thought to be sufficient. Remaining SOG was etched using chemicals and the devices were inspected using a microscope.

An SEM shown in Figure 7.7, shows the removal of the diamond from the aluminum metal pads.

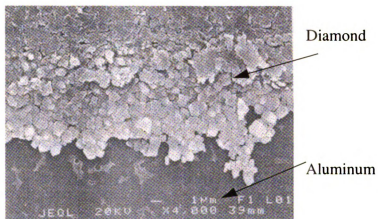


Figure 7.7: Selectively etched diamond coated IC shows aluminum pad

Some of the devices were successfully tested using the probe station and device parameter analyzer assembly. However, this experiment represents an initial attempt which can be further improved with the use of better mask material. In this first attempt, over-etching was noticed although the diamond was seen to be patterned.

Chapter VIII. Summary and Future Research

8.1 Summary of Research

The dc arc jet and microwave CVD grown samples were successfully etched using ECR plasmas generated from MPDR 325i reactor. Etching was mainly carried out with O₂ containing plasmas although some sputtering experiments were performed with only argon. Initial plasma etching experiments exhibited a low etch rate of diamond but with the help of statistically designed experiments the etch rate was increased by an order of magnitude. An etch rate of about 8 μm/hr on 100 mm wafers and 12 μm/hr on smaller samples were finally obtained. Statistical analysis showed that oxygen and rf bias have the strongest positive influences on etch rate while SF₆ has a negative effect. However, diamond etched in absence of SF₆ produced a black film on the etched surface. This black layer acted as a passivation layer, and the etch rate was found to decrease as the black film became denser. Hence etching of diamond at a steady high rate required the plasma to contain a minimum amount of SF₆.

Experiments demonstrated that plasma composition with higher oxygen contents produces higher etch rate and the etching nature was shown to be reactive ion assisted. The sputtering rate was found to be extremely low compared to the rate of reactive etching. An etch rate equation of diamond was also calculated from the theory of reactive etching and compared with the rate obtained from the experiments. These values agreed quite closely. A maximum of about 250 μm was removed from one single diamond wafer. The etch rate of diamond did not differ much from substrate side to the growth side.

Four inch, ~1.5 mm thick CVD grown polycrystalline diamond films were processed

with as low as 5% non-uniformity over the surface. The uniformity of diamond etching was observed to increase when etching was performed with more than one mode in sequence of time. This observation was theoretically investigated to learn about the role of modal patterns and ambipolar diffusion on the etching behavior. The simulation result supported the hypothesis of mixing modes to obtain higher uniformity of etching.

Another part of our research was aimed at planarizing rough diamond surfaces. The etch back method was employed to reduce the surface roughness of the arc-jet deposited and microwave CVD grown diamond samples. Different spin-on-sacrificial layers such as photoresist, titanium silicate emulsion in photoresist, and SOG were spun on diamond and used as planar coatings. UV-hardened photoresist in oxygen containing plasma environment showed a much higher etch rate compared to diamond in our system for all conditions investigated. Titanium silicate in photoresist showed a two phase etching mechanism with photoresist being etched away at a very high rate leaving behind the titanium silicate particles on the uneven surface of diamond. Both spin-on-layers of titanium silicate-photoresist emulsion and SOG resulted into planarizing the short range surface roughness. The long-range (order of 100 μm) surface variations were more or less followed by the coated layer. However, planarization experiments conducted on microwave grown diamond films with short range surface variation (order of 1 μm), showed initial success of achieving some degree of planarization using etch back technique.

Masking of diamond films using SOG was briefly investigated. An integrated circuit coated with diamond, was patterned with SOG and selectively etched with ECR plasmas. The aim of this work was to etch the diamond layer from the metal pads of the ICs. An argon, oxygen, SF_6 plasma was successfully used to remove the diamond layer from the

desired locations.

8.2 Future Work

Further development of ECR etching of diamond may go in many directions. A few of these potential research areas are highlighted below.

A. Obtaining higher etch rate

Etch rate of diamond may still be increased several folds if higher rf bias and higher microwave power are applied for etching. With an rf induced dc bias of 300V and the microwave power of 1.5 KW, the speculated etch rate becomes over 40 $\mu\text{m/hr}$ if the etch rate increased linearly with both bias and microwave power. The etch rate is unlikely to depend linearly on the microwave power and rf bias over an indefinite range, still one can reasonably expect to obtain an etch rate of about 25 $\mu\text{m/hr}$ using ECR oxygen plasmas.

B. Relation of rf power and induced dc bias in MPDR

Preliminary experiments showed that the rf induced dc bias is related to rf power in a complicated way for a microwave cavity. Detailed experimental or theoretical investigations were not performed to understand how the rf power (rf induced dc bias), microwave power, and the downstream distance are mutually related in a microwave ECR reactor. Investigation of this would be an important in order to understand the etching behavior of these microwave discharges with rf biasing.

C. Black film investigation

Although we were successful in preventing the formation of black film on diamond surface using SF₆ in plasma, we have not quantified the film. Black films grown under different etching conditions were not investigated or compared. Research can be directed with proper surface analysis techniques to identify the chemical composition of the black film in order to find the nature of the black film and the reason for its formation.

D. Relating etch rate to the quality of the diamond film

Different diamond samples showed different etch rate when etched simultaneously under same plasma conditions. The reason behind this observation has remained unexplored. Investigations relating the dependence of etch rate on the quality of the film namely, electrical conductivity, optical transparency, grain size and orientation may be quite helpful in answering the sample-to sample variation.

Also experiments with single diamond crystal will be an important contribution in finding the directional dependence of diamond etching with ECR plasmas. At this point, it is believed that plasma etching does not show large variation in etch rate from one direction to other.

E. Surface planarization

Although etch back technique following a coating of SOG on diamond showed some improvement of surface roughness, SOG is not an excellent material for planarization. As multiple layers are spun, cracks and scales are seen on the surface. Therefore, for an improved surface smoothening, search for a better planarizing material should continue.

Ideally this material should exhibit the ability to form a thick coating to planarize both long range and short range surface variations and show an etch rate comparable to diamond under attainable plasma conditions of the reactor.

F. Uniformity analysis and experimental verification

Further work is required to correlate etch uniformity in r and θ with different cavity modes. A more precise measurement technique than the micrometer would be useful. For example, the etching experiments could be conducted on smooth wafers such as, SiO_2 coated Si wafers and a wafer scanning ellipsometer can be used to record etch uniformity. This way the uncertainty of thickness measurement that arises from the roughness of a polycrystalline diamond wafer can be avoided.

8.3 Conclusions

In conclusion, ECR post-process etching was found to offer significant improvement as a diamond removal method as compared to conventional mechanical post-processing. The rate of material removal is over an order of magnitude higher than that obtained by the older method. This research represents the first report of high rate and uniform ECR plasma etching on large free standing diamond substrates. As a result, there is interest in transferring the technology to industry in order to supplement or replace the existing methods of diamond finishing. Also, the research describes a new method for controlling etch uniformity through mixed mode etching.

A significant challenge for future work is to achieve not only rapid material removal, but also improve the quality of the finished surface by reducing the surface roughness.

This involves the uses of sacrificial over-layers on diamond and will be the subject of ongoing research.

List of Appendices

Appendix A: Safety and Maintenance of ECR system

Some important safety issues for the users and the ECR plasma etching system are addressed here.

The plasma radiates UV light, hence looking directly into the plasma without having proper eye-protection should be avoided. The ECR system runs under high vacuum, hence caution must be taken to avoid all risks of implosion. If the pressure inside the main-chamber for any reason goes up, then the system should be immediately shut down for investigation before further processing. For example, a cracked bell jar can lead to dangerous accidents. As the system operates with microwave energy, microwave leak detection is necessary before processing. Proper and safe handling of gas cylinders is also a part of operating this system. If ever, the system is opened for maintenance, all necessary precautions must be taken to avoid inhaling any hazardous gas that may be used or generated during processing.

Preventive maintenance on a regular interval is suggested to reduce the chance of system failure. The mechanical pumps need an oil change, bearing lubrication etc. on a regular basis. Nitrogen should flow for purging the alcatel mechanical pump especially if fluorine contained gas e.g, SF₆ etc. is flown through the cavity. Presently the microwave cavity and the turbo pump is open-end water cooled using tap water. However, the turbo pump runs always and water should always flow through the pump. Water cooling lines get eventually clogged because of the sediment deposits and use of common cleaning agents for removal of sediments may be very damaging for the system at times. Therefore, closed loop cooling arrangement with cooling agents other than water is recommended. Usually mixture of ethylene glycol and de-ionized water is circulated through the chiller

for cooling. Presently the rf biased chuck is cooled this way, other parts that need cooling especially the microwave cavity may be recommended to switch over to closed-loop cooling system using chiller in future.

Appendix B: SPSS Output

27 Oct 94 SPSS for MS WINDOWS Release 6.0
This software is functional through January 31, 1995.

Page 1

**** MULTIPLE REGRESSION ****

Listwise Deletion of Missing Data

Equation Number 1 Dependent Variable.. RATE

Block Number 1. Method: Enter POWER SF6 O2 BIAS

Variable(s) Entered on Step Number 1.. SF6 2.. BIAS
3.. O2 4.. SF6

Multiple R .98505
R Square .97033
Adjusted R Square .95549
Standard Error .10438

Analysis of Variance	DF	Sum of Squares	Mean Square
Regression	4	2.85047	.71262
Residual	8	.08716	.01090

F = 65.40646 Signif F = .0000

----- Variables in the Equation -----

Variable	B	SE B	95% Confdnce	Intrvl B
BIAS	.033841	.004142	.024289	.043394
O2	.138801	.017585	.098250	.179351
POWER	.001983	5.5480E-04	7.03893E-04	.003263
SF6	-.065051	.017585	-.105601	-.024500
(Constant)	-2.937349	.491688	-4.071183	-1.803515

End Block Number 1 All requested variables entered.

Appendix C: Matlab Programs

The following Matlab program generates Figure 6.5

```
% Ambipolar Diffusion Simulation
% Initialize the matrix and problem size
% Assume that there is no recombination in the plasma; i.e.,
%  $V_i/D = 0$  % Down-stream Distance  $dist1=1$ ;  $dist2=2$ ;
% Collisional term:  $col = v_i/D$ 
col=0.0;
a=zeros(20,20);
nr=20;
nz=20;
delr=1.0;
delz=1.0;
delr2=delr*delr;
delz2=delz*delz;
% Initialize the boundary
for m=1:nz
    a(20,m)=0.0;
end
for m = 1:nr
    if m>10
        a(m,1)=0.0;
    else a(m,1)=1+(0.09*m)^2;
        a(m,20)=0.0;
    end
end
% Set up the matrix : Use the iterative method
for k = 1:100
    maxerr=0.0;
    sumerr=0.0;
    for i=2:nr-1
        for j=2:nz-1
            r=i*delr;
            adev=(2./delr2+2./delz2+col);
            apr2=a(i+1,j)/delr2;
            amr2=a(i-1,j)/delr2;
            apr1=a(i+1,j)/(2.*r*delr);
            amr1=-a(i-1,j)/(2.*r*delr);
            apz2=a(i,j+1)/delz2;
            amz2=a(i,j-1)/delz2;
            anew=(apr2+apr1+amr2+amr1+apz2+amz2)/adev;
            err=abs(anew-a(i,j));
            maxerr=max(err,maxerr);
        end
    end
end
```

```

        sumerr=sumerr+err;
        a(i,j)=anew;
    end
end
for m=1:nz
    a(1,m)=a(2,m);
end
end
sumerr;
maxerr;
for m=1:nr
    conc1(m)=a(m,dist1)/a(10,1);
    conc2(m)=a(m,dist2)/a(10,1);
    rad(m)=0.5*(m-1);
end
plot(rad,conc1,'-',rad,conc2,'-.')
title ('Figure 6.5 : Diffusion of Species in Mode 1')
ylabel ('Species Concentration') xlabel ('Radial Distance in inches')
gtext ('___ Concentration : at source')
gtext ('-.- Concentration : 5 cm below')
print mesh1.ps

```

The following Malab program generates Figure 6.6

```

% Ambipolar Diffusion Simulation
% Initialize the matrix and problem size
% Assume for that there is no generation-recombination in the plasma; i.e, %  $V_i/D = 0$ 
% Down-stream Distance dist1=1; dist2=8;
% Collisional term : col =  $v_i/D$ 
col=0.0;
a=zeros(20,20);
nr=20;
nz=20;
delr=1.0;
delz=1.0;
delr2=delr*delr;
delz2=delz*delz;
% Initialize the boundary
for m=1:nz
    a(20,m)=0.0;
end
for m = 1:nr
    if m>10

```

```

    a(m,1)=0.0;
    else a(m,1)=1+(0.02*m)^2;
    a(m,20)=0.0;
end
end
% Set up the matrix : Use the iterative method
for k = 1:100
maxerr=0.0;
sumerr=0.0;
for i=2:nr-1
for j=2:nz-1
    r=i*delr;
    adev=(2./delr2+2./delz2+col);
    apr2=a(i+1,j)./delr2;
    amr2=a(i-1,j)./delr2;
    apr1=a(i+1,j)/(2.*r*delr);
    amr1=-a(i-1,j)/(2.*r*delr);
    apz2=a(i,j+1)./delz2;
    amz2=a(i,j-1)./delz2;
    anew=(apr2+apr1+amr2+amr1+apz2+amz2)/adev;
    err=abs(anew-a(i,j));
    maxerr=max(err,maxerr);
    sumerr=sumerr+err;
    a(i,j)=anew;
end
end
for m=1:nz
    a(1,m)=a(2,m);
end
end
sumerr;
maxerr;
for m=1:nr
conc1(m)=a(m,dist1)/a(10,1);
conc3(m)=a(m,dist2)/a(10,1);
rad(m)=0.5*(m-1);
end plot(rad,conc1,'-',rad,conc3,'-.')
title ('Figure 6.6 : Diffusion of Species in Mode 2')
ylabel ('Species Concentration')
xlabel ('Radial Distance in inches')
gtext ('___ Concentration: at source')
gtext ('-.- Concentration: 20 cm below')
print mesh2.ps

```

To generate Figure 6.7, three Matlab programs are to be run in sequence. These three programs are numbered as Program 1, Program 2 and Program 3, These programs are given below.

Program 1

```

% Ambipolar Diffusion Simulation
% Initialize the matrix and problem size
% Assume that there is no generation-recombination in the plasma; i.e, % Vi/D =0
% Down-stream Distance dist1=1; dist2=2;
% Collisional term : col = vi/D
col=0.0;
a=zeros(20,20);
nr=20;
nz=20;
delr=1.0;
delz=1.0;
delr2=delr*delr;
delz2=delz*delz;
edge=9;
% Initialize the boundary
for m=1:nz
    a(20,m)=0.0;
end
for m = 1:nr
    if m>10
        a(m,1)=0.0;
    else a(m,1)=1+(0.09*m)^2;
        a(m,20)=0.0;
    end
end
% Set up the matrix : Use the iterative method
for k = 1:100
    maxerr=0.0;
    sumerr=0.0;
    for i=2:nr-1
        for j=2:nz-1
            r=i*delr;
            adev=(2./delr2+2./delz2+col);
            apr2=a(i+1,j)./delr2;
            amr2=a(i-1,j)./delr2;
            apr1=a(i+1,j)/(2.*r*delr);
            amr1=-a(i-1,j)/(2.*r*delr);
            apz2=a(i,j+1)./delz2;

```

```

    amz2=a(i,j-1)/delz2;
    anew=(apr2+apr1+amr2+amr1+apz2+amz2)/adev;
    err=abs(anew-a(i,j));
    maxerr=max(err,maxerr);
    sumerr=sumerr+err;
    a(i,j)=anew;
end
end
for m=1:nz
    a(1,m)=a(2,m);
end
end
sumerr;
maxerr;
for m=1:nr
    conc1(m)=a(m,dist1)/a(10,1);
    conc2(m)=a(m,dist2)/a(10,1);
    rad(m)=0.5*(m-1);
end
etch1=conc2(1:edge);
radius=rad(1:edge);
plot(radius,etch1,'-')

```

Program 2

```

% Ambipolar Diffusion Simulation
% Initialize the matrix and problem size
% Assume that there is no generation-recombination in the plasma; i.e.,  $v_i/D = 0$ 
% Down-stream Distance dist1=1; dist2=8;
% Collisional term : col =  $v_i/D$ 
col=0.0; a=zeros(20,20);
nr=20;
nz=20;
delr=1.0;
delz=1.0;
delr2=delr*delr;
delz2=delz*delz;
edge=9;
% Initialize the boundary
for m=1:nz
    a(20,m)=0.0;
end for m = 1:nr
    if m>10
        a(m,1)=0.0;
    else a(m,1)=1+(0.02*m)^2;

```

```

a(m,20)=0.0;
end
end
% Set up the matrix : Use the iterative method
for k = 1:100
maxerr=0.0;
sumerr=0.0;
for i=2:nr-1
for j=2:nz-1
r=i*delr;
adev=(2./delr2+2./delz2+col);
apr2=a(i+1,j)./delr2;
amr2=a(i-1,j)./delr2;
apr1=a(i+1,j)/(2.*r*delr);
amr1=-a(i-1,j)/(2.*r*delr);
apz2=a(i,j+1)./delz2;
amz2=a(i,j-1)./delz2;
anew=(apr2+apr1+amr2+amr1+apz2+amz2)/adev;
err=abs(anew-a(i,j));
maxerr=max(err,maxerr);
sumerr=sumerr+err;
a(i,j)=anew;
end
end
for m=1:nz
a(1,m)=a(2,m);
end
end
sumerr;
maxerr;
for m=1:nr
conc1(m)=a(m,dist1)/a(10,1);
conc3(m)=a(m,dist2)/a(10,1);
rad(m)=0.5*(m-1);
end
etch2=conc3(1:edge);
radius=rad(1:edge);
plot(radius,etch2,'--')

```

Program 3

```

etch3=(etch1+etch2)/2;
plot(radius,etch1,'--',radius,etch2,'-.',radius,etch3,'-')
title ('Comparison of Etching Profiles')
ylabel ('Etching Profile')

```

```
xlabel ('Radial Distance on Wafer Surface (inches)')  
gtext ('Etching profile in Mode 1 alone')  
gtext ('Etching profile in Mode 2 alone')  
gtext ('Etching in mixed modes : Mode 1 for 50% and Mode 2 for 50% time')  
print etch.ps
```

List of References

List of References

Chapter 1

[1.1] "Synthesis of Large Area Diamond Film by a Low Pressure DC Plasma Jet, R. L. Woodin, L. K. Bigelow, and G. L. Cann, Proceedings of the First International Conference on the Applications of Diamond Films and Related Materials, Edited by Y.Tzeng, M. Yoshikawa, M. Murakawa, A. Feldman (editors), Elsevier Science Publishers, August 17-22, 1991, pp 439-444.

[1.2] Comparison of Advanced Plasma Sources for Etching Applications: a Helicon and a Multipolar ECR, J. T. Lee, F. P. Klemens, J. L. Benton, G. S. Higashi, T. Boone, A. Onuoha, R. A. Gottscho, D. E. Ibbotson, G. W. Gibson, H. H. Sawin and J. Cecchi, Final Report for SRC/Sematech, AT&T Bell Laboratories, December 3, 1993.

[1.3] "Plasma Etching with a Microwave Cavity Plasma Disk Source", J. Hopwood, M. Dahimene, D. K. Reinhard, and J. Asmussen, Journal of Vacuum Science and Technology, B 6, 1988, pp 268.

[1.4] "Comparison of CH₄/H₂/Ar Reactive Ion Etching and Electron Cyclotron Resonance Plasma Etching of In-based III-V Alloys", S. J. Pearton, U. K. Chakrabarti, A. Katz, P. Perley, W. S. Hobson, C. Constantine, Journal of Vacuum Science and Technology, B 9(3), 1992, pp 1421-1432.

Chapter 2

[2.1] "Applications of Bulk and Thin Film Diamond", M. Seal, Proceedings of the First International Conference on the Applications of Diamond Films and Related Materials, Edited by Y.Tzeng, M. Yoshikawa, M. Murakawa, A. Feldman (editors), Elsevier Sci-

ence Publishers, August 17-22, 1991, pp 3-7.

[2.2] Diamond Chemical Vapor Deposition, F. G. Celli and J. E. Butler, in Annual Review of Physical Chemistry, Vol. 42, Annual Reviews Inc., 1991.

[2.3] Class notes of EE 989/NTU IC 734-MS by J. C. Angus, Lecture 19, 1995.

[2.4] "Magnetoplasmadynamics Apparatus and Process for Separation and Deposition of Materials", G. L. Cann, U.S. Patent nos. 4471003 and 4487162.

[2.5] "Magnetoplasmadynamics Processor, Application thereof and Methods", G. L. Cann, U.S. Patent no. 4682564.

[2.6] Diamond Cutting, B. Watermeyer, 2nd edition, published by Centaur, Johannesburg, 1982.

[2.7] Hardness 10: Diamond, E. Vleeschdrager, published by Gaston Lachurie, Paris, 1986.

[2.8] Properties and Application of Diamond, John Wilks and Eilen Wilks, published by Butterworth and Heinemann, 1991, Chapter 9, pp 228-264.

[2.9] V. P. Ageev, L. L. Builov, V. I. konov et. al., Soviet Physics - Doklady., Vol. 33, 1988, pp 840.

[2.10] S. Tezuka and M. Yoshikawa, Japan Society of Precision Engineering, Vol. 56. 12, 1990 pp. 2255.

[2.11] "Light-induced polishing of diamond films", V. N. Tokorev and V. I. Konov, Proceedings of the First International Conference on the Applications of Diamond Films and Related Materials, Edited by Y.Tzeng, M. Yoshikawa, M. Murakawa, A. Feldman (editors), Elsevier Science Publishers B.V., 1991, pp 249-255.

[2.12] "Laser Patterning of Diamond Films", J. Narayan and X. Chen, Journal of

Applied Physics, Vol. 71, April 15, 1992, pp 3795-3801.

[2.13] "Cutting and Surface Planing of CVD Diamond Films by YAG Laser", S. Tezuka and M. Yoshikawa, *New Diamond*, Vol. 17, 1990, pp 36-37.

[2.14] "Diamond Properties and Applications", M. Yoder, Chapter 1 of Diamond Films and Coatings, Development, Properties, and Applications, Noyes Publication, 1993, pp 1-30.

[2.15] "The Polishing of Polycrystalline Diamond Films", A. B. Harker, J. Flintoff, J. F. DeNatale, *Diamond Optics III*, SPIE, Vol. 1325, 1990, pp 222-229.

[2.16] "Development and Performance of a Diamond Film Polishing Apparatus with Hot metals", M. Yoshikawa, *Diamond Optics III*, SPIE, Vol. 1325. pp 210-217.

[2.17] "Polishing of CVD Diamond Films", H. Tokura, M. Yoshikawa, *Proceedings of the First International Conference on the Applications of Diamond Films and Related Materials*, Edited by Y.Tzeng, M. Yoshikawa, M. Murakawa, A. Feldman (editors), Elsevier Science Publishers, August 17-22, 1991, pp 241-248.

[2.18] "Shaping of Diamond films by Etching with Molten Rare-Earth Metals", S. Jin, J. E. Graebner, M. McCormack, T. H. Tiefel, A. Katz, and W. C. Dautremont-Smith, *Nature*, Vol. 362, 1993, pp 822-824.

[2.19] "Massive Thinning of Diamond Films by a Diffusion Process", S.Jin, J.E. Graebner, G.W. Kammlott, T.H. Tiefel, S.G. Kosinski, L.H. Chen, and R.A. Fastnacht, *Applied Physics Letters*, Vol. 60, 1992, pp 1948.

[2.20] "Thinning a Diamond Body by means of Molten Rare-Earth-Containing Alloys" J.E. Graebner, S.Jin, and M. McCormack, AT&T Bell Laboratory, U.S. Patent No. 5328550, Oct 1992.

[2.21] "Thermal Conductivity in Molten-Metal-Etched Diamond Films", S. Jin, L. H. Chen, J. E. Graebner, M. McCormack, M. E. Reiss, Applied Physics Letters, Vol. 63, 1993.

[2.22] "Diamond Shaping and Polishing by Chemical Reactions", S.Jin, W.Zhu and T.H. Tiefel, Extended abstract no. 223, The Electrochemical Society, Spring meeting at Reno, Nevada, Vol. 95-1, May, 1995, pp 340-341.

[2.23] T. Evans and P. F. James, Proceedings of Royal Society, London, Vol. A 277, 1964. pp 260.

[2.24] G. Davis and T. Evans, Proceedings of Royal Society, London, Vol. A 328, 1972, pp 413.

[2.25] L.S. Plano, S. Yokota, and K.V. Ravi, Proceedings of First International Symposium on Diamond and Diamond-like Films, Proc. vol 89-12, The Electrochemical Society, Pennington, NJ, 1989, pp 380.

[2.26] "Oxidation Kinetics of Diamond, Graphite and Chemical Vapor Deposited Diamond Films by Thermal Gravimetry", A. Joshi, and R. Nimmagadda, and J. Herrington, Journal of Vacuum Science and Technology, A, 1990, pp 2137.

[2.27] "Post-depositional Diamond Etching", P.K. Bachmann, D. Leers, D.U. Wiechert, Diamond and Related Materials, February, 1993, pp 683-693.

[2.28] "Oxidation of Diamond Films Synthesized by hot Filament assisted Chemical Vapor Deposition", K. Tankala, T. DebRoy, M. Alam, Journal of Material Research, Vol. 5, Nov 1990, pp 2483-2489.

[2.29] "The Role of Microstructure on the Oxidation Behavior of Microwave Plasma Synthesized Diamond and diamond-like carbon Films", R. R Nimmigada, A. Joshi, W. L.

Hsu, *Journal of Material Research*, Vol. 5, Nov 1990, pp 2445-2450.

[2.30] "Etching of Diamond with Argon and Oxygen Ion Beams", T.J. Whetten, A. A. Armstead, T. A. Grybowski, and a. L. Rouff, *Journal of Vacuum Science and Technology*, Vol. A(2), 1984, pp 477.

[2.31] "Ion-beam-assisted Etching of Diamond", N. N. Efremow, M. W. Geis, D. C. Flanders, G. A. Lincoln, and N. P. Economou, *Journal of Vacuum Science and Technology*, Vol. B(3), January/February 1985, pp 416-418.

[2.32] "Planarization Technique for Ion-beam Polishing of Diamond Films", D. F. Grogan, T. Zhao, B. G. Bovard, and H. A. Macleod, *Applied Optics*, Vol. 31, No. 10, April 1, 1992, pp 1483-1487.

[2.33] "Smoothing of Diamond Films by Ion Beam Irradiation", A. Hirata, H. Tokura, and M. Yoshikawa, *Proceedings of the First International Conference on the Applications of Diamond Films and Related Materials*, Edited by Y.Tzeng, M. Yoshikawa, M. Murakawa, A. Feldman (editors), Elsevier Science Publishers, August 17-22, 1991, pp 227-232.

[2.34] "Diamond film polishing with Argon and Oxygen ion beams", Z. Tianji, D. F. Grogan, B. G. Bovard, and H.A. Macloed, *SPIE Vol. 1325, Diamond Optics III*, 1990, pp 142-151.

[2.35] "Oxygen-ion beam polishing of a 5-cm-diameter diamond flambe. G. Bovard, T. Zhao, and H. A. Macleod, *Applied Optics*, Vol 31, No. 13, May 1992, pp 2366-2369.

[2.36] "Air Microwave Plasma Etching of Polycrystalline Diamond Thin films" R. Ramesham and B. H. Loo, *Journal of the Electrochemical Society*, Vol. 139, No. 7, July 1992, pp 1988-1993.

[2.37] "Reactive Ion Etching of Diamond", G. S. Sandhu and W. K. Chu, Applied Physics Letters, Vol. 55, No. 5, July 31, 1989, pp 437-438.

[2.38] "Erosion of Diamond Films and Graphite in Oxygen Plasma", A. Joshi, and R. Nimmagadda", Journal of Materials Research, Vol. 6, No. 7, July 1991, pp 1484-1490.

[2.39] "Dry Etching of Undoped and Boron Doped Polycrystalline Diamond Films", O. Dorsch, M. Werner, and E. Obermeier, Diamond and Related Materials, Elsevier Science publishers, Vol. 4, 1995, pp 456-459.

[2.40] Application of Plasma Process to VLSI Technology, T. Sugano, Wiley, 1985.

[2.41] "ECR Plasma Etching of Chemically Vapour Deposited Diamond Thin film", S. J. Pearton, A. Katz, F. ren, and J. R. Lothian, Electronics Letters, Vol. 28, No. 9, April 23, 1992, pp 822-824.

[2.42] "Diamond Thin-Film recessed Gate Field-Effect-Transistors Fabricated by Electron Cyclotron Resonance Plasma Etching", S. A. Grot, and G. Sh. Gildenblat, IEEE Electron Devices Letters, Vol. 13, No. 9, September 1992, pp 462-464.

[2.43] "CVD Diamond Films Etching in ECR Discharge", N. V. Suetin, K. S. Gulyaev, A. S. Kovalev, A. T. Rakhimov, and A. N. Vasilieva, Extended abstract no. 224, The Electrochemical Society, Spring meeting at Reno, Nevada, Vol. 95-1, May 1995, pp 343.

[2.44] Private Conversation with Dr. N. V. Suetin at the Conference of The Electrochemical Society, Spring meeting at Reno, Nevada, May 1995.

[2.45] J Asmussen, J. Hopwood, and F. C. Sze, Review of Scientific Instruments, Vol 61, 1990, pp250.

[2.46] Plasma Processing, McGraw Hill Encyclopaedia of Science and Technology, 1992, pp 353-356.

[2.47] Gaseous Electronics and Gas Lasers, B. E. Cherrington, Pergamon Press, 1974.

[2.48] "Electron Cyclotron Microwave Discharge for Etching and Thin film deposition", Jes Asmussen, *Journal of Vacuum Science and Technology*, Vol. A7, No. 3, May/June 1989, pp 883-893.

Chapter 3

[3.1] Wavemat Inc., 44191 Plymouth Oaks Blvd., Suite 100, MI 48170, USA.

[3.2] PlasmaQuest Inc., 850 N. Dorothy Drive, Suite 504, Richardson, TX 75081, USA.

[3.3] "Electron Cyclotron Resonance Microwave Discharge for Etching and Thin Film Deposition", J. Asmussen, Chapter 11 of Handbook of Plasma Processing Technology: Fundamentals of Etching, Deposition, and Surface Interactions, Park Ridge, N.J., Noyce Publication, 1990.

[3.4] "Plasma Diagnostics Modeling and Etching Application of the Multipolar ECR Plasma Reactor", J. Asmussen, paper distributed as a part of class notes for EE 989, 1993.

[3.5] Basic Operation Instruction for Plasmaquest 357 W Electron Cyclotron Resonance Reactor, User Manual, Chapter 4 and Chapter 10.

[3.6] User Manual for Gaertner WaferScanTM Ellipsometer L 115 B, Gaertner Scientific Corporation.

[3.7] "Characterization of Diamond Films", W. Zhu, H. S. Kong, J. T. Glass, Chapter 6, of Diamond Films and Coatings, Development, Properties and Applications, R. F. Davis, Noyes Publications, New Jersey, 1993, pp 244-327.

[3.8] Headway Research Inc, Netscape web site: <http://argon.eecs.berkeley.edu:8080/>

text/equipment.mar

[3.9] Warning and Rating Label of Headway Spinner.

[3.10] Semiconductor Integrated Circuit Technology, W. R. Runyan Addison-Wesley, 1990.

[3.11] User Manual of MJB 3 Mask Aligner, Karl Suss.

[3.12] R. J. Nemanich and J. T. Glass, Journal of Vacuum Science and Technology, A 6, 1988, 1783-1787.

[3.13] User Manual for HP 4145 B parameter analyzer and the operating diskette, Hewlett Packard.

Chapter 4

[4.1] Glow Discharge Processes: Sputtering and Plasma Etching, B. Chapman, Wiley, New York, 1980, Chapter 7, pp 297-342.

[4.2] Plasma Etching: an Introduction, D. L. Flamm and D. M. Manos, Academic Press, Boston, 1989, Chapter 2, pp 91-182.

[4.3] Plasma Diagnostics Techniques, R. H. Huddleston and S. L. Leonard, Academic Press, 1965.

[4.4] "Optical Emission Spectroscopy of Reactive Plasmas: A Method for Correlating Emission Intensities to Reactive Particle Density", J. W. Coburn, and M. Chen, Journal of Applied Physics, Vol 51, 1980, pp 3134-.

[4.5] "Positive Ion currents in the Positive Column of the Mercury Arc". I. Langmuir, General Electric Review, Vol 26, 1923 pp 731-735.

[4.6] A Theoretical and Experimental Investigation of the Chemical Kinetics of an

Oxygen Microwave Discharge, M. L. Brake, Ph.D dissertation, 1983, MSU, pp20-25.

[4.7] Diffusion Process, M. H. Jacobs, Springer-Verlag, 1967.

[4.8] The Diffusion and Drift of Electrons in Gases, L. G. H. Huxley, Wiley, 1974.

[4.9] Diffusion Kinetics for Atoms in Crystals, J. R. Randolph, Van Nostrand, 1968.

[4.10] The Mobility and Diffusion of Ions in Gases, E. W. Wadsworth, Wiley, 1973.

[4.11] Principles of Plasma Discharge and Materials Processing, M. A. Lieberman and A. J. Lichtenberg, John Wiley and Sons, 1994, Chapter 9, pp 290-297.

[4.12] Introduction to Plasma Physics, B. M. Smirov, Mir Publisher, 1977.

[4.13] The Adsorption of Gases on Solids, N. Feather and D. Shoneberg, Cambridge university Press, 1949.

[4.14] Physisorption Kinetics, H. J. Kreuzer, Springer-Verlag, 1986.

[4.15] Theory of Chemisorption, Springer Verlag, 1980.

[4.16] Elementary Chemical Kinetics, J. L. Latham and A. e. Burgess, Butterworths, 1962.

[4.17] Basic Chemical Kinetics, H. Eyring, Wiley, New York, 1980.

[4.18] Chemisorption, D. O. Hayward and B. M. W. Trapnell, Butterworths, London, 1964.

[4.19] Diffusion and heat transfer in chemical kinetics, D. A. Frank-kamenskii, Plenum Press, New York, 1969.

[4.20] Principles of Plasma Discharge and Materials Processing, M. A. Lieberman and A. J. Lichtenberg, John Wiley and Sons, 1994, Chapter 15, pp 472-510.

[4.21] "Measured Temperatures of Burning Pulverized Particles and the Nature of the Primary reaction Products", A. B. Ayling, and I. W. Smith, Combustion and Flame, Vol

18, 1972, pp 172.

[4.22] "The Role of Surface Complex in the Carbon-Oxygen Reaction", N. R. Laine, F. J. Vastola, and P. L. Waker Jr., Proceedings of the Fifth Carbon Conference, Vol 2, Pergamon Press, New York, 1963.

[4.23] Combustion, I. Glassman, Academic Press, 1987, pp 391-395.

[4.24] "Factors Affecting the Product Ratio of the Carbon-Oxygen Reaction- II. Reaction Temperature", R. Phillips, F. J. Vastola, P. L. Walker Jr., Carbon, Vol 8, 1970, pp 205.

[4.25] "Combustion and Mass Transfer Characteristics of Large Carbon Particle in the Grid Region of a Fluidized Bed Combustor", A. S. Choi, Ph.D dissertation, 1988, Section 2-2, pp 1-30.

[4.26] "Heterogeneous Kinetics of Coal Char Gasification and Combustion", N. M. Laurendeau, Progress in Energy and combustion science, Vol 4, 1978, pp 221-270.

Chapter 5

[5.1] Glow Discharge Processes, B. Chapman, John Wiley & Sons, 1980, Chapter 1, pp 1-19.

[5.2] "ECR sputter removal of SiO₂ on Silicon Wafers", V. Gopinath, G. T. Salbert, T. A. Grotjohn, and D. K. Reinhard, Journal of Vacuum Science and Technology, B 11, Vol 6, Nov/Dec 1993, pp 2067-2070.

[5.3] Macroscopic Properties of a Multipolar Electron Cyclotron Resonance Microwave Plasma Source for Anisotropic Silicon Etching, J. A. Hopwood, Ph.D desertion, MSU, 1990, Chapter 5, Section 5.6.3, pp 99-108.

[5.4] Design and Experimental Investigation of a Large Diameter Electron Cyclotron

Resonance Plasma Source, F. C. Sze, Ph.D Dissertation, MSU, Chapter 4 and Chapter 6.

[5.5] Statistics for Experiments: An Introduction to Design, Analysis, and Model Building, G.E. P. Box, Willey, 1978.

[5.6] Analysis of Messy Data, G. A. Milliken, Lifetime Learning Publication, 1984.

[5.7] Response Surface Methodology, R. H. Myers, Allyn and Bacon, 1971.

[5.8] "Statistical Experimental Design in Plasma Etch Modeling", G. S. May & C. J. Spanos, IEEE Transaction on Semiconductor Manufacturing, Vol 4, No. 2, May 1991, pp 83-98.

[5.9] "Optimization of a Low Damage, High Resolution SiN_x Etch Process in an Electron Cyclotron Resonance (ECR) Reactor with Multipolar Confinement", R. J. Olson, T. E. Kaizor, B. Lane, W. M. Hobler, and L. Bourget, Presented at The Electrochemical Society, Spring meeting at Reno, Nevada, May 1995.

[5.10] Statistical Design and Analysis of Experiments with Applications to Engineering and Science, R. L. Mason, R. F. Gunst, and J. L. Hess, John Wiley and Sons, Chapter 7, 9, 11, and 15.

[5.11] SPSS for Windows Made Simple P. R. Kinner, Lawrence Erlbaum, 1994.

[5.12] Temperature and Concentration of Ionic and Neutral Species in Resonant Microwave Cavity Plasma Discharges, G. L. King, Ph.D Desertion, MSU, 1994.

[5.13] Principles of Plasma Discharges and Materials Processing, M. A. Lieberman and A. J. Lichtenberg, John Wiley and Sons, 1994, Chapter 11, pp 327-386.

[5.14] "High Frequency Sustained Multipolar Plasmas", C. Pomot and J. Pelletier, Chapter 13 of Microwave Excited Plasmas, edited by M. Moisan and J. Pelletier, Elsevier, 1992, pp 385-418.

[5.15] "Investigation of Influence of Electromagnetic Excitation on Electron Cyclotron Resonance Discharge Properties", P. Mak, G. King, T.A. Grotjohn, and J. Asmussen, *Journal of Vacuum Science and Technology*, A 10, No. 4, 1992, pp 1281-1287.

[5.16] "Ion and Neutral Energies in a Multipolar Electron Cyclotron Resonance Plasma Source", G. King, F. C. Sze, P. Mak, T. A. Grotjohn, and J. Asmussen, *Journal of Vacuum Science and Technology*, A 10, No. 4, 1992, pp 1265-1269.

[5.17] "Investigation of Multipolar ECR Plasma Source Sensors and Models for Process Control", P. U. Mak, M. H. Natarajan, B. L. Wright, T. A. Grotjohn, F. Salam, M. Siegel, and J. Asmussen, presented at 42nd National Symposium of the American Vacuum Society, Minneapolis, Minnesota, Oct 1995.

[5.18] "Cleaning of Metal Parts in Oxygen Radio Frequency PLasma: Process Study", D. Korzec, J. Rapp, D. Theirich, and J. Engemenn, *Journal of Vacuum Science and Technology*, A 12, 1994, pp 369.

[5.19] Glow Discharge Processes, B. Chapman, John Willey & Sons, 1980, Chapter 6, pp 250.

Chapter 6

[6.1] EE 836 Lecture Notes, K. M.Chen, Chapter 2, MSU, 1994.

[6.2] Field and Wave Electromagnetics, D. Cheng, Addison-Wesley, 1992.

[6.3] Elements of Engineering Electromagnetics, N. N. Rao, Prentice Hall, 1991.

[6.4] "Plot of Modal Field Distribution in Rectangular and Circular Waveguides", C. S. Lee, W. Lee, and S. Chuang, *IEEE Transactions on Microwave Theory and Techniques*, Vol 33, pp 271, 1985.

[6.5] Numerical Solution of Differential Equation, I. Fried, Academic Press, 1979.

[6.6] The Student Edition of MATLAB: Student User Guide, Prentice Hall, 1992.

Chapter 7

[7.1] Manual for Atomic Force Microscope, 1993, pp 243.

[7.2] "Method for Leveling Diamond Film", Patent Application No. 62-220052, Japanese Patent Office, Sep 2, 1987.

[7.3] "Surface Smoothing of Diamond Membranes by Reactive Ion Etching Process" C. Vivensang, L. Ferlazzo-Manin, M. F. Ravet, G. Turban, F. Rousseaux, and A. Gicquel, to be published in *Diamond and Related Materials*.

[7.4] "ECR Plasma Polishing of CVD Diamond Films", H. Buchkremer-Hermanns, C. Long, and H. Weiß, presented at *Diamond Films 1995*, Barcelona.

[7.5] "Experimental Study of Diamond Surface Planarization", D. K. Reinhard, research proposal submitted to Norton Diamond Film, 1993.

[7.6] Hoechst Celanese Group, Somerville, NJ, USA.

[7.7] Filmtronics Inc., P. O. Box 1521, Butter, PA 16003, USA.

[7.8] Shipley Inc., 500 Nickerson Road, Marlboro, MA 01752, USA.

[7.9] "Techniques for patterning of CVD diamond films on non-diamond substrates", Masood A, Aslam M, Tamor M.A, *Journal of the Electrochemical Society*, Vol 138: L67-8, Nov 1991.

[7.10] "Microstructural control of diamond thin films by microlithographic patterning", J. F. DeNatale, J. F. Flintoff and A.B. Harker, *J. Appl. Phys.*, Vol. 68 (8), 15 October 1990, pp 4014-4019.

[7.11] "Selected area nucleation and patterning of diamond thin films by electro-phoretic seeding", J. L. Valdes, J.W. Mitchel, J. A. Mucha, L. Seibles, and H. Huggins, *Journal of Materials Science*, 27, 1992, pp 553-556.

[7.12] "Micropatterned diamond substrate", J.W. Glesener, and R. J. Tonucci, *J. Appl. Phys.*, Vol. 74, No. 8, 1993, pp 5280-5281.

[7.13] "Processes for the preparation of Polycrystalline Diamond Films", F. Jansen and M. A. Machonkin, Xerox Inc. U.S. Patent # 4925701, May 15, 1990.

[7.14] "M. Ulczynski, D. K. Reinhard, M. Prystajko, and J. Asmussen, *Advances in New Diamond Science and Technology*, edited by S. Saito, N. Fujimori, O. Fukunaga, M. Kamo, K. Kobashi, and M. Yoshikawa, pp 41, M.Y.U., Tokyo, 1994.

[7.15] "Diamond Coatings on Integrated Circuits", D. K. Reinhard, M. Ulczynski, and R. N. Chakraborty, presented at 3rd International Conference on Applications of Diamond Films and Related Materials, Gaithersburg, Maryland, August 21-24, 1995.

MICHIGAN STATE UNIV. LIBRARIES



31293014027761